La investigación reportada en esta tesis es parte de los programas de investigación del CICESE (Centro de Investigación Científica y de Educación Superior de Ensenada, Baja California).
La investigación fue financiada por el SECIHTI (Secretaría de Ciencia, Humanidades, Tecnología e Innovación).

Centro de Investigación Científica y de Educación Superior de Ensenada, Baja California

Doctor of Science
in Earth Science with orientation in Seismology

Seismic wave propagation in fractured media saturated with fluids

A dissertation

submitted in partial satisfaction of the requirements for the degree

Doctor of Science

By:

Ana Lucía Ramos Barreto

Ensenada, Baja California, Mexico

2025

A Dissertation Presented by

Ana Lucía Ramos Barreto

and approved by the following Committee

Dr. Jonás de Dios de Basabe Delgado
Thesis director

Dr. Tobias Markus Müller

Dr. Luis Alonso Gallardo Delgado

Dr. Sergio Chávez Pérez

Dr. Diego Ruiz Aguilar
Coordinador del Posgrado en Ciencias de la Tierra

Dra. Ana Denise Re Araujo
Directora de Estudios de Posgrado

Resumen de la tesis que presenta Ana Lucía Ramos Barreto como requisito parcial para la obtención del grado de Doctor en Ciencias en Ciencias de la Tierra con orientación en Sismología.

Propagación de ondas sísmicas en medios fracturados saturados con fluidos

Resumen aprobado por:

Dr. Jonás de Dios de Basabe Delgado
Thesis director

El efecto de los fluidos dentro de las fracturas en la propagación de ondas elásticas sigue siendo un tema complejo y actualmente investigado. En particular, relacionar viscosidad y densidad del fluido con el comportamiento de las ondas en medios fracturados saturados con fluidos representa un desafío, y la literatura actual no ofrece conclusiones definitivas. Además, la modelación numérica añade dificultades por la pequeña escala de las fracturas frente a la longitud de onda. Para abordar estos desafíos, este estudio combina mediciones de laboratorio y simulaciones numéricas con el fin de investigar la influencia de la viscosidad y densidad del fluido en la propagación de ondas P y S en medios fracturados saturados. La configuración experimental consiste en el apilamiento de discos de aluminio para simular fracturas paralelas horizontales, saturadas con aire, agua, aceite de silicón o miel, en configuraciones de 1, 5 y 10 fracturas. Se determinaron las conformidades para regimen estático y dinámico, para las componentes normal y tangencial, bajo condiciones secas y saturadas. Estas mediciones se incorporan en simulaciones numéricas de propagación de ondas elásticas con el Método de Galerkin Discontinuo con Penalización Interior (IP-DGM), con la integración del Modelo de Deslizamiento Lineal (LSM) para representar fracturas explícitamente. Los resultados experimentales indican que las conformidades son mayores en el régimen estático que en el dinámico, y que ambas disminuyen conforme aumenta el número de fracturas. Asimismo, se observa una diferencia marcada entre condiciones secas y saturadas. En este último caso, la densidad del fluido se correlaciona positivamente con la velocidad de la onda P, su coeficiente de transmisión y el factor de calidad. Para la onda S, estos parámetros presentan un comportamiento cóncavo hacia arriba en función de la densidad del fluido. Las simulaciones numéricas reproducen adecuadamente estas tendencias y permiten diferenciar con claridad los distintos fluidos. Sin embargo, subestiman ligeramente la atenuación. Las simulaciones confirman que los fluidos más densos favorecen la transmisión de las ondas al reducir el contraste de impedancia entre las interfaces de la fractura, mejorando el acoplamiento y reduciendo retrasos en el arribo como la atenuación. En conjunto, los resultados experimentales y numéricos demuestran la capacidad de IP-DGM combinado con la conformidad de la fractura obtenidos experimentalmente, para modelar con precisión la propagación de ondas en medios fracturados y saturados con fluidos viscosos. Esta metodología proporciona información valiosa sobre la sensibilidad de las ondas sísmicas a las caracteriticas de las fracturas y los fluidos que las rellenan, con implicaciones importantes para el monitoreo sísmico de yacimientos fracturados y otras aplicaciones geofísicas.

Palabras clave: Fracturas saturadas con fluidos, pruebas ultrasónicas, conformidad de fractura

Abstract of the thesis presented by Ana Lucía Ramos Barreto as a partial requirement to obtain the Doctor of Science degree in Earth Science with orientation in Seismology.

Seismic wave propagation in fractured media saturated with fluids

Abstract approved by:

PhD Jonás de Dios de Basabe Delgado
Thesis Director

The effect of fluid within fractures on elastic wave propagation remains a complex and actively researched topic. In particular, establishing clear relationships between fluid viscosity, density, and wave behavior in fractured media presents significant challenges, with current literature offering no definitive conclusions. Accurately modeling fractures in wave-propagation simulations is further complicated by their small scale relative to the wavelength and other geological features. To address these challenges, combined laboratory measurements and numerical simulations are used to investigate the effects of fluid propertiesparticularly viscosity and densityon P- and S-wave propagation in fractured media. The experimental setup consists of stacked aluminum discs to mimic parallel horizontal fractures, which are filled with air, water, silicon oil, or honey. I examined configurations with 1, 5, and 10 fractures and determined static and dynamic, normal and tangential fracture compliances under dry and saturated conditions. These measurements are incorporated into elastic wave simulations using the Interior-Penalty Discontinuous Galerkin Method (IP-DGM) coupled with the Linear Slip Model (LSM) to explicitly represent fractures. Laboratory results show that P-wave velocity, transmission coefficient, and quality factor increase with fluid density, while they decrease with increasing fracture number. For S-wave, the results reveal a concave upward tendency on fluid density that is consistent across different fracture numbers. Fracture compliance-both normal and tangential- differ between dry and saturated conditions and tend to decrease as the number of fractures increases, with static values generally exceeding dynamic ones. Numerical simulations show good consistency with experimental observations, successfully discriminating between fluids, although numerical attenuation tends to be slightly underestimated. Furthermore, higher-density fluids enhance wave transmission by reducing the impedance contrast across fracture surfaces, thereby improving coupling and minimizing wave-front delays and amplitude attenuation. Overall, these findings highlight the ability of IP-DGM, combined with laboratory-derived fracture parameters, to model wave propagation in realistic fractured and fluid-saturated media accurately. This integrated approach provides valuable insights into the sensitivity of seismic waves to fracture and fluid characteristics, with important implications for seismic monitoring of fractured reservoirs and related applications.

Keywords: Fluid-filled fractures, ultrasonic tests, fracture compliance

Dedication

With all my heart and soul to God, whose infinite grace, love, and mercy sustained me throughout this journey. To my family, for their unwavering support, encouragement, and prayers, which gave me the courage to persevere.

"The grace of our Lord was poured out on me abundantly, along with the faith and love that are in Christ Jesus." 1 Timothy 1:14.

Acknowledgments

First and foremost, I wish to thank God once again for all the people who, in one way or another, have been involved in this project. I would like to express my gratitude to the Center for Scientific Research and Higher Education of Ensenada, Baja California (CICESE) for the opportunity to study here, and to SECIHTI for the financial support, which made this PhD possible. I am sincerely grateful to my advisor, Dr. Jonás de Basabe, for his patient, guidance and support throughout these years. I am also deeply thankful to my thesis committee: Dr. Sergio Chávez, for his academic advice and life lessons; Dr. Tobias Müller, for his attentiveness and insightful questions which fueled my progress even from the other side of the world; and Dr. Luis Gallardo, for his thoughtful questions, kindness and humility, which have truly marked my life. I feel very privileged to have worked with all of you.

I also appreciate the support of Sistemas de Laboratorios Especializados (SLE) at CICESE and Rubén Rioyos for his valuable collaboration in the laboratory. I am grateful to the Supercomputing Lab for providing me access to Lamb cluster, an essential tool for this research. I am deeply thankful to Dr. Pratap Sahay, for the encouragement in every conversation we had. Thanks also to the members of the Rock Physics Group, especially Gabriel Mejía for his kind friendship all the time and to Josué González for his valuable comments on the project. I would also like to thank all the teachers from whom I received knowledge; Dr. Javier Alejandro González, MsC. José Guadalupe Acosta. Maybe I did not take formal classes, but your conversations contributed to my academic formation; Dr. Juan Manuel Romo, Dr. Carlos Flores, Dr. Enrique Gómez, Dr. Diego Ruiz , Dr. Marco Pérez. As well as the administrative staff at CICESE for their support throughout my studies, specially Melissa Corral, who was always attentive to the documents needed to meet all administrative requirements.

I also thanks all of my friends and colleagues in the Earth Science division: Alejandra Sánchez, Betty Váldez, Jessica Salas, Favio Cruz, Nacho García, Jorge Castro, Daniel Rendón, Mariana Gómez, Thalia Avilés, Sebastián Camacho, Carlos Reinoza and Luis Yegres. Specially Naye Chacón, Tati Valencia, Francy Carvajal and Caro Balbuena, four different times just one heart.

To my family and dearest friends across México; the Mendoza-Bermeo family, who always opened their home with a warm heart; Laura Rosique, Gaby Vera, Eri Orantes, Dianita Vargas, Jaime Urías and Viri Vázquez (thanks for the DOI task), who have always been there through phone calls or messages; and

my special friend Deysy Cruz, who is on the other side of the line with words of encouragement, a warrior of prayer, thank you for all of them. I would also like to thank my Colombian friends; Tafur, JC, Andre, Yili and Vane, friends of many years with whom I have shared special moments, and who have followed and supported my progress across time and distance.

Special thanks to my purrfect companion, Galena, who accompanied me from the beginning and during the pandemic period, to the Barrón-Platero family, who never hesitated to provide a safety, lovely and peaceful place to live in Ensenada, and to my beloved church community, which has been a source or joy ans support. Thanks to the Radiantes women Eunice, Noemy, Alejandra, Lupita T and Yesi, who have been with me throughout this process and specially to Eddha Cabrera, my soul sister, partner in crime, and prayer mate, for listening and always being there. Thanks for holding me up when I could not continue.

Finally, I wanted to express my deepest gratitude to my dear friend Paco Carranza, for all the support in and outside CICESE, for standing by me in the most difficult moments of my health issues, and all the time we shared. To my beloved family in Colombia, despite the distance, thank you for holding my dreams, being my refugee, for your patient and understanding when I could not be there, for the countless ways you reminded me I am never alone, and staying with me in spirit through every moment.

Table of contents

Page

List of figures

Figura Página

List of tables

Chapter 1. Introduction

1.1 Fractures, and their effects on Seismic Wave Propagation

Fractures are critical structures that influence not only fluid dynamics and material strength but also the propagation of seismic waves, which makes them key targets in subsurface characterization. Their presence significantly impacts various geological and engineering applications, including hydrocarbon extraction, geothermal energy, groundwater management, underground construction, and CO_2 sequestration (Tsang et al., 2005, 2015; Iding & Ringrose, 2009). Understanding how seismic waves interact with fractures provides a practical means for their detection and characterization (Tsvankin & Grechka, 2011).

Fracture properties influence seismic wave propagation through mechanisms such as scattering, attenuation, and velocity dispersion. Parameters like fracture density and orientation primarily control the macroscopic response of the fractured medium. At the fracture scale, parameters such as aperture and infill properties influence the mechanical behavior of individual fractures, and are encapsulated in the concept of fracture compliance (or its inverse, stiffness). Fracture compliance, representing the ease of normal or shear deformation across a fracture, thus integrates the effects of these local properties and plays a critical role in controlling wave transmission and reflection, making it a central parameter in both experimental and theoretical seismic analyses.

Fracture compliance, characterizes the mechanical response of a fracture to applied stress and is widely used in both laboratory and modeling studies. It can be measured using static mechanical tests or dynamic ultrasonic methods (Goodman et al., 1968; Pyrak-Nolte et al., 1987; Lubbe et al., 2008; Hobday & Worthington, 2012), and is particularly sensitive to fluid properties, fracture roughness, and in situ stress conditions. As such, compliance is a crucial parameter for interpreting wavefracture interactions and assessing fracture properties from seismic data.

Seismic waves can be used to detect fracture zones and infer their properties, offering a non-invasive approach to subsurface characterization. While extensive research has been conducted on dry fractures (Pyrak-Nolte et al., 1990a; Cai & Zhao, 2000; Zhu et al., 2011), fewer studies have thoroughly explored how fluid properties within fractures influence wave behavior. Laboratory experiments by Pyrak-Nolte et al. (1990b) demonstrated that fluids within fractures can amplify both compressional and shear waves. This amplification is attributed to the increased effective stiffness of the fracture and the viscous coupling

between the fracture surfaces, which enhances wave transmission. Hsu & Schoenberg (1993) further investigated the role of fluid properties by measuring fracture compliance under different saturations (air and honey), demonstrating that it varies with fluid saturation and static stress. Furthermore, Guo et al. (2018) developed a theoretical model to investigate how fluid properties in combination with fracture thickness influence P-wave dispersion and attenuation through scattering. Using the Foldy approximation and representation theorem, they linked these wave phenomena to the displacement discontinuities across fluid-saturated fractures. Their results highlight the strong influence of fracture thickness and fluid compressibility, while showing that viscosity effects were negligible under their tested conditions.

Yang et al. (2019) experimentally studied the effects on P-waves of varying fracture thickness when saturated with water. They further investigated the influence of different fluid-saturation percentages within the fracture, considering water, light oils, and mixed compositions, on P-wave propagation in the ultrasonic band (Yang et al., 2020). They observed that an increase in fracture thickness leads to greater wave attenuation. For a specific fracture thickness, a higher proportion of water content, compared to light oils, reduces wave attenuation, increases P-wave velocity, and increases transmission. These variations were attributed to changes in the fluid compressibility and viscosity. Remarkably, these studies found that liquids with lower viscosity exhibited greater wave transmission and reduced wave attenuation across the medium.

However, these findings contrast from those of Clarke et al. (2020), who observed that increased viscosity and bulk modulus of the saturating fluid resulted in greater P-wave velocities and reduced wave attenuation. Their study, focusing on volcanic rocks, explored the impact of varying viscosity and bulk modulus of the saturating fluid on P-wave attenuation and velocity. The discrepancies in these studies may arise from the complexity of porous rocks, where multiple interactions between fluid-filled fractures and the surrounding rock matrix complicate the direct influence of fluid-filled fractures embedded in an elastic medium.

Numerical and theoretical research has complemented experimental findings, providing evidence of the impact of fluid properties on fractures based on different models. A study by Zhu et al. (2012) used a layered medium model in a numerical parametric study and concluded that fluid viscosity significantly affects wave transmission, with higher viscosity leading to increased attenuation. In contrast, Rao & Wang (2015) in their numerical study, found that seismic attenuation is only weakly sensitive to viscosity, based on simulations involving fractures with varied physical properties.

Collectively, experimental, numerical, and theoretical studies highlight the significant influence of fluid properties on wave propagation in fractured media. The discrepancies observed across studies emphasize the complexity of fracture-fluid interactions, particularly in porous rock matrices, where additional interactions between the host medium and fractures can further influence wave behavior.

1.2 Models for seismic propagation in fractured media

In practical: inverse problems, seismic detection of fractures is often based on equivalent-media theories, which mimic the seismic response of fractured rocks. These models simplify fractures by assuming properties such as shape, aperture, length, surface roughness, and connectivity (Liu & Martinez, 2012). Fractures may be substituted by ellipsoidal cracks, slip interfaces, displacement discontinuities or, more complexly, as fractal networks. Some approaches based on equivalent-medium theories include the Muir Model (Muir, 1972), which approximates fractures as aligned cracks in a homogeneous medium, and the Hudson Model (Hudson, 1981), which treats fractures as penny-shaped cracks embedded in a solid medium. These models aim to approximate fractured media by averaging fracture properties into an effective homogeneous medium. The Linear-Slip Model (LSM) (Schoenberg, 1980) stands out for its focus on displacement discontinuities across fractures and its ability to incorporate fracture compliance offering a more detailed framework for modeling fracture behavior.

LSM is widely accepted for modeling fractures, particularly for describing the mechanical behavior of fractures through discontinuity of the displacement across the fracture interface. The model is formulated in terms of fracture compliance and does not rely on assumptions about the microstructure and microgeometry of fractures (Bakulin et al., 2000). In addition to the displacement discontinuity, Pyrak-Nolte et al. (1990b) introduced a velocity discontinuity to account for the effects of viscous coupling due to the presence of fluids in fractures. This velocity discontinuity is described by a specific viscosity, which is defined by the ratio between the stress across a fracture and the resulting velocity discontinuity.

While theoretical models provide valuable insights into fracture behavior. Numerical modeling enable more flexible simulations of seismic wave propagation through fractured media, particularly when dealing with irregular fracture geometries, heterogeneous material properties, and fluid interactions that are difficult to capture with analytical models. However, accurately modeling seismic wave propagation through fractured media is challenging for numerical simulations as well, due to the scale disparity between fractures and the numerical grid resolution (Hall & Wang, 2012).

A common method for simulating wave propagation in fractured media is to use an equivalent medium (Schoenberg, 1980; Hudson, 1981). While this approach simplifies calculations, it does not capture the individual discrete effects of fractures on elastic waves. Thus, it becomes less effective when fracture spacing is comparable to or larger than the wavelength, as single or sparsely fractures can significantly influence wave propagation (Pyrak-Nolte et al., 1990b).

An alternative approach is to explicitly model fractures within wave-equation simulations, maintaining their mechanical influence on elastic waves. Several numerical methods have been developed for this purpose. The Finite-Difference Method (FDM) is widely used but struggles with handling discontinuities at interfaces (Coates & Schoenberg, 1995; Vlastos et al., 2003). Traditional Finite Element Methods (FEM) are also common (Hughes, 1987), but they face challenges in capturing the discrete nature of fractures, particularly when dealing with fluid-filled fractures where wave behavior is influenced by both mechanical and hydraulic properties. The Spectral Element Method (SEM) offers high accuracy but assumes continuity of the wave field at element interfaces (Komatitsch & Vilotte, 1998; Martin et al., 2008). On the other hand, the Discontinuous Galerkin Method (DGM), while computationally demanding, is particularly well-suited for modeling discrete fractures due to its ability to handle any type of discontinuity in the wave field (De Basabe et al., 2008, 2016; Duru et al., 2019).

The Discontinuous Galerkin Method (DGM) was first used to model fractures in fractured media with the incorporation of LSM under the scheme of the Interior-Penalty Discontinuous Galerkin Method (IP-DGM) for elastic wave propagation by De Basabe et al. (2016). This integration allows fractures to be explicitly modeled, preserving their discrete influence without averaging their effects, and accurately capturing localized fracture dynamics. By incorporating LSM into IP-DGM, the flexibility and precision of elastic wave simulations in complex geometries and fluid conditions are enhanced. A related implementation using the Nodal Discontinuous Galerkin method was developed by Möller & Friederich (2019), where fractures with various rheologies are modeled through additional numerical fluxes based on LSM.

DGM is a powerful numerical technique for simulating wave propagation in fractured media, particularly due to its ability to explicitly model fractures. This makes DGM highly effective for representing complex fracture geometries while minimizing numerical dispersion. A recent study by Pyrak-Nolte (2019) employed DGM to investigate wave propagation across single fractures in a 2D isotropic medium, analyzing the impact of fracture geometry on wave attenuation. Other research, such as Pyrak-Nolte et al. (1990a) and Rioyos-Romero et al. (2022), compared the effects of discrete fractures on seismic anisotropy using LSM and the effective moduli method. These studies found that the effective moduli method fails to capture the discrete nature of fractures, while LSM preserves the localized effects of fractures, effec-

tively capturing anisotropy in wave propagation. In an elastic medium with parallel fractures, factors such as wave frequency, fracture stiffness-to-seismic impedance ratio, and angle of incidence affect wave velocities and transmission coefficientseffects that are lost in effective-medium models unless they are modified with complex moduli, transforming the medium from elastic to viscoelastic.

1.3 Hypothesis and Research Objectives

Despite extensive research on wave propagation in fractured media, open questions remain regarding the influence of fluid properties, particularly density and viscosity (here understood as the shear viscosity of a Newtonian fluid), on fracture compliance and seismic wave behavior. Specifically, the relationship between normal and tangential fracture compliance and fluid density requires further investigation. Additionally, the effect of fluid viscosity on wave attenuation remains unclear, with conflicting findings in existing literature.

From this context, the following research questions are posed: How does normal and tangential fracture compliance relate to fluid density?, Can the normal-to-tangential compliance ratio serve as an effective fluid indicator, and how does it scale with fluid density?, What is the relationship between seismic wave attenuation and fluid viscosity?.

Hypothesis

Variations in fracture fluid density and viscosity produce measurable changes in normal and tangential fracture compliance, which in turn control the propagation characteristics of P- and S-waves in fractured media. If these compliance parameters are accurately quantified through laboratory experiments, they can be used as inputs to numerical simulations to reproduce the observed wave behavior.

Objectives

To assess this hypothesis, the objectives of this study are:

- Quantify normal and tangential fracture compliance under controlled variations of fluid density and viscosity using mechanical and ultrasonic laboratory measurements on artificial fractures in an aluminum medium.
- Integrate the measured compliance parameters into numerical simulations based on the Interior-

Penalty Discontinous Galerkin Method (IP-DGM) with the Linear Slip Model (LSM) to compare synthetic seismograms with experimental results to assess the validity of the approach.

1.4 Outline

Chapter 2 provides an overview of the theoretical framework for this study. It explores the characteristics of fractured media, fracture compliance, and the role of fluid-filled fractures in seismic wave propagation. It also introduces LSM as the framework to represent fracture effects. Chapter 3 presents a detailed description of the laboratory experiments, including the experimental setup, methodologies employed to estimate both static and dynamic fracture compliance; key parameters estimated for subsequent application in the numerical modeling. Chapter 4 focuses on numerical modeling. outlining IP-DGM. It describes the weak formulations used and the numerical models developed to simulate wave propagation in fractured media saturated with fluids. Moving forward to Chapter 5, it presents the results obtained from both laboratory experiments and numerical simulations. It includes fracture compliance measurements, observed waveforms, key seismic parameters, and numerical analyses of displacement fields under varying fracture number and fluid types, and also discusses the comparison of numerical simulations with laboratory observations, and Chapter 6 presents the concluding remarks.

Chapter 2. Theoretical background

Understanding the basic physics of seismic wave propagation is essential before addressing the more complex case of fractured and fluid-filled media. This chapter begins with the fundamentals of seismic wave propagation in elastic media, followed by a discussion of the main characteristic of fractured rocks and the effects of fluid-filled fractures on wave behavior. The concepts of fracture compliance and the theoretical model describing wave propagation across fractures, with emphasis on the Linear Slip Model.

2.1 Seismic wave propagation: basic concepts

Seismic waves propagate through the solid Earth because its materials, though rigid, can undergo internal deformation. Any disturbance within the Earth or material can therefore generate seismic waves, which carry information not only about the source of the waves but also about the properties of the materials they travel across.

Ar the fundamental level, seismic wave propagation is governed by the relationship between stress and strain tensor in the material. Stress represents the internal forces acting on a deformable continuous medium, while strain quantifies the resulting deformation. In its simplest one-dimensional form, stress and strain are proportional:

$$\sigma = E\epsilon, \tag{1}$$

where σ is stress, ϵ is strain and E is the stiffness of the material or Young's modulus. This proportionality illustrates that the way a material responds to deformation controls how seismic waves travel. A more complete mathematical formulation, including the elastic wave equation and tensor-based stress-strain relations is presented in Chapter 4.1.1.

The equation of motion for an elastic medium yields two solutions, representing the two types of elastic waves. Body waves travel through the material or Earth's interior and include: (a) **Compressional (P-) waves**, with particle motion or displacement parallel to the propagation direction and (b) **Shear (S-) waves**, with particle motion or displacement perpendicular to the propagation direction (Figure 1). Their velocities depend on the medium's elastic moduli and density:

$$V_p = \sqrt{\frac{\lambda + 2\mu}{\rho}}, \quad V_s = \sqrt{\frac{\mu}{\rho}}, \tag{2}$$

Where λ and μ are the Lamé parameters, and ρ is the density. These relations underscore that S-wave propagation is only possible in media with nonzero shear modulus, explaining why fluids supports only compressional waves. As body waves travel through the material, they undergo reflection, refraction and mode conversion at interfaces where material properties change. In addition to body waves, there exist surface waves, which propagates along the material's surface and arise either from a type of S-wave or form a combination of P- and S-waves. Surface waves typically produce the largest ground displacements. The two principal are: Rayleigh waves, with retrograde elliptical particle motion in the vertical plane, and love waves, characterized by horizontal shear motion confined to near-surface layers.

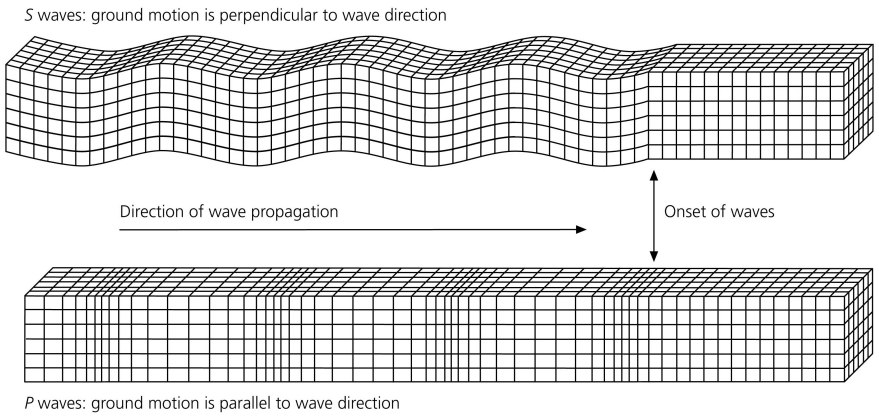

Figure 1. Displacements produced by P- and S- waves. P-wave produce displacement in the direction of wave propagation and S-wave produce displacement perpendicular to the direction of wave propagation (Stein & Wysession, 2003).

The propagation of seismic waves is also affected by material anisotropy, which occurs when a medium exhibits direction-dependent properties. In anisotropic media, wave velocity and attenuation vary with direction, reflecting the alignment of minerals, fractures, or layering within the rock.

Finally, attenuation and dispersion provide additional insights into material properties. Attenuation can result from viscoelastic behavior, scattering due to heterogeneities, or fluid-filled fractures, while dispersion arises when wave velocity depends on frequency. These effects are key for linking laboratory measurements, numerical simulations, and field observations in seismology and rock physics.

Since these effects are strongly influenced by discontinuities, it is natural to extend to fractured media. It have long been recognized as a critical factor in controlling the mechanical and hydraulic behavior of the Earth's crust. Since the early studies in rock mechanics and reservoirs engineering in the mid-20th century, researchers have worked to understand how fractures, whether isolated or in complex networks, alter the propagation of seismic waves. Their presence can significantly modify the elastic response of rocks, influence energy scattering and attenuation, and serves as pathways for fluid migration. Building

on this, the following section outlines the main characteristics of fractures and their implications for seismic wave behavior.

2.2 Fractured media: Characteristics and effect on seismic waves

Fractures can be described as natural rock discontinuities that occur when stresses exceed the rock's rupture strength (Aguilera, 1998). A fractured rock or geological formations is characterized by their textural properties of their individual fractures in combination with their bulk rock properties. The fracture-specific parameters include their density , extent, aperture, surface roughness and infill material, which combined transform mechanical characteristics of an otherwise homogeneous, unfractured media into those of the actual fractured formation.

Geometric properties include fracture density, extent, and aperture. Fracture density can vary with some regions displaying higher concentration of fractures than others. The extent of a fracture ranges from "small" cracks of few millimeters to large fissures or faults up to several kilometers. Aperture refers to the separation between fracture surfaces, influencing the volume available for infill material.

Infill material refers to the substance occupying the space between fracture surfaces. Fractures may contain fluidssuch as water, oil, or gasor solid materials, both of which modify their response to external stress. Solid infill can result from erosion of the fracture walls by mechanical processes or from precipitated minerals deposited after fluid flow events. The type and phase of a fluid (liquid or gas) can significantly influence the behavior of seismic waves (Berryman, 2007). For the purposes of this study, only non-pressurized gas (air) and liquids are considered as infill materials.

Surface properties such as roughness ans shape irregularities also play a important role. Surface roughness refers to the distribution of asperities on fracture surfaces, providing a measure of how irregular or uneven the surface id. It reflects the extent and nature of deviations in asperity heights from a baseline or reference plane (Choi et al., 2014; Smith, 2021). Rough fracture walls can scatter and diffract seismic waves, altering their propagation. In this study, the roughness of fracture surfaces was characterized using a laser profilometer.

Orientation is another defining feature of fractures. An orderly arrangement, such as parallel fractures, can introduce anisotropy, in which the seismic waves direction of propagation interacts with fracture orientation. This anisotropy is particularly pronounced in stress-aligned fracture systems. Additionally,

scattering and diffraction at fracture surfaces contribute to wave attenuation and dispersion.

A useful parameter that synthesis some physical properties of the fractures, including their geometric complexity into a mechanical response of a fractured media is the compliance (Choi et al., 2014) - section 2.3.

Seismic attenuation and fracture-related wave phenomena

Attenuation describes the energy lost by a seismic wave as it propagates. This loss manifests as reduced amplitudes in higher-frequency components. Attenuation arises from four primary mechanisms: (1) geometrical spreading; (2) energy partition at discontinuities, such as fractures; (3) energy loss due to internal friction (intrinsic attenuation) and (4) wave interference or caused by small-scale heterogeneities (Shearer, 2019).

Fractures, in particular, following the last three mechanisms for instances, scatters fracture surface fronts producing a scattering attenuation (see figure 2). Fractures also significantly impact over wave features including, energy partition, refraction and mode conversion.

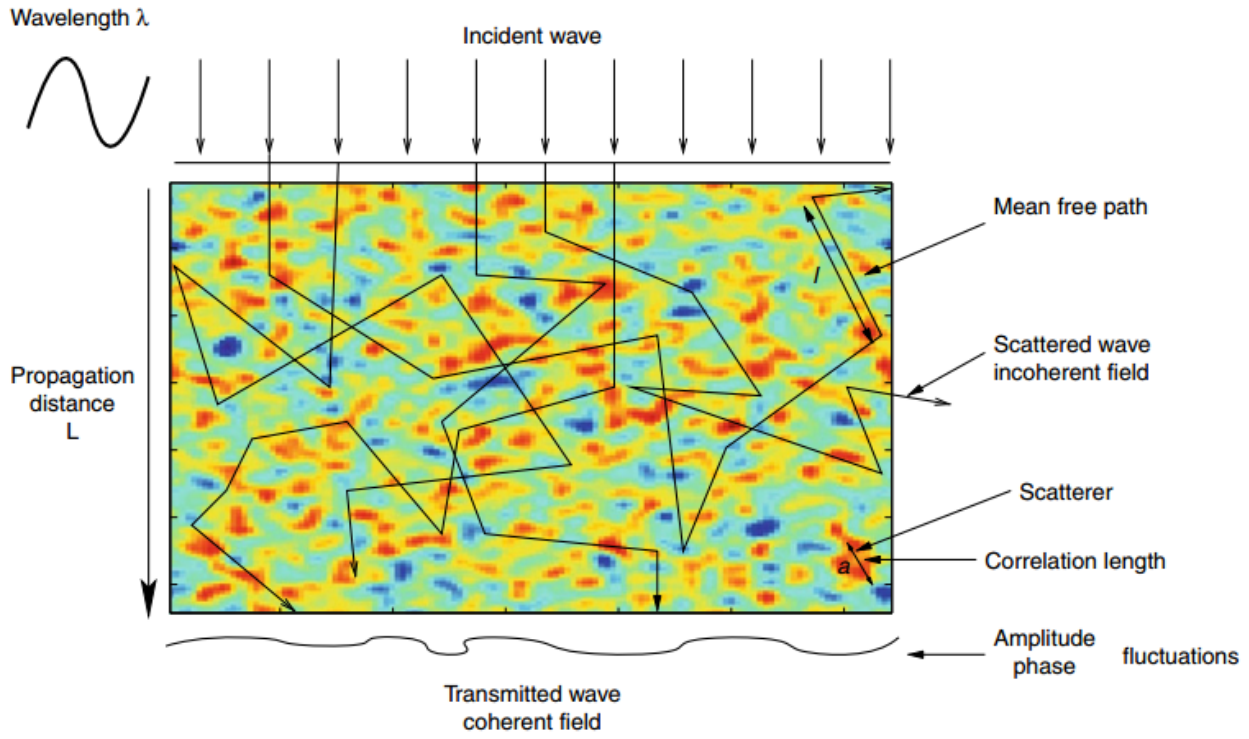

Figure 2. Scattering process of an incident plane wave propagating across a chunk of random medium of dimension L. As the plane wave progresses across the heterogeneous medium (represented by the space with colors blue, red, yellow and green) scattering operates and deflects energy in all space directions (black arrows in the medium), and the transmission wavefield is distorted and attenuated (Arora et al., 2011).

Reflection occurs when part of the wave energy returns at the fractures, providing valuable insights into subsurface structures. Refraction arises when waves are guided through fractures themselves; whereas involves the passage of seismic energy completely through the fractured medium. Additionally, fractures produce mode conversions, e.g., compressional wave converting to a shear wave. This study focuses only on the transmitted portion of the wave that reaches the receiver after traveling through the fractured medium.

2.2.1 Effect of fluid-filled fractures on seismic waves

The role of the fluids filling the fractures in seismic wave propagation is matter of current debate. Laboratory and field experiments have shown that the presence of fluids significantly influences the behavior of both P- and S-waves. In first approximation, the density and viscosity of the fluid can introduce changes in attenuation, dispersion and velocity of seismic waves. The interaction between seismic waves and fractures provides valuable insights into subsurface properties but also complicates geophysical data interpretation.

Wave Attenuation: The presence of fluids within fractures is generally expected to increase the attenuation (loss of energy) of seismic waves. This occurs because the fluids absorb and dissipate wave energy as the waves pass through the fracture. In viscous fluids, attenuation arises not only from bulk compressional effects but also from wave-induced shear deformation within small fluid volumes. As described by Mavko et al. (2020), this mechanism causes acoustic waves in viscous fluids to be both dispersive and attenuating, due to the shear contribution to wave-induced deformation. Experimental observations by Wei et al. (2024) confirm that higher viscosity fluids, such as glycerin, tend to cause greater attenuation compared to lower viscosity fluids like water. However, this relationship is not always straightforward. Under certain conditionsparticularly in rocks with high permeability or clay contentvery high viscosity fluids can suppress poroelastic fluid flow, leading to lower overall attenuation than predicted by conventional theory (Gurevich et al., 2010; Best, 1992). These findings highlight that attenuation depends on a complex balance between fluid viscosity, fracture, rock microstructure, and wave frequency, and may not always follow intuitive trends.

Velocity Changes: Although this study remains within the framework of elastic modeling and does not explicitly incorporate poroelastic effects, it is important to acknowledge the role of porosity in modulating seismic waves velocities in fractured media. Fluid-filled fractures can significantly alter both

P-wave and S-wave velocities, depending on the fluid properties such as density and viscosity. Ba et al. (2023) found that, at full fluid saturation, P-wave velocity increases with confining pressure, while attenuation decreases. However, higher porosity and permeability lead to increased attenuation. In gas-water conditions, seismic velocity increases, and attenuation peaks at intermediate saturations due to mesoscopic heterogeneities. These findings underscore the importance of fluid saturation and confining pressure in governing wave velocities in fractured media.

Wave Delay: Fractures typically introduce delays in seismic wave propagation due to their increased compliance (reduced stiffness), resulting in longer arrival times compared to intact rock. However, the presence of fluids within these fractures can alter this behavior significantly. Laboratory experiments by (Pyrak-Nolte et al., 1990b) demonstrated that the transmission of seismic waves across fractures is closely related to fracture stiffness, which increases with fluid saturation. Although they did not report arrival times explicitly, their displacement-discontinuity model shows that increasing the specific stiffness of a fluid-saturated fracture reduces phase delays, allowing waves to travel faster across the interface. This is particularly evident for P-waves, where fluid presence enhances coupling and leads to improved transmission. Similarly, Yang et al. (2020) conducted ultrasonic experiments on fluid-filled rock joints and observed that increasing the fluid contentespecially with waterconsistently led to higher wave velocities across the joint. They attributed this effect to the increase in bulk modulus and viscous coupling introduced by the fluid, which effectively stiffens the fracture and reduces its compliance. Taken together, these studies indicate that while dry fractures typically delay wave arrivals, the presence of fluidsdepending on their propertiescan mitigate this delay by enhancing fracture stiffness and facilitating faster wave transmission.

Acoustic impedance: Fluid-filled fractures can make subsurface fracture more detectable in seismic data by increasing the elastic contrast between the fracture and the surrounding rock matrix. This contrast, especially when the fracture contains fluids with significantly different acoustic impedance (e.g., water, oil, or gas), leads to stronger scattering and reflection of seismic waves. As a result, seismic energy is more likely to be scattered or reflected back to the surface or sensors, making the fracture more detectable in seismic imaging. Studies have shown that fluid-filled fractures cause amplitude anomalies, travel-time delays, and waveform distortions that can be used to infer the presence, orientation, and even the fluid content of the fractures (Pyrak-Nolte et al., 1990b; Schoenberg & Douma, 1988).

In general seismic waves are influenced by multiple factors, including the fluid properties (such as saturation, viscosity, and density), the fracture characteristics, and the frequency and amplitude of the seismic waves. The interaction between these factors shapes the overall response of the seismic waves.

For example, even small amounts of gas $(6\% - 8\%)$ can significantly alter attenuation and dispersion characteristics (Wei et al., 2024), with viscosity playing a key role in both energy dissipation and frequency shifts. Pimienta et al. (2016) found that fluid viscosity also affects Poissons ratio dispersion, with significant frequency-dependent variations caused by the fluid presence, influencing the waves frequency range.

2.3 Fracture compliance

Fracture compliance (Z) is a key parameter that integrates the main mechanical and geometrical properties of fracture, such as its surface roughness, contact area, and aperture into a single measure. It consists of two components, normal compliance, describing deformation perpendicular to the fracture plane, and tangential compliance, describing with shear deformation along the fracture plane (see sections 3.3.1).

In essence, compliance quantifies the fracture's ability to deform under applied stress, providing a practical characterization without requiring separate, detailed measurements of aperture, contact area ratio or roughness Goodman et al. (1968).

Normal compliance describes the fracture's ability to deform in response to a normal or perpendicular stress. It is particularly important when considering the effect of fractures on wave propagation, as it influences how fractures respond to compression or extension. Normal compliance can vary significantly depending on the properties of the surrounding rock.

Tangential compliance, on the other hand, focuses on the fracture's response to tangential or shear stress. It is crucial for understanding how fractures slide or slip in response to shearing forces. Tangential compliance can also be influenced by factors like surface roughness, fracture orientation, and the presence of infill materials.

Formally, fracture compliance is defines as the proportionality constant between the discontinuity in displacement across a fracture and the traction acting on it. $[\boldsymbol{\mathcal{U}}]$ denotes the relative displacement across the fracture and $\boldsymbol{\tau}^{\gamma}$ the traction vector on the fracture plane, then:

$$[\boldsymbol{\mathcal{U}}] = \boldsymbol{Z}\boldsymbol{\tau}^{\gamma}, \tag{3}$$

where $\boldsymbol{Z}$ is the compliance matrix. In an isotropic fracture, this matrix reduces to two scalar components:

the normal compliance Z_n and the tangential Z_t, which describe the response to normal and shear tractions, respectively.

Both normal and tangential compliance can be evaluated under different loading conditions, giving rise to the concepts of static and dynamic compliance. Static compliance reflects the deformation of the fracture under steady or slowly applied stresses, whereas dynamic compliance captures its response to oscillatory stresses such as those generated by seismic or ultrasonic waves. As highlighted by Pyrak-Nolte (1996), these parameters form a critical link between the hydraulic, mechanical and seismic properties of fractures, and are indispensable for realistic models of wave propagation in fractured media. The ratio of normal-to-tangential compliance, for example, serve as an indicator of fluid presence within fractures Liu et al. (2000).

Static compliance is typically determined through mechanical tests, such as uniaxial compression of specimens containing fractures. In these tests, normal compliance is obtained as the inverse of the slope of the displacement-stress curve, with loading and unloading segments revealing the fracture's deformation characteristics. Dynamic compliance, in contrast, is obtained from wave-base measurements. Seismic and ultrasonic laboratory experiments transmit high-frequency waves through fractured specimens to determine properties such as wave velocities and transmission coefficients, from which compliance can be inferred. Notably, static compliance values are often larger than dynamic ones (Pyrak-Nolte, 2019; Zhou et al., 2020). The table 1 present a compilation of laboratory and field estimates of normal and tangential compliance to both static and dynamic evaluation found in the literature, illustrating the range of values observed under different conditions.

2.4 Theory of elastic wave propagation across fractures

Although fracture effects on seismic waves are readily observable, their measurements can be influenced by multiple scattering and other phenomena that depend on the signal's wavelength as well as the size and distribution of discontinuities. To capture these effects, several modeling approaches have been developed, which can be categorized into three main types: scattering models, effective media models, and displacement discontinuity models (Suarez-Rivera, 1992).

Scattering models are suited for material containing small cracks. They predict velocity changes caused by the presence of cracks, as well as apparent attenuation due to energy scattering (Hudson, 1981).

Table 1. Reported values of static and dynamic fracture compliance under different conditions. (Modify from Hobday & Worthington (2012))

Compliance (m/Pa)	Normal stress (MPa)	Reference
Static		
1.0×10^{-13} 1.0×10^{-12}	2.211.5	Rutqvist (1995)
9.0×10^{-13} 1.0×10^{-10}	2.211.5	Rutqvist (1995)
2.27×10^{-12}	10	Makurat et al. (1991))
5.6×10^{-13} 2.6×10^{-12}	2527	Makurat et al. (1991)
2.8×10^{-13} 1.0×10^{-11}	4	Pratt et al. (1977)
1.2×10^{-13} 2.0×10^{-11}	230	Zangerl et al. (2008)
1.2×10^{-13} 1.0×10^{-11}	10	Giwelli et al. (2009))
5.0×10^{-13} 9.0×10^{-11}	10, 25	Barton (2006)
3.0×10^{-13} 1.0×10^{-12}	2.933	Pyrak-Nolte et al. (1987)
$> 5.0 \times 10^{-11}$	1.5	Evans & Wyatt (1984)
1.3×10^{-11} 1.7×10^{-10}	1.0	Jung (1989)
Dynamic		
7.8×10^{-16} 3.2×10^{-14}	10, 30	Lubbe et al. (2008)
5.0×10^{-15} 5.7×10^{-14}	10, 33	Pyrak-Nolte et al. (1990b)
8.3×10^{-14} 3.8×10^{-13}	1	Hardin et al. (1987)
3.5×10^{-12}	1	Lubbe & Worthington (2006)
2.0×10^{-12}	1	Myer et al. (1990)
1.7×10^{-13}	90	Prioul et al. (2007)
1.4×10^{-12}	Unknown	Prioul et al. (2008)

In this models the seismic waves are assumed to be uniformly scattered by the cracks. The cracks are small relative to the seismic wavelength and do not interact with one another. Additionally, the models account for the effect of viscous damping caused by liquids contained within the cracks, which contributes to intrinsic attenuation.

Effective medium models treat a fractured rock mass as a homogeneous equivalent material with modified elastic properties (O'Connell & Budiansky, 1977; Zimmerman & King, 1985; Sayers & Kachanov, 1991). When these properties accurately represent the cracked medium, the predicted variations in seismic velocity are equivalent to the those observed in the real rock. However, as the model assumes elastic behavior, it does not account for attenuation, except for cases when the cracks are filled with liquids.

Displacement discontinuity models explicitly represent fractures as internal boundaries within an otherwise elastic medium. Fractures are often idealized as infinitely long, planar interfaces. This framework allows direct incorporation of mechanical propertiessuch as complianceinto wave propagation equations.

Among these approaches, the Linear Slip Model (LSM) is particularly well suited for this study, as it provides a simple but rigorous frame to incorporate fractures into the equations of elastic wave propagation.

2.4.1 Linear slip model

The Linear Slip Model (LSM), originally proposed by Schoenberg (1980), idealizes a fracture as a planar interface of negligible thickness relative to the seismic wavelength, with large separation between asperities and between adjacent fractures. In this framework, the fracture is introduced mathematically as a boundary condition: stresses remain continuous across the interface, but displacements exhibit a discontinuity. As recalled in section 2.3, eq. 3, this discontinuity $[\boldsymbol{\mathcal{U}}]$ is linearly related to the traction vector $\boldsymbol{\tau}^{\gamma}$ through the fracture compliance $\boldsymbol{Z}$: $[\boldsymbol{\mathcal{U}}] = \boldsymbol{Z}\boldsymbol{\tau}^{\gamma}$. For an isotropic fracture, this matrix reduces to two components (Sayers, 2007):

$$Z_{ij} = Z_n n_i n_j + Z_t(\delta_{ij} - n_i n_j), \tag{4}$$

with Z_n denoting the normal compliance and Z_t the tangential compliance.

In a physical sense the meaning of fracture compliance in the LSM can be schematically illustrated by a spring (figure 3). In this analogy, a more compliant spring corresponds to a more deformable fracture, where higher compliance implies lower stiffness and greater relative displacement across the interface.

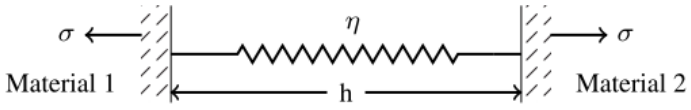

Figure 3. Schematic representation of a fracture compliance with compliance η, h is the thickness which $h \to 0$ in the LSM. Figure taken from Möller & Friederich (2019).

The LSM has been extensively studied and validated both theoretically and experimentally (Schoenberg, 1980; Pyrak-Nolte et al., 1990b,a; Lubbe & Worthington, 2006; Lubbe et al., 2008; Myer et al., 1990). It captures key fracture-induced effects on seismic waves, including changes in amplitude, frequency content, and group delay. Since it is formulated within an elastic framework, the model is inherently non-dissipative.

Nevertheless, dissipation can be incorporated. In classical applications, viscous fluids introduce energy loss through a velocity discontinuity at the fracture interface (Pyrak-Nolte et al., 1990b). In this research, however, fluid effects are embedded directly into the fracture compliance. By using dynamic compliance values derived from laboratory measurements, attenuation is indirectly represented, without explicitly modeling viscous or poroelastic mechanisms. Thus, attenuation is not explicitly modeled through viscous or poroelastic mechanism, but rather approximated through the adaptation of the LSM.

Chapter 3. Laboratory experiments

This chapter describes the laboratory work carried out at the **S**istemas de **L**aboratorios **E**specializados **(SLE)** at CICESE. The purpose of the experiments was to accurately estimate the compliance of single and multiple fractures filled with different kinds of fluids. I employed two distinct experimental approaches in this research: (1) deformation tests and (2) pulse transmission technique. The deformation tests facilitated the estimation of static normal compliance, while the pulse transmission technique enabled the determination of dynamic normal and tangential compliance. Moreover, the data recorded during ultrasonic tests allowed me to quantitatively analyze key wave parameters, i.e., wave velocity, transmission coefficient, and quality factor (Q). This analysis will offer valuable insights into the influence of viscosity and density on wave behavior.

3.1 Experimental set-up: specimens

For the laboratory experiments I opted for aluminum cylinders due to its low-attenuation properties. The experiments were conducted on four cylindrical specimens (aluminum type 6061). The specimens included one non-fractured and three fractured specimens, with the fractured specimens containing one, five, and ten equally-spaced fractures, respectively. To simulate fractures, I stacked aluminum discs of varying thicknesses, as illustrated in Figure 4.

The height of each fractured specimen matches the height of the intact specimen, as shown in Figure 4. The specimens measure 76.08 mm in height and 38 mm in diameter. The mechanical properties of the aluminum determined at the laboratory are: density ρ = 2702 kg/m^3, dynamic Young's modulus E = 71.3 GPa, and Poisson's ratio ν = 0.34. In addition the P- and S-wave velocities of aluminum, also measured at the laboratory were 6432 and 3133 m/s respectively. These velocities resemble those of low-permeability rocks such as limestone (P-wave velocity of 6315 m/s and S-wave velocity between 3170 and 3350 m/s) (Lubbe et al., 2008). This similarity further validates the aluminum as a material for the experiments.

I conducted the experimental tests under both dry and saturated conditions. For saturated condition, a small amount of fluid between the contact surfaces of each pair of discs were added. The fluids used were water (18 μL), silicone oil (12 μL), and honey. Water and silicone oil were measured using a micropipette; however, due to its high density, honey could not be measured with the same method. Instead, its volume was carefully controlled using alternative means to maintain consistency across

samples. Table 2 presents the properties of these fluids at room temperature. Here, viscosity refers especifically to the shear viscosity of newtonian fluid, defines as the proportionality between shear stress and strain rate, since only Newtonian fluids are considered in this work.

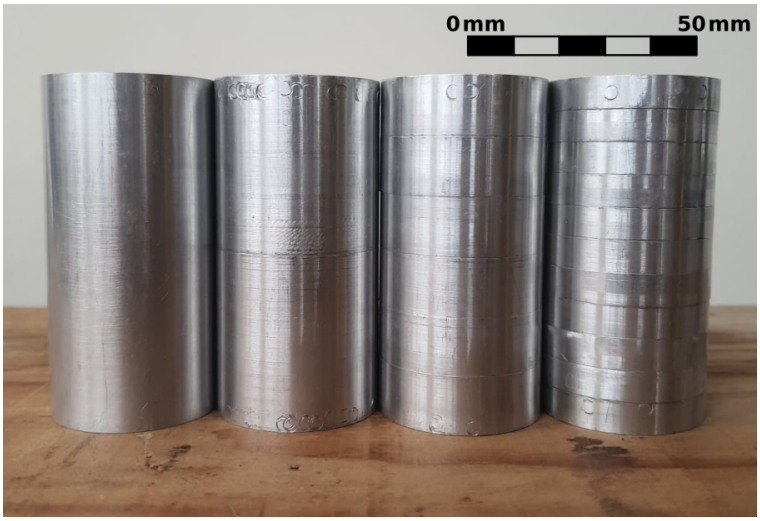

Figure 4. Aluminum specimens set, one intact (left) and the remaining are disc-stack models to mimic specimens with horizontal parallel fractures (from left to right: 1, 5 and 10 fractures).

Table 2. Physical properties of liquids at room temperature (20°C). Density ρ_f, shear viscosity η_f and bulk modulus K_f.

Fluid	$\rho_f(kg/m^3)$	$\eta_f\ (kg/m.s)$	$K_f\ (GPa)$
Air (Dry)	1.204	1.825×10^{-5}	1.01×10^{-4}
Silicon Oil	965.00	9.65×10^{-3}	1.6-1.8
Water	998.20	1.002×10^{-3}	2.0
Honey	1420.00	$2000 - 10000 \times 10^{-3}$	4.2-5.0

3.2 Experimental components

The experimental setup for the deformation and ultrasonic tests involved different components. The primary device is the *GCTS Rapid Triaxial Rock Testing System* (RTR-2000), a servo-controlled loading system capable of applying a maximum axial load of 210 MPa. In figure 5 the main components are depicted, which are a box load frame, and the closed-loop servo control of the axial load actuator.

The RTR-2000 is integrated with the *Ultrasonic Velocity Test System* console (ULT-200), which facilitates the execution of ultrasonic tests. This system comprises two steel platens equipped with integrated piezoelectric transducers, serving as wave sources and receivers (figure 6). The piezoelectric transducers

have a natural central frequency of 1 MHz, corresponding to a P- and S- wavelength of 6.43 mm and 3.13 mm respectively. The data acquisition is through the software *Computer Aided Ultrasonic Velocity Testing Software* (CATS) provided by GCTS.

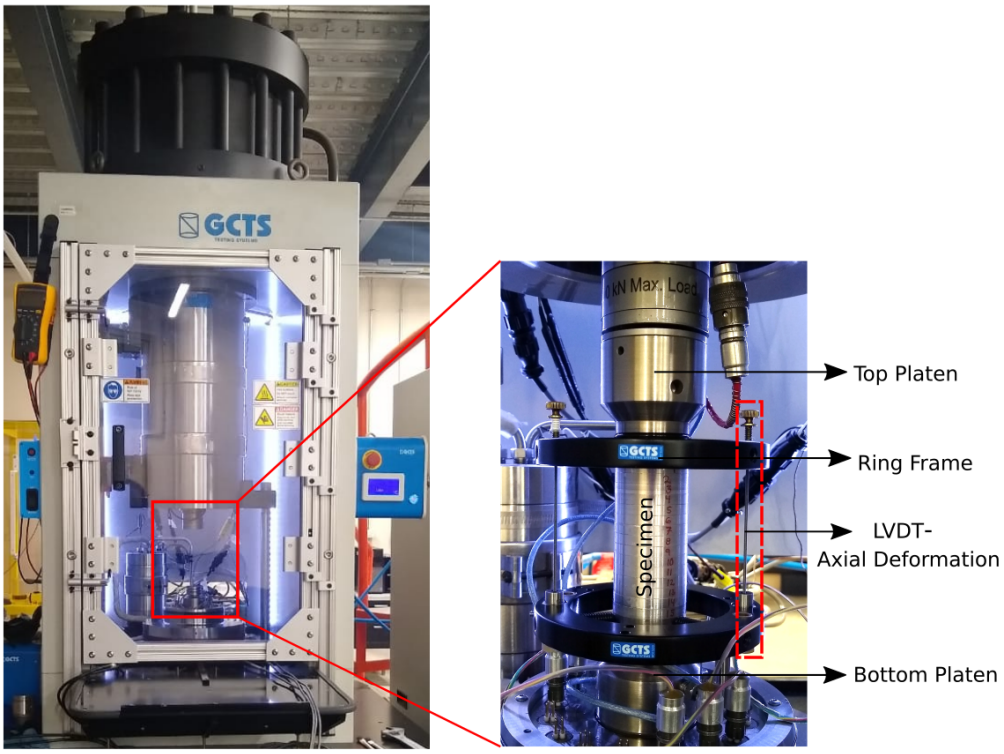

Figure 5. Left: Servo-controlled GCTS Rapid Triaxial Rock Test RTR-2000, the red rectangle corresponds to the connection base and load column. Right: connection base and load column where the platens and specimen are placed.

3.3 Deformation tests and static fracture compliance

The deformation tests involve conducting uniaxial compression tests on cylindrical aluminum specimens (intact and fractured) placed between the steel platens. Honey was used to ensure good contact between the platens and the specimen's ends. In these tests, a compression load is applied in one principal direction, normal to the fracture surface.

The specimens are initially fixed to a dual ring-frame structure to ensure precise alignment. Then, a pair of Linear Variable Differential Transformers (LVDTs) with a resolution of 0.1 μm are carefully installed on opposite sides of the ring frame (as illustrated in figures 5 and 7c). These LVDTs precisely measure the uniaxial deformation during both the loading and unloading cycles applied to the specimens.

After setting the LVDTs, the machine underwent calibration by performing a test on the intact specimen to obtain the Young modulus of the aluminum. The test sequence comprises two stages, each involving two loading/unloading cycles up to 50 MPa at a stress rate of 10 MPa/min. In the first, the objective is to stabilize the entire system by eliminating excess axial displacement caused by the coupling between the upper and lower discs with the platens. This coupling effect may introduce random variations in the measurement, which this first stage effectively mitigates.

Figure 6. Ultrasonic velocity test system (ULT-200).

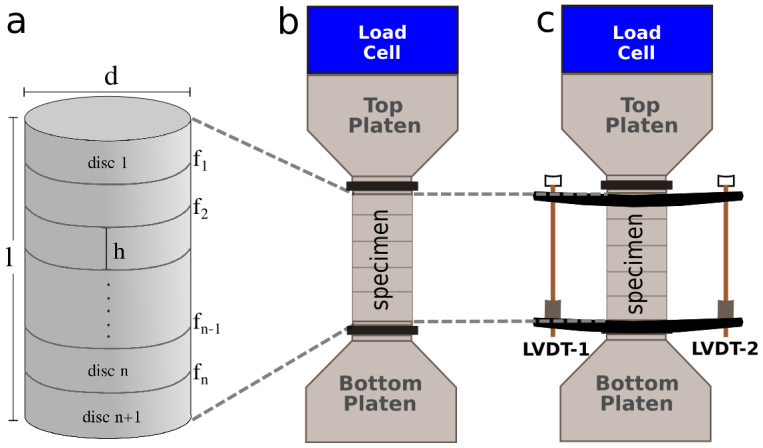

Figure 7. Schematic diagram of the experimental setup. (a) stack-disc for a specimen containing n horizontal-parallel fractures, where: d, cylinder diameter, l, cylinder length,f_i, i-th fracture, h, aluminum disc height. (b) configuration for the ultrasonic tests and, (c) configuration for the normal deformation tests, local LVDTs mounted on the specimen.

Following stabilization, the second stage focuses on recording the deformation experience by the aluminum specimen against the applied normal stress. This entire sequence is repeated four times, with the setup disassembled between each repetition to ensure the reproducibility of the results. The data obtained is presented in the normal stress-axial displacement curves for the intact and fractured specimens (Figures(8a, 8b, 8c).

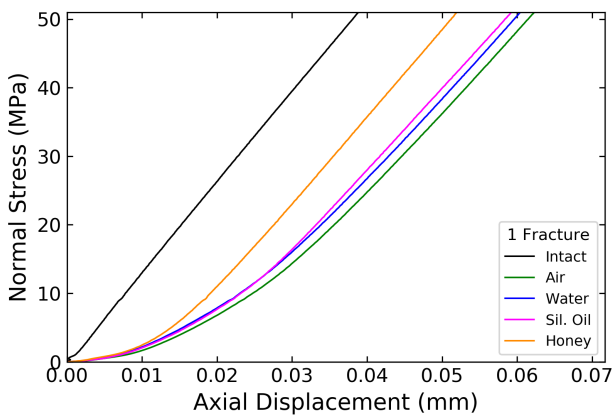

(a) 1 Fracture

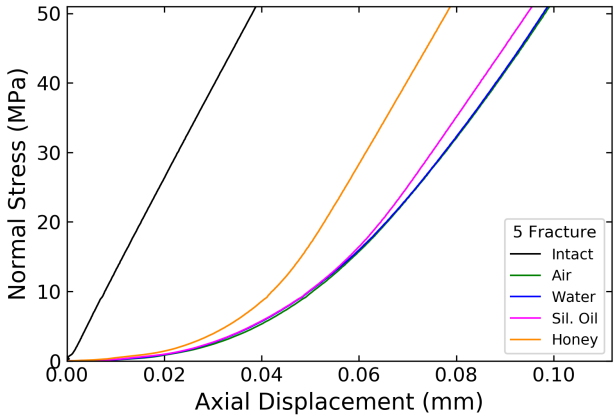

(b) 5 Fractures

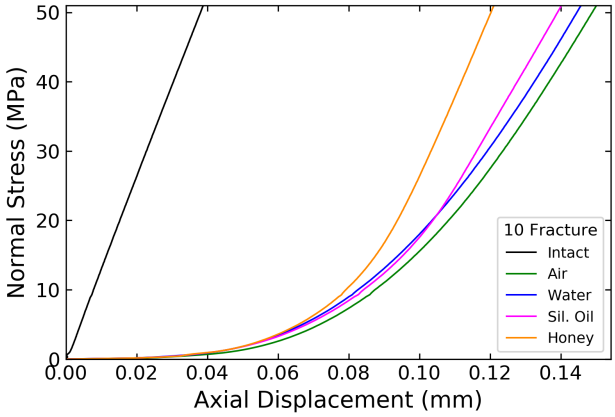

(c) 10 Fractures

Figure 8. Uniaxial normal stress-axial displacement curves for the intact and fractured specimens. The curves show the evolution of the axial deformation for each set of fractures versus normal stress. From these measurements, the normal static compliance is estimated.

For the fractured specimens, the total normal deformation includes both the deformation of the intact aluminum and the fractures. Thus, the final normal stress-displacement curve for each fractured specimen used to determine the normal static compliance is derived by subtracting the stress-displacement curve of the intact specimen (Goodman, 1976) as I will describe in the next section for clarity.

3.3.1 Static normal compliance determination

According to Goodman et al. (1968), the static normal compliance (inverse of the stiffness) is defined as the ratio between the average displacement Δd associated with the increment of applied stress $\Delta\sigma$:

$$\mathcal{Z}_n = \frac{\Delta d}{\Delta \sigma}, \tag{5}$$

hence, the normal static compliance is obtained from the inverse slope of the normal stress-displacement curves (Goodman et al., 1968; Pyrak-Nolte et al., 1990b; Zhou et al., 2020).

As I mentioned in the previous section, the determination of the normal static fracture compliance involve the data from the normal stress-axial displacement curve. The axial deformation measured on the fractured samples consists of two contributions: the deformation of the intact rock and an excess deformation attributed to the fracture. Hence, the excess of deformation and the final stress-displacement curve for each fractured specimen were obtained by subtracting the stress-displacement curve of the intact specimen from that of the fractured specimen for each normal stress (Goodman et al. (1968)). This excess deformation is commonly called fracture closure and increases as the fractures compress (Liu (2005)). A graphic representation of this process is shown in figure 9.

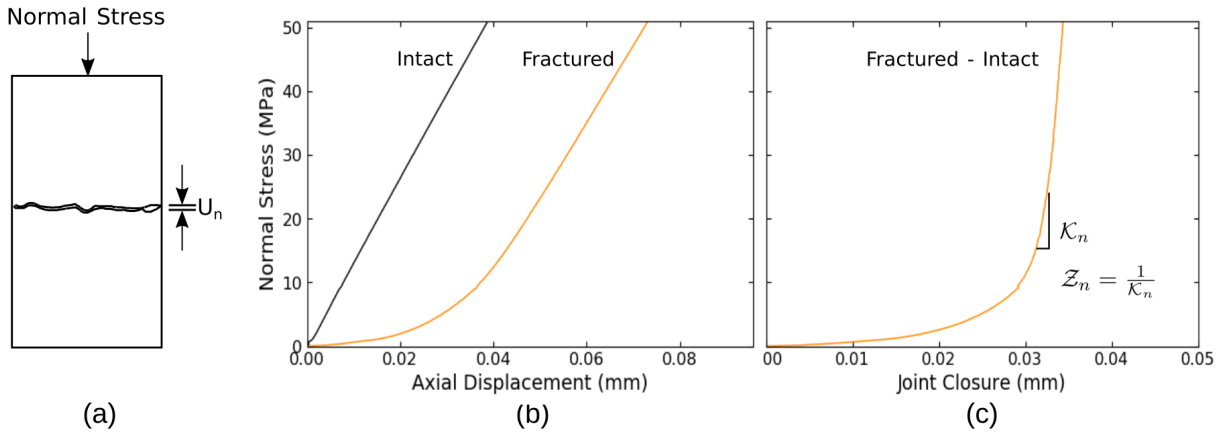

Figure 9. Normal fracture compliance. (a) Diagram of uniaxial normal loading on fracture and (b) normal stress- axial deformation curve of intact and fracture specimen and (c) and normal stress-fracture closure, and definition of normal static compliance $\mathcal{Z}_n$ (modified from Zhang et al. (2023)).

From the normal stress-fracture closure curves, I calculated the slope along the entire curve illustrating the trend of the normal static fracture compliance. This compliance varies not only as a function of the normal stress but as influenced by factor such as the number of fractures and the type of filling fluid as is shown in figure 10. The data depicted in the figure correspond to the value of individual fractures within each specimen, rather than reflecting the cumulative values across all fractures within the specimens.

After estimating the normal static compliance, the next step in the analysis involved the estimation of the static tangential compliance, the second parameter needed to characterize fractures. This parameter is estimated by relying on two models that establish the relationship between normal and tangential compliance, i.e. the ratio compliance for dry fractures. In these models, fractures are modeled as planar distributions of cracks.

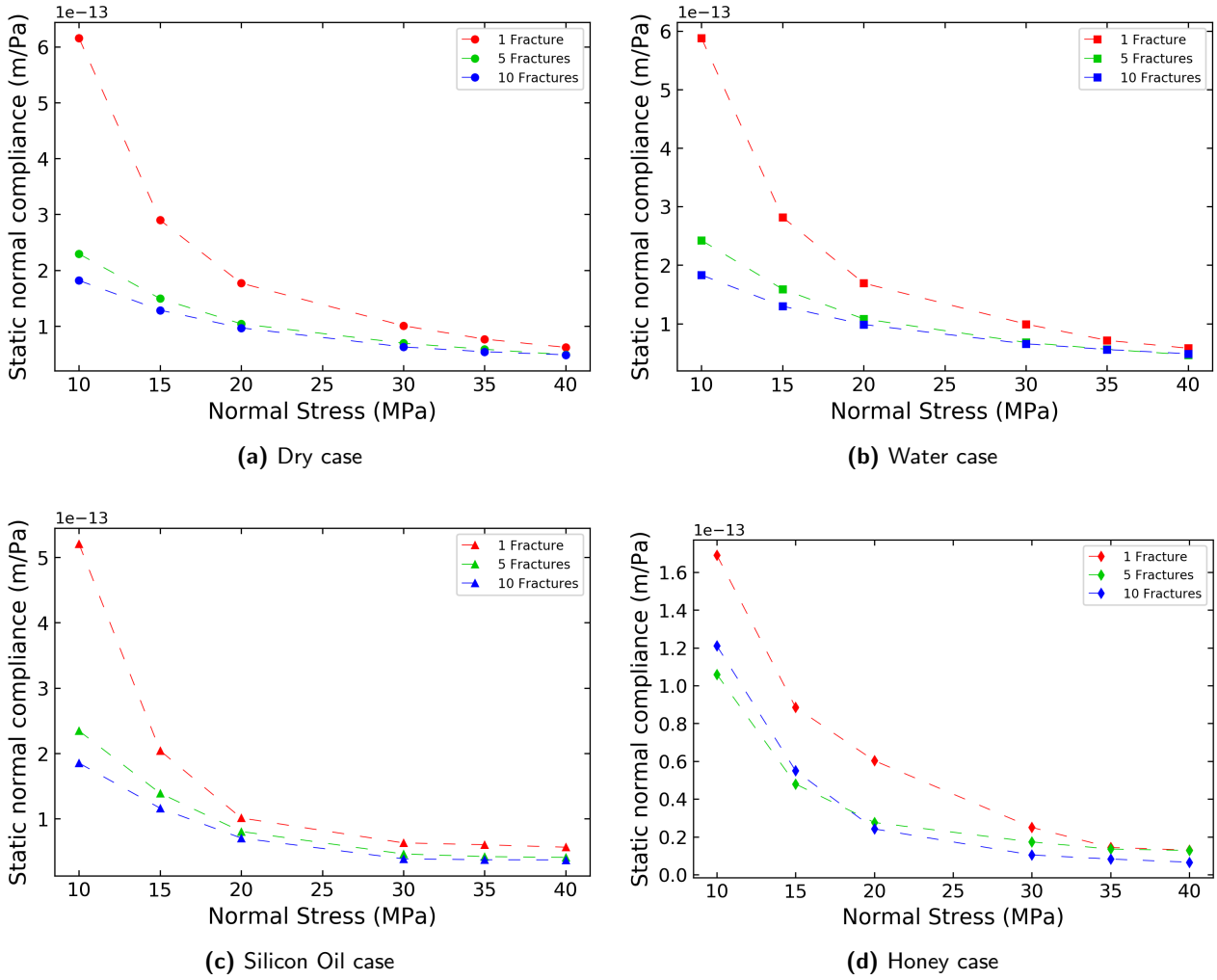

Figure 10. Normal Static compliance-Uniaxial stress curves for fractured specimens. The curves show the evolution of the normal static compliance versus normal stress. The plotted values for the cases of 5 and 10 fractures represent the characteristics values of a single fracture within each specimen, rather than the aggregate values of all fractures present.

The first model (M1), conceptualizes a fracture as a planar distribution of small isolated areas of slip or cracks (partial bond), while the second model (M2), establishes a fracture as a plane distribution of imperfect contacts or a rough surface. Despite being originally developed for dry fractures, in this study these models are extrapolated to fluid-filled fractures, as there are currently no available models in the literature that specifically address this scenario. The corresponding fracture compliances ratio are given by Liu et al. (2000), where ν is the Poisson's ration of the rock matrix, defines as:

$$\nu = -\frac{\epsilon_{lateral}}{\epsilon_{axial}}, \tag{6}$$

where ϵ_axial is the axial strain and $\epsilon_lateral$ the strain perpendicular to the applied load:

$$\text{M1:} \qquad \frac{\mathcal{Z}_n}{\mathcal{Z}_t} = 1 - \frac{\nu}{2}, \tag{7}$$

$$\text{M2:} \qquad \frac{\mathcal{Z}_n}{\mathcal{Z}_t} = \frac{1-\nu}{1-\frac{\nu}{2}}. \tag{8}$$

Therefore $\mathcal{Z}_t$ for both aforementioned models is defined as:

$$\text{M1:} \qquad \mathcal{Z}_t = \mathcal{Z}_n \frac{2}{2-\nu}, \tag{9}$$

$$\text{M2:} \qquad \mathcal{Z}_t = \mathcal{Z}_n \frac{(2-\nu)}{2(1-\nu)}. \tag{10}$$

3.4 Ultrasonic-pulse transmission

Ultrasonic pulse transmission is a technique used to study the propagation of ultrasonic waves across a medium. In this technique, a pulse is generated by a transducer and directed into the material. The waves travel through the material and are detected by another transducer on the opposite side. Hence by analyzing the time it takes for the wave to travel through the material and the amplitude of the transmitted or received signal, it is possible to investigate the effect of fluid-filled fractures on seismic waves. Ultrasonic pulse transmission is commonly used because is a non-destructive testing method.

The aluminum specimens are placed between the steel platens as is shown in figures 5 and 7b and subjected to ultrasonic pulse transmission tests. These tests were conducted at pressures up to 50 MPa, with signals recorded at 10 MPa intervals. After comparing the recorded signals, 20 MPa was selected for further analysis because it provided optimal results, allowing for an adequate amount of liquid in the fracture. The average fracture aperture is approximately 20μm under zero applied pressure, corresponding to the roughness average of a polish aluminum disc and measured using the *Keyence* VR 5000 optical profilometer (Figure 11). Figure 12 illustrates the changes in amplitude and travel times for P-waves in the intact, 1-fracture and 10 fractures dry cases. For the intact case, changes in amplitude with pressure are almost imperceptible, while for the fractured cases, amplitude changes beyond 30MPa became very small. The 20 MPa pressure ensures efficient wave propagation and high signal-to-noise ratios, making it ideal for analyzing the effect of fluid properties on wave behavior, which is the primary focus of this study.

For propagation parallel to the fracture surface normal or to the symmetry axis there are a pure vertically propagating P-wave and one vertically pure S-wave. Since the propagation is parallel to the axis of symmetry of our media, both phase and group velocity will be the same (Hornby, 1998).

To reduce the noise-to-signal ratio, 16 digitized signals were stacked for each test. The waves were recorded at a sampling rate of 40 MHz, ensuring high-resolution data acquisition with 16-bit precision. The recording window spanned 100 μs.

The sources of the waves correspond to transducers placed inside the platens: one located in the center for the P-wave and four surrounding it for the S-wave. The P-wave is employed to measure the normal dynamic compliance, whereas the S-wave is utilized for determining the tangential dynamic compliance.

Prior to the acquisition of the P- and S-waves, I determined the delay time of the ultrasonic system, including the piezoelectric transducers, performing a face-to-face test in which the platens were positioned in such a way that their surfaces are directly facing each other (without a specimen between them). The time delay for P- and S- waves are 13.15 μs and 23.78 μs, respectively.

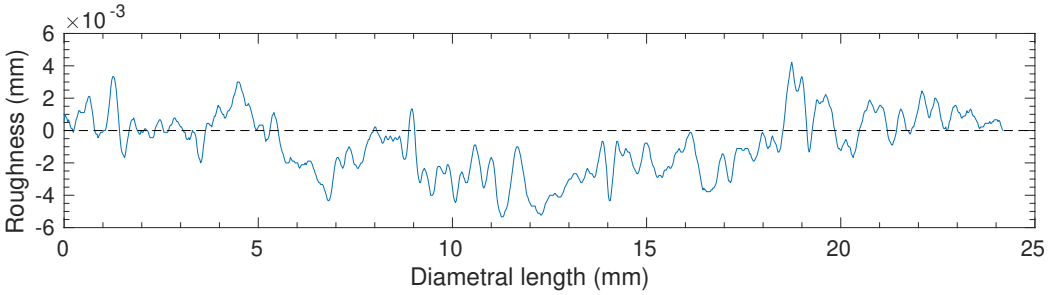

Figure 11. Surface roughness of an aluminum specimen used in this study.

3.4.1 Estimation of dynamic fracture compliance

The estimation of normal and tangential dynamic compliances involves the use of the elastic wave measurements obtained from the ultrasonic transmission laboratory tests. These values are derived by correlating the transmission coefficients of compressional and shear waves, incident normally on the fractures.

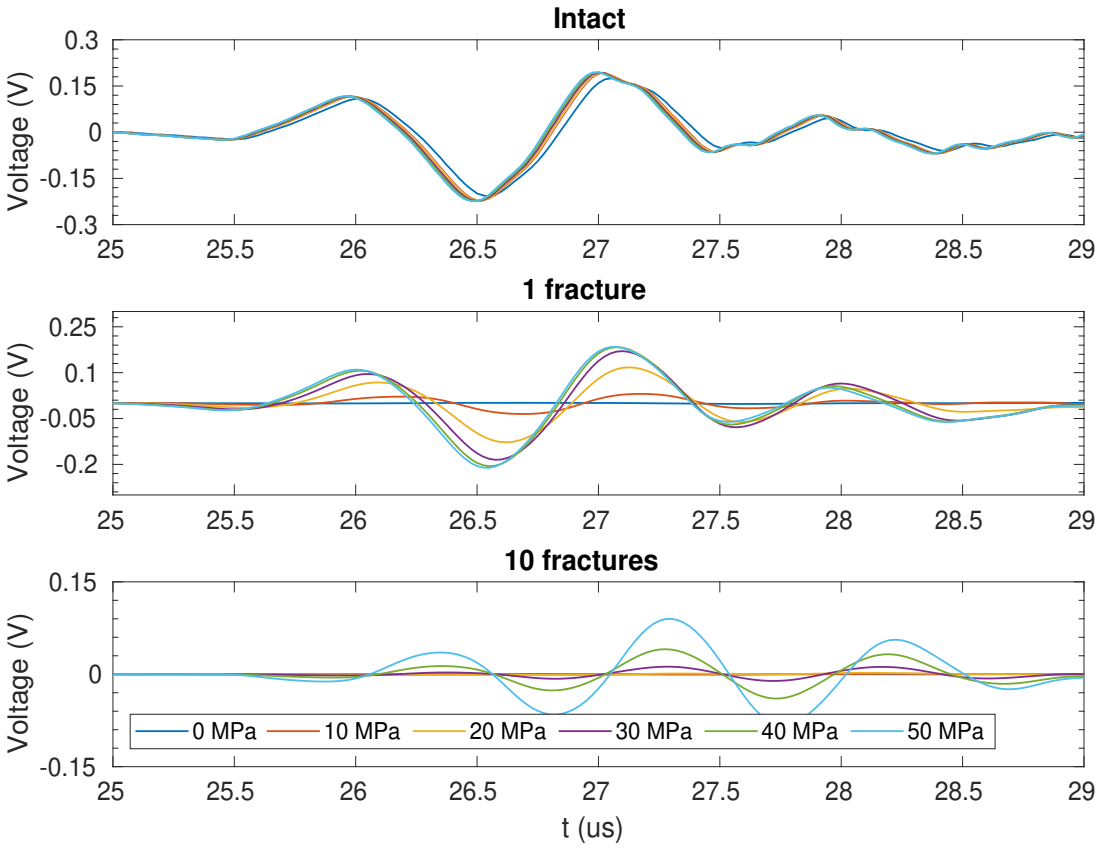

Figure 12. P-waveforms for the intact, 1-fracture, and 10-fractures under dry conditions, recorded at 10 MPa intervals, up to a maximum pressure of 50 MPa.

From LSM (Schoenberg, 1980) (see 2.4.1), analytical expressions for the compliance-dependent transmission coefficient are derived (see also Pyrak-Nolte et al., 1990b; Möllhoff et al., 2010). For a single fracture, the norm of the PP and SS transmission coefficients are given by

$$|T_{PP}^{1}| = \frac{2}{\sqrt{4 + (Z_n \zeta_P \omega)^2}}, \tag{11}$$

$$|T_{SS}^{1}| = \frac{2}{\sqrt{4 + (Z_t \zeta_S \omega)^2}}, \tag{12}$$

where $|T_{PP}^{1}|$ and $|T_{SS}^{1}|$ represent the absolute value of the transmission coefficients, determined as the ratio between waveform peak amplitudes in the time domain. Z_n and Z_t are the dynamic normal and tangential compliances, ζ_P and ζ_S denote the P- and S-wave impedance, and $\omega = 2\pi f$ is the angular frequency. For the case of N parallel fractures, Pyrak-Nolte et al. (1990a) proposed a simplified method to determine the transmission coefficient across parallel fractures by ignoring multiple reflections. Hence,

the overall transmission coefficients are expressed by the relations,

$$|T_{PP}^{N}| = |T_{PP}^{1}|^{N}, \tag{13}$$

$$|T_{SS}^{N}| = |T_{SS}^{1}|^{N}. \tag{14}$$

3.5 Ultrasonic measurements

3.5.1 Velocity

For the wave analysis, the waveforms of the intact specimen were used as a reference to compare with the waveforms through fractured specimens. The wave velocities were calculated from the P- and S-wave arrival times of transmitted ultrasonic pulses and the height of the specimens as:

$$V = \frac{H}{t_s - t_o}, \tag{15}$$

where H is the specimen length, t_s is the travel time through the specimen, and t_o is the reference travel time from the face-to-face test.

The arrival times were manually picked from the recorded waveforms or seismograms and corrected by subtracting the delay time of the system. The velocity uncertainty was estimated according to Hornby (1998), considering a specimen length of 76.08 mm with a precision of 0.005 mm. I estimated an absolute error of velocity measurement of 11.28 $\pm m/s$ and 2.78 $\pm m/s$ for a P- and S- wave propagation respectively. Therefore the relative error in the velocity estimation for the intact specimen is approximately 0.42$\%$ for P-wave velocity of 6432 m/s and 0.21$\%$ for S-wave velocity of 3139 m/s.

Error Analysis: Velocity measurements

Considering that velocities are estimated by using travel times of transmitted ultrasonic pulses (eq. 15), expressing the uncertainty in terms of partial derivatives gives us an expression that can be used for the error analysis,

$$\Delta V = \frac{\partial V}{\partial H}\Delta H + \frac{\partial V}{\partial t_s}\Delta t_s + \frac{\partial V}{\partial t_o}\Delta t_o \tag{16}$$

where Δt_s and Δt_o are the errors in the travel time picks for the measured and reference travel times and ΔH is the magnitude of the error in the specimen length measurement. By substituting the explicitly

expression for velocity and simplifying the partial derivatives in eq. 16, it is obtained:

$$\Delta V = \frac{\Delta H}{t_s - t_o} + H \left| \frac{\Delta t_s}{(t_s - t_o)^2} \right| + H \left| \frac{\Delta t_o}{(t_s - t_o)^2} \right| \tag{17}$$

Assuming symmetric uncertainty in the time picks (i.e., $\Delta t = |\Delta t_s| = |\Delta t_o|$), eq. 17 can be simplified to compute the maximum absolute error in velocity:

$$\Delta V = \frac{\Delta H}{t_s - t_o} + 2H \frac{\Delta t}{(t_s - t_o)^2} \tag{18}$$

Eq. 18 is the final form used to estimate the maximum velocity uncertainty in this study.

3.5.2 Transmission Coefficient

In assessing wave transmission through fractured media, the wave transmitted through an intact specimen serves as the reference incident pulse. This approach minimizes the impact of the interfaces between the intact specimen and transducers on wave propagation. Wave transmission is typically quantified using the transmission coefficient, which is the ratio of the amplitudes of the transmitted and incident waves. In the context of this study, the transmission coefficient is determined using the peak-to-peak amplitude of the first arriving pulses (Möllhoff et al., 2010; Yang et al., 2020). This parameter is useful as it describes the amplitude of the transmitted wave across a fractured specimen relative to the intact specimen, providing information about seismic propagation and wave behavior in different fluid-filled fractured specimens

$$T = \frac{A_{ft}}{A_{it}}. \tag{19}$$

where A_{ft} and A_{it} are the peak-to-peak wave amplitudes of the pulse transmitted through the fractured and intact specimens, respectively.

3.5.3 Quality factor Q

The quality factor, Q, is a measure of how dissipative the material is, i.e., it quantifies how effectively a material attenuates seismic waves and is a dimensionless quantity. A lower Q indicates greater dissipation, and vice versa. In this study, the Spectral Ratio Method was used to estimate the quality factor Q. This

method analyzes waveforms in the frequency domain. I followed the procedure outlined in Toksöz et al. (1979), and Pyrak-Nolte et al. (1990b), see also Yang et al. (2020); Zhou et al. (2020).

The Spectral Ratio Method was applied specifically to the first arrival pulse, which was isolated from the initial portion of the transmitted P- and S-waveforms. This initial portion includes the first arrival pulse and subsequent reflections from various interfaces within the medium. To isolate the first arrival pulse for the analysis, a cosine taper with a window width between 3.5 and 4.4 μs was applied. This tapering process ensures that the selected time window minimizes any signal spectrum distortion.

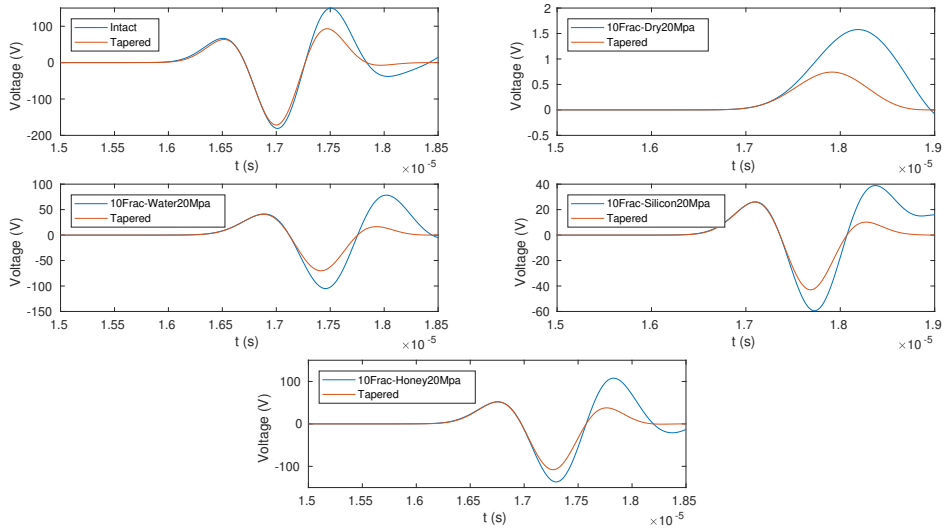

(a) P-wave Tapered

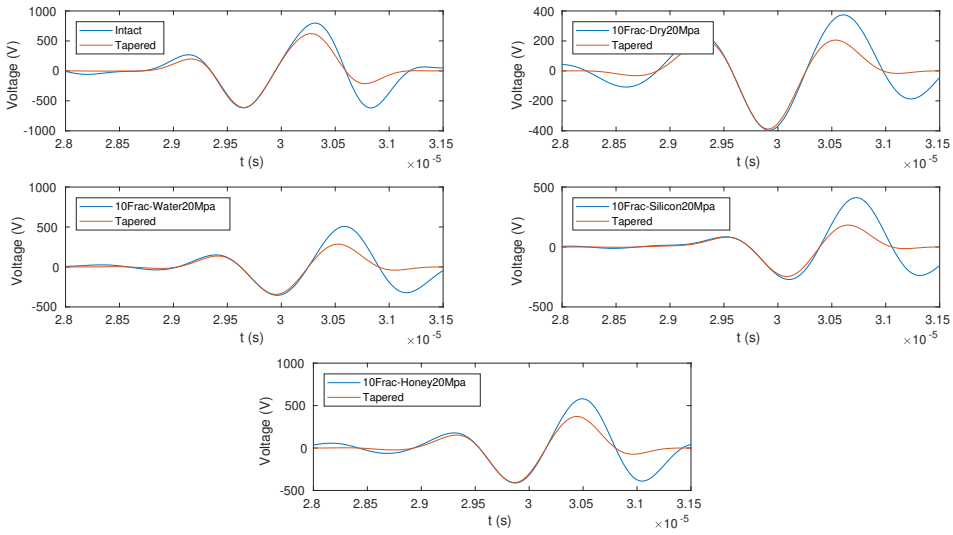

(b) S-wave Tapered

Figure 13. Selected initial arrival wave (raw waveform) and tapered waves for a 10-fractured specimen for different fluid. Waves were tapered by a cosine.

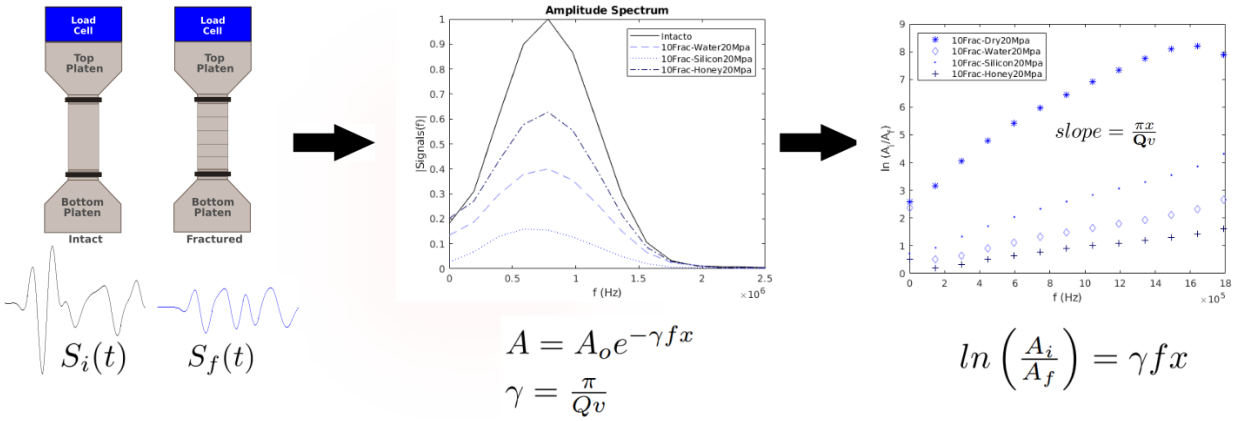

Figure 14. Summary of Spectral Ratio method used for Q-estimation.

Figures 13a and 13b show the original initial waves and tapered waves selected by cosine taper for 10-fracture specimens for the different fluids used in this study. With the signals tapered the next step is to determine the amplitude spectra by the Fast Fourier Transform (FFT). This spectral information is used to quantify the wave attenuation through the quality factor Q by using the spectral ratio method (Toksöz et al., 1979). This method has been widely use in the literature (e.g. Pyrak-Nolte et al., 1990b; Yang et al., 2019) and measure the attenuation relative to a reference sample which has very low attenuation (aluminum intact-specimen). The expressions for the plane seismic wavefields, for the reference (intact) and fractured specimens are given as:

$$A_i(f) = A_{oi}(x)e^{-\alpha_i x}e^{i(\omega t - k_i x)} \tag{20}$$

and

$$A_f(f) = A_{of}(x)e^{-\alpha_f x}e^{i(\omega t - k_f x)}, \tag{21}$$

where x is the travel path length, f is the frequency, A_{oi} and A_{of} are geometrical factors, k is the wavenumber, and α is the frequency-dependent attenuation coefficient. The subscripts i and f refer to the intact and fractured specimens, respectively. It is assumed that α is a linear function of frequency, thus one can write it as:

$$\alpha(f) = \gamma f, \tag{22}$$

where γ is a constant related with Q by

$$Q = \frac{\pi}{\gamma \nu}. \tag{23}$$

Therefore the ratio of the Fourier amplitudes is:

$$ln\frac{A_i}{A_f} = \gamma_f fx + ln\frac{A_{oi}}{A_{of}}, \tag{24}$$

When $\frac{A_{oi}}{A_{of}}$ is independent of frequency, and assuming the same geometry for both the intact and fractured specimens, then $A_{oi} = A_{of}$, and Q, the quality factor can be determined by:

$$ln\frac{A_i}{A_f} = \gamma_f fx \tag{25}$$

$$ln\frac{A_i}{A_f} = \frac{\pi}{Q\nu} fx, \tag{26}$$

γ_f is determined from the slope of the line fitted to $ln(A_{oi}/A_{of})$ versus frequency (Figure 14).

Chapter 4. Numerical Modeling

In the context of seismic wave propagation, the Discontinuous Galerkin Method (DGM) is particularly valuable because it allows for the use of discontinuous functions at element boundaries, enabling the analysis of displacement fields within media containing faults and fractures (De Basabe et al., 2016). This method has been widely used to approximate the elastodynamic equation in seismic studies. In this thesis, numerical simulation of ultrasonic wave propagation in both intact and fractured specimens were conducted using DGM to complement findings from laboratory experiments.

This chapter provides an overview of DGM, then introduce the weak formulation used in DGM for the wave equation, specifically the interior Penalty (IP-DGM) form and finally provide a summary of the parameters used in the numerical simulations.

4.1 Discontinous Galerkin method

DGM is a class of finite element methods for solving partial differential equations by approximating solutions with discontinuous, piecewise polynomials as basis functions, unlike typical finite element methods. The original problem is decomposed into a set of subproblems, each associated with a disjoint finite element mesh, where each mesh element determines a single subproblem, and appropriate conditions connect these subproblems (see Figure 15). The global solution over the entire computational domain is then obtained by summing the contribution from all mesh elements, enabling DGM to effectively handle sharp gradients, discontinuities, and complex boundary conditions (Lähivaara, 2010).

This method was first introduced in 1973 to solve the hyperbolic neutron transport equation (Reed & Hill, 1973), in the late eighties, Cockburn et al. (2000) connected the discontinuous Galerkin method with high-order Runge-Kutta-type time integration schemes. DGM were later extended to other fields of physics and engineering such us meteorology, modeling of shallow water, electromagnetism, gas dynamics, among many others, and its popularity increased since the early 1990s.

Initially, the general strategy for solving hyperbolic differential equations using the first-order form with DGM involved discretizing the differential equation in space using a flux-based formulation and in time using Runge-Kutta methods (De Basabe, 2011). In the field of seismic wave propagation, the first application was published by Käser & Dumbser (2006).

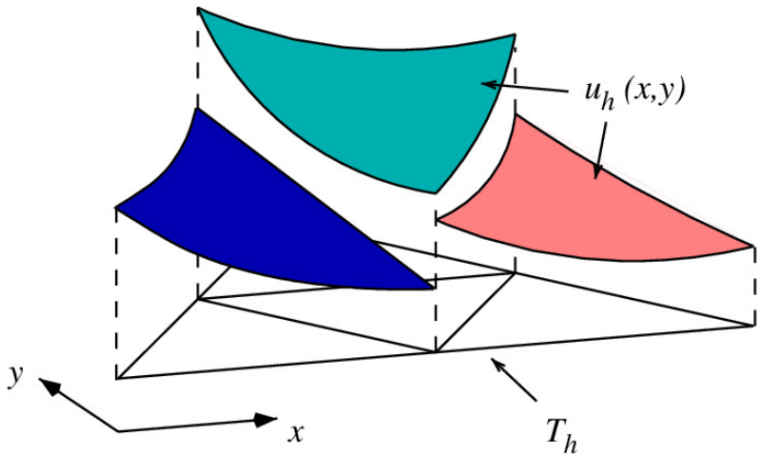

Figure 15. Discontinous elements with interface solution u_h for the element T_h in a nonoverlaping system (mosaic) of the domain Ω. Modified from Fidkowski & Chen (2020).

Also around the 1970s, independently, the Galerkin method was applied to elliptic and parabolic equations using discontinuous finite elements. These approaches were generally known as *interior penalty* IP methods, and their development remained independent from the DG methods for hyperbolic equations. The IP methods arose from the observation that, just as Dirichlet boundary conditions could be imposed weakly instead of being built into the finite element space, so interelement continuity could be attained in a similar fashion. This makes it possible to use spaces of discontinuous piecewise polynomials for solving second order problems (Arnold et al., 2000).

Some discontinuous Galerkin methods proposed for wave propagation include: Incomplete Interior Penalty (IIPG) (Dawson et al., 2004), the Non-symmetric Interior Penalty Galerkin (NIPG) (Rivière et al., 1999), and the Symmetric Interior Penalty Galerkin (SIPG) (Wheeler, 1978; Arnold, 1982).

Within this framework, incorporating fractures is straightforward, as the degrees of freedom of each element in the model are independent. DGM allow to simulate the presence of single fractures in a natural way, instead of using effective medium theories. De Basabe et al. (2016) proposed a scheme that incorporates fractures using Schoenberg's LSM (Schoenberg, 1980) within IP-DGM for wave propagation.

The method utilizes discontinuous basis functions and an additional penalty term in the weak formulation to enforce continuity where required (Rivière, 2008). It has been successfully applied to elastic wave propagation. Its advantages include (a) the ability to handle unstructured meshes, (b) ease of parallelization on high-performance computers, (c) the capability to model large volumes of fractures with a high degree of precision, (d) versatility in incorporating various types of boundary conditions such

as Dirichlet, Neumann, or Robin, (e) the ability to include arbitrary topography and heterogeneities using irregular grids (De Basabe et al., 2016).

4.1.1 Weak Formulation of the Elastic Wave Equation : Non-fractured media

Elastic wave equation

An elastic wave arises when particles within a medium are displaced due to a mechanical perturbation and it is mathematically represented by the momentum equation for an elastic continuum:

$$\rho\, \ddot{\boldsymbol{\mathcal{U}}} = \boldsymbol{\nabla} \cdot \boldsymbol{\sigma} + \boldsymbol{f}, \tag{27}$$

where $\boldsymbol{\mathcal{U}} = \boldsymbol{\mathcal{U}}(\boldsymbol{x}, t)$ is the displacement field, $\ddot{\boldsymbol{\mathcal{U}}} = \partial^2 \boldsymbol{\mathcal{U}} / \partial t^2$ is the acceleration, $\rho = \rho(\boldsymbol{x})$ denotes the density, $\boldsymbol{\sigma} = \boldsymbol{\sigma}(\boldsymbol{x}, t)$ is the stress tensor, and $\boldsymbol{f}(\boldsymbol{x}, t)$ represents the source vector. We require a relationship between stress and strain, which is given by Hooke's law:

$$\boldsymbol{\sigma} = \boldsymbol{C} \,:\, \boldsymbol{\epsilon}, \tag{28}$$

where $\boldsymbol{C}$ is the fourth-order stiffness tensor or the elasticity tensor, the operator : denotes the double-dot product, and $\boldsymbol{\epsilon}$ is the strain tensor, defined in terms of the displacement by:

$$\boldsymbol{\epsilon} = \frac{1}{2} \left(\nabla \boldsymbol{\mathcal{U}} + \nabla \boldsymbol{\mathcal{U}}^T \right). \tag{29}$$

For linear, isotropic media, the stress-strain relationship, equation 28, takes the form:

$$\sigma_{ij}(\boldsymbol{\mathcal{U}}) = \lambda \delta_{ij} \partial_k \mathcal{U}_k + \mu (\partial_i \mathcal{U}_j + \partial_j \mathcal{U}_i), \tag{30}$$

where $\lambda = \lambda(\boldsymbol{x})$ and $\mu = \mu(\boldsymbol{x})$ are the Lamé parameters, and δ_{ij} is Kronecker's delta. Substituting equation 30 into equation 27 yields the elastic wave equation for an isotropic and elastic domain in

vector notation:

$$\begin{aligned} \rho\ddot{\boldsymbol{\mathcal{U}}} - \nabla\lambda(\nabla\cdot\boldsymbol{\mathcal{U}}) - \nabla\mu(\nabla\boldsymbol{\mathcal{U}} + \nabla\boldsymbol{\mathcal{U}}^T) = \boldsymbol{f} \quad &\text{in } \Omega\times(0,T] \\ \boldsymbol{\tau}(\boldsymbol{\mathcal{U}}) = 0 \quad &\text{on } \partial\Omega \\ \boldsymbol{\mathcal{U}} = \dot{\boldsymbol{\mathcal{U}}} = 0 \quad &\text{for } t = 0, \end{aligned} \tag{31}$$

where $\Omega \subset \mathbb{R}^d$ is the physical domain, d is the number of physical dimensions (2 or 3), $\boldsymbol{\tau}(\boldsymbol{\mathcal{U}}) = \boldsymbol{\sigma}(\boldsymbol{\mathcal{U}})\cdot\boldsymbol{n}$ is the traction vector, $\partial\Omega$ is the external boundary of Ω, $\boldsymbol{n}$ is a unitary vector normal to $\partial\Omega$, and $(0,T]$ is the time domain.

To derive the weak formulation, the wave equation 31 is discretized by partitioning the computational domain into smaller elements. To proceed with the formulation, let me introduce the necessary notation and mathematical framework (see figure 16), following De Basabe et al. (2008, 2016), which will be used to construct the weak form of the wave equation.

- Ω_h: Finite element partition of the domain Ω.
- Γ_h: The set of all faces between the elements in Ω_h.
- $\Gamma_c \subset \Gamma_h$: The subset of all faces where the displacement field is continuous.
- $\Gamma_f \subset \Gamma_h$: The subset of faces representing fractures, where $\Gamma_c \cup \Gamma_f = \Gamma_h$ and $\Gamma_c \cap \Gamma_f = \emptyset$.
- $\{.\}$ denotes the average of the function on $\gamma \in \Gamma_h$.
- $[.]$ denotes the jump of the function on $\gamma \in \Gamma_h$.
- γ is the edge between elements E_1 and E_2.

  Therefore, the average and jump of a scalar function u over γ are given by:

$$\{u\} = \frac{1}{2}\left(u\mid_{E_1} + u\mid_{E_2}\right) \text{ and } [u] = u\mid_{E_1} - u\mid_{E_2}. \tag{32}$$

A vector space $\mathbf{X} = X^d$, is introduced, where $X = span\{\phi_i\}_{i=1}^N$, ϕ_i are the discontinuous basis functions and N is the total number of these functions.

The first step in solving for $\boldsymbol{u} \in \mathbf{X}$ is to multiply equation 31 by a vector test function $\boldsymbol{v} \in \mathbf{X}$, and perform an element-wise integration to obtain

$$\partial_{tt}\int_E \rho\boldsymbol{u}\cdot\boldsymbol{v}d\boldsymbol{x} - \int_E (\nabla\lambda(\nabla\cdot\boldsymbol{u})\cdot\boldsymbol{v} - \nabla\mu(\nabla\boldsymbol{u} + \nabla\boldsymbol{u}^T)\cdot\boldsymbol{v})d\boldsymbol{x} = \int_E \boldsymbol{f}\cdot\boldsymbol{v}d\boldsymbol{x}. \tag{33}$$

Using the corollary of the Gauss divergence theorem:

$$\int_{\Omega} \varphi \nabla \cdot \boldsymbol{u} = \int_{\partial\Omega} \varphi \boldsymbol{u} \cdot \boldsymbol{n} - \int_{\Omega} \nabla\varphi \cdot \boldsymbol{u}, \tag{34}$$

It is applied to equation 33 to get the corresponding equation with boundary terms

$$\begin{aligned} \partial_{tt} \int_E \rho \boldsymbol{u} \cdot \boldsymbol{v}\, d\boldsymbol{x} + \int_E \left(\lambda(\nabla\cdot\boldsymbol{u})(\nabla\cdot\boldsymbol{v}) + \mu(\nabla\boldsymbol{u} + \nabla\boldsymbol{u}^T) : \nabla\boldsymbol{v}\right) d\boldsymbol{x} \\ - \int_\gamma \left(\lambda(\nabla\cdot\boldsymbol{u})\boldsymbol{v} + \mu\boldsymbol{v}(\nabla\boldsymbol{u} + \nabla\boldsymbol{u}^T)\right)\cdot\boldsymbol{n}\, d\gamma \\ = \int_E \boldsymbol{f}\cdot\boldsymbol{v}\, d\boldsymbol{x}. \end{aligned} \tag{35}$$

The second step involves handling the boundary integral over γ. This integral is not well defined due to the discontinuity of $\boldsymbol{u}$ across element interfaces. To address this, it is applied the property $[\xi\psi] = \{\xi\}[\psi] + [\xi]\{\psi\}$ for $\gamma \in \Gamma_c$, which yields to the following expression, representing the contribution of the integral over the interface between adjacent elements. Due to the physical requirement of traction continuity across element interfaces, the jumps in the traction vector must be zero, therefore:

$$\begin{aligned} \boldsymbol{J}^c_\gamma(\boldsymbol{u},\boldsymbol{v}) = \int_\gamma \{\boldsymbol{\tau}^\gamma(\boldsymbol{u})\}\cdot[\boldsymbol{v}] d\gamma - \int_\gamma \{\boldsymbol{\tau}^\gamma(\boldsymbol{v})\}\cdot[\boldsymbol{u}] d\gamma \\ + \frac{R}{|\gamma|}\int_\gamma \{\lambda + 2\mu\}[\boldsymbol{u}]\cdot[\boldsymbol{v}]\, d\gamma. \end{aligned} \tag{36}$$

Where, R and S are the penalty and symmetry parameters respectively, added without loss of generality and for stability. S takes values of 0, 1, or -1 depending on the specific formulation of IP-DGM (S=0 for IIPG, S=-1 for SIPG, and S=1 for NIPG). The formulation used by De Basabe et al. (2016) is SIPG (S=1).

Hence, the weak formulation for the wave equation is:

$$\sum_{E\in\Omega_h} \left((\rho\partial_{tt}\boldsymbol{u},\boldsymbol{v})_E + \boldsymbol{B}_E(\boldsymbol{u},\boldsymbol{v}) \right) + \sum_{\gamma\in\Gamma_c} \boldsymbol{J}^c_\gamma(\boldsymbol{u},\boldsymbol{v}) = \sum_{E\in\Omega_h} (\boldsymbol{f},\boldsymbol{v})_E, \quad \forall\, \boldsymbol{v}\in\mathbf{X} \tag{37}$$

where

$$(\boldsymbol{u},\boldsymbol{v})_E = \int_E \boldsymbol{u}\cdot\boldsymbol{v}\, d\boldsymbol{x}, \tag{38}$$

$$\boldsymbol{B}_E(\boldsymbol{u},\boldsymbol{v}) = \int_E \left(\lambda(\nabla\cdot\boldsymbol{u})(\nabla\cdot\boldsymbol{v}) + \mu(\nabla\boldsymbol{u} + \nabla\boldsymbol{u}^T) : \nabla\boldsymbol{v}\right) d\boldsymbol{x}. \tag{39}$$

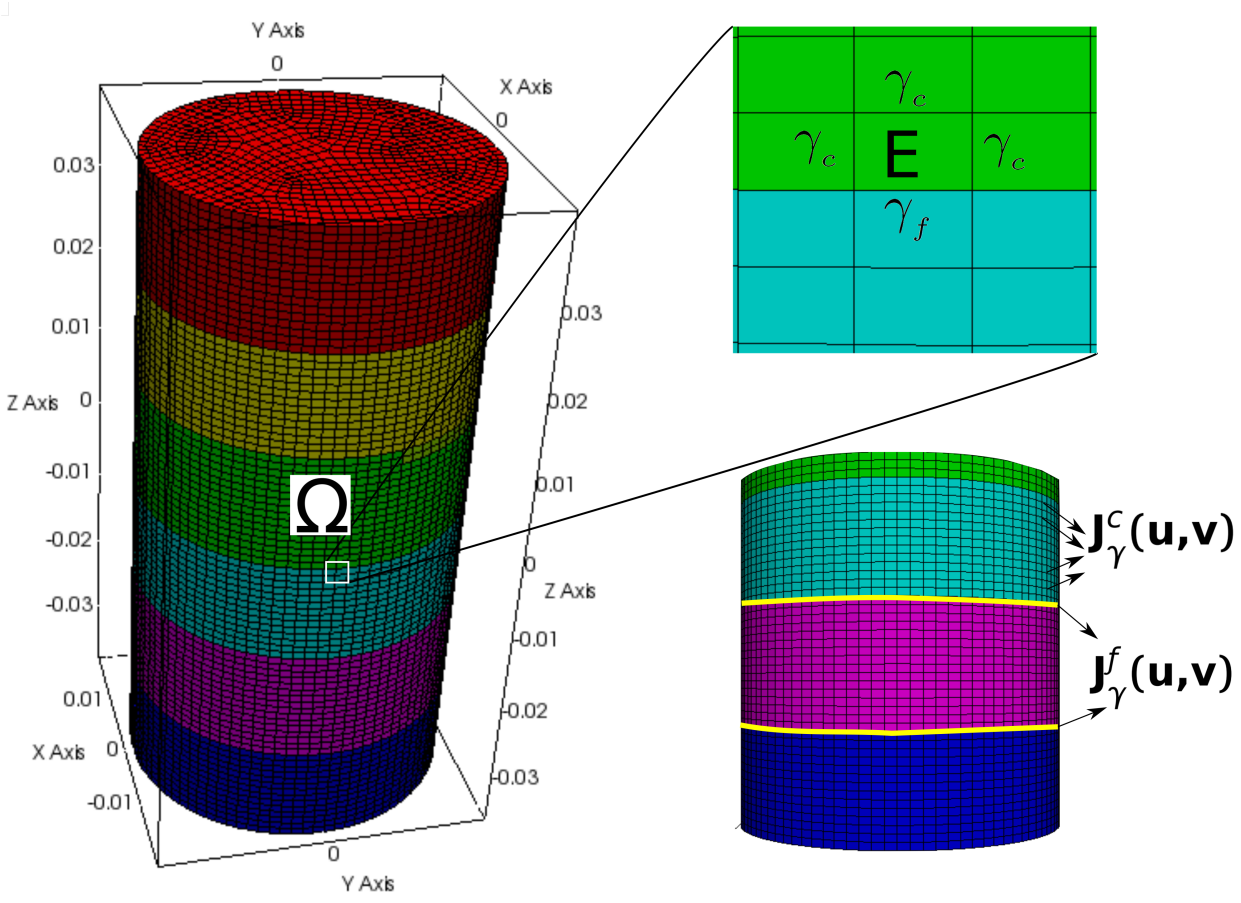

Figure 16. A depiction of a domain Ω consisting of 6 discs, each represented by a different color. An element E shares edges with other elements within the same disc and with elements from neighboring disc. γ_c denotes the edge where the displacement field is continuous, while γ_f represents the edge where the displacement field is discontinuous (indicating a fracture). $\mathbf{J}^c_\gamma(\mathbf{u},\mathbf{v})$ refers to the penalty term associated with continuous edges, and $\mathbf{J}^f_\gamma(\mathbf{u},\mathbf{v})$ represent the term for the linear slip condition at a fracture edges (yellow line).

4.1.2 Weak formulation : fractured media of the Elastic Wave Equation

Within the framework of the weak formulation, some interfaces between elements can be selectively treated as discontinuous, allowing fractures to be naturally incorporated into the model without altering the mesh structure. This approach accommodates natural discontinuities or jumps in the medium and wavefield, which commonly occur around fractures. To account for the presence of fractures, the term $\boldsymbol{J}^f_\gamma(\boldsymbol{u},\boldsymbol{v})$ is introduced in the weak formulation of the wave equation Eq. (37). At the fracture interfaces, i.e, for $\gamma \in \Gamma_f$, the symmetry and penalty terms are ommited, as the displacement field is discontinuous.

In this case, the fracture contribution is:

$$\boldsymbol{J}_{\gamma}^{f}(\boldsymbol{u},\boldsymbol{v}) = \int_{\gamma} \{\boldsymbol{\tau}^{\gamma}(\boldsymbol{u})\} \cdot [\boldsymbol{v}] d\gamma. \tag{40}$$

Substituting the expression of the traction average in this equation with equation 3, yields

$$\boldsymbol{J}_{\gamma}^{f}(\boldsymbol{u},\boldsymbol{v}) = \int_{\gamma} \boldsymbol{Z}^{-1}[\boldsymbol{u}] \cdot [\boldsymbol{v}]\, d\gamma. \tag{41}$$

Therefore the weak formulation including fracture is:

$$\sum_{E\in\Omega_h} \left((\rho\partial_{tt}\boldsymbol{u},\boldsymbol{v})_E + \boldsymbol{B}_E(\boldsymbol{u},\boldsymbol{v}) \right) + \sum_{\gamma\in\Gamma_c} \boldsymbol{J}_{\gamma}^{c}(\boldsymbol{u},\boldsymbol{v}) + \sum_{\gamma\in\Gamma_f} \boldsymbol{J}_{\gamma}^{f}(\boldsymbol{u},\boldsymbol{v}) = \sum_{E\in\Omega_h} (\boldsymbol{f},\boldsymbol{v})_E, \quad \forall\, \boldsymbol{v}\in\mathbf{X}. \tag{42}$$

4.2 Numerical models

The numerical simulations were computed using a code that implements IP-DGM to solve seismic wave propagation, explicitly including fractures under the LSM scheme. The code developed by De Basabe (2009) is written in C++ and incorporates various methods for spatial and temporal discretization of the acoustic or elastic wave equation in 2D and 3D. Among these methods, IP-DGM is available in different versions: acoustic, elastic, acoustic-elastic, fractured, anisotropic and anisotropic-fractured. Each version utilizes the Finite Difference method (FDM), the 4th-order Runge-Kutta method (RK-4), and the 4th-order Lax-Wendroff method (LWM-4) for time stepping. This method was validated and tested by De Basabe et al. (2016), who used it to generate synthetic seismograms for a set of horizontal fractures to simulate the reflection and transmission of waves at fracture and at fracture interface waves. The approach also enables exploration of anisotropic effects of fractures on propagating elastic waves (Vasilyeva et al., 2019; Vamaraju et al., 2020; Rioyos-Romero et al., 2022). More recently, it has been applied to investigate elastic wave propagation through cylinders with fluid-filled fractures using IP-DGM, as presented in Ramos-Barreto et al. (2025).

The code is structured to allow flexibility in adjusting parameters, making it adaptable for various test scenarios. Therefore, the experimental setup used in the laboratory has been replicated. To model the conditions of the laboratory experiments, I examine the three-dimensional elastic wave equation. In this section, I provide an overview of the input parameters, which are categorized into three main groups:

(a) model parameters, (b) background parameters, and (c) fracture parameters.

a. Model parameters

Model parameters are those involved in the simulations, including the physical model, physical dimensions, numerical method, polynomial degree of the basis functions for the numerical method and mesh type. For the Discontinuous Galerkin method, additional parameters are specified, such as method type, penalty, basis type, time stepping, maximum time and the stability condition for time stepping CFL (Courant-Fiederich-Lewy), condition for convergence. The specific parameters used in the simulations are as follow:

- PHYSICAL MODEL : FRACTURED
- DIMENSIONS : 3
- METHOD : DG (DISCONTINUOUS GALERKIN)
- POLY. ORDEN : 3
- MESHFILE : Exodus II mesh file

The structured 3D cylindral mesh used in the numerical simulations was generated with Cubit Version 13.1, by Sandia National Laboratories[1] (Figure 17). The mesh consist of 807,030 hexahedral elements, designed to ensure that the interfaces between the elements closely align with the height of the aluminum disc, explicitly incorporating fractures in the simulations. Although the mesh is cylindrical, the simulations are conducted in a Cartesian coordinate system (x,y,z). The element's size are chosen to avoid numerical dispersion, ensuring sampling ratios of at least 5 nodes per wavelength for S-waves and at least 11 nodes per wavelength for P-waves. The remaining parameters in this group are:

DG parameters

- DGTYPE : SIPG
- DGPENALTY : 50
- BASISTYPE : NODAL-GLL (Gauss-Lobatto-Legendre)

Time Stepping parameters

- TSMETHOD : 2nd order Finite Difference

[1] `https://cubit.sandia.gov/`

- TMAX : 50 μs
- CFL : 0.01

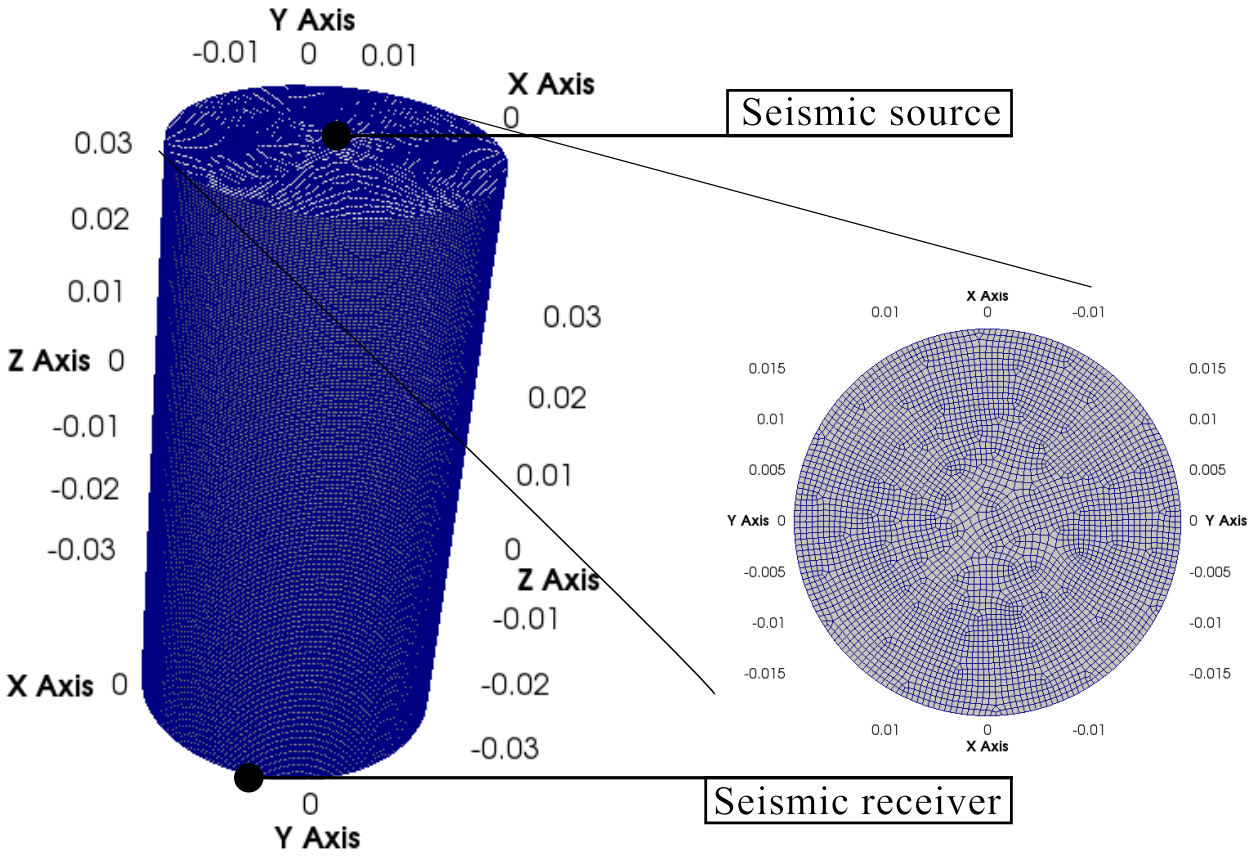

Figure 17. Finite-element mesh created with Cubit for the simulations. A wave, generated from a source positioned at the top of the cylinder, propagates through the model and is recorded by the receiver at the bottom.

b. Background parameters

To best mimic the laboratory experimental conditions, the seismic source is modeled as a vector point source centered at the top of the model. The receiver (where the seismogram is recorded) centered at the bottom of the model (see Figure 17). This source generates a directional impulse producing a 1 MHz pulse: a downward impulse in the z-direction for P-wave and in the x-direction for S-wave. The time function of the source is a Ricker wavelet, which is similar to the second derivative of the Gaussian function.

The code produces three types of outputs: snapshots, seismograms, and traces. Snapshots represent the wavefield at a specific time, while seismograms are time functions that record the wave field at a

point, and traces are seismograms recorded along a set aligned points. I selected a single seismogram, specifying its location.

The surface of the physical domain, a cylinder, is left without absorbing boundaries to replicate the reflections observed in laboratory experiments. This cylindrical domain is defined by the mesh described earlier, the background matrix was modeled using the properties determined in laboratory tests of the intact aluminum specimen. These properties include a P-wave velocity of 6425 m/s, S-wave velocity of 3140 m/s, and a density of 2702 kg/m^3.

Source and receiver parameters

- SRCTYPE : Point Source
- SRCFUNC : Ricker pulse 2nd derivative
- PKFREQ : 1.0 MHz
- SRCLOC : Source location (X,Y,Z) - Top of the cylinder
- SRCVECTOR : Polarization of the wave
- NSEISMO : 1 - Number of seismograms
- SEISMO : Location of seismogram recording (X,Y,Z) -Bottom of the cylinder

Boundary conditions

- FREESURF : Free Surface
- BC : Neumman (Boundary Coditions)

Domain parameters

- VP : 6425 m/s - Background P-wave velocity
- VS : 3140 m/s - Background S-wave velocity
- RHO : 2702 kg/m^3 Background density

c. Fracture parameters

As noted throughout the document, fractures are defined by the compliance they add to the background material. These are systematically incorporated into the simulation, requiring inputs for the number of fractures, their normal and tangential compliances (estimated from P- and S-waves data obtained via

the ultrasonic pulse tests, see section 3.4.1), and their specified location by x, y and z coordinates in the code. Recall that, as I mentioned in the model parameter section, the simulations are performed in Cartesian coordinate system.

- NFRACTURES : Number of fractures (1,5 or 10)
- ZT_i : Tangential compliance for i-th fracture in m/Pa
- ZN_i : Normal compliance for i-th fracture in m/Pa
- $FRACX_i$: X coordinates of the i-th fracture
- $FRACY_i$: Y coordinates of the i-th fracture
- $FRACZ_i$: Z coordinates of the i-th fracture

Figure 18 is a simplified flowchart that illustrates the interaction between the laboratory experiments results and numerical modeling, showing how laboratory-derived seismograms and fracture key parameters (compliances) serve as inputs to numerical simulations, enabling a comparison of key wave parameters (wave velocity, transmission coefficient, and quality factor) between experimental and simulated results.

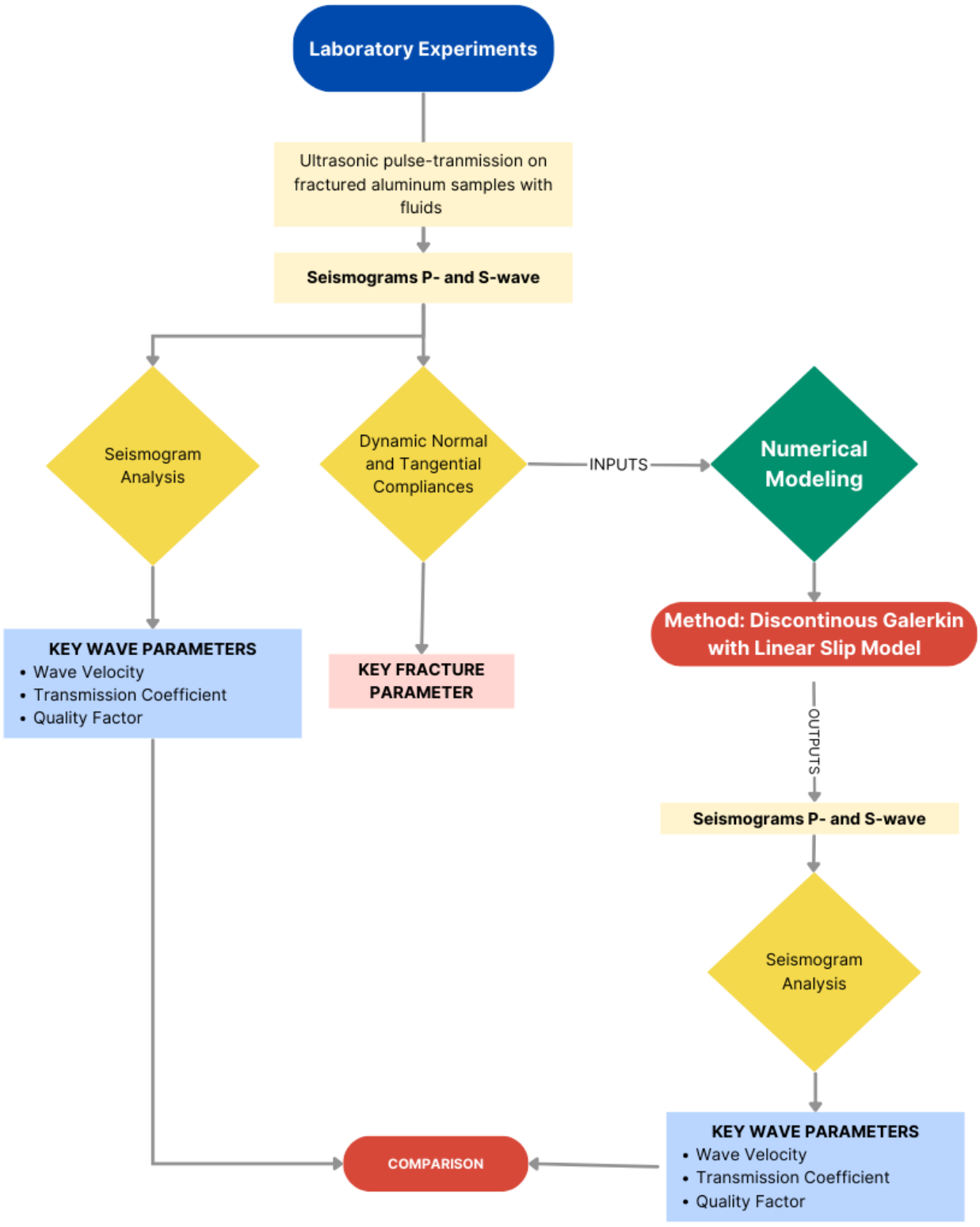

Figure 18. Simplified representation of the flow for the numerical modeling.

Chapter 5. Results

This chapter presents the results of laboratory experiments and numerical modeling aimed at understanding the effect of fluid properties, specifically viscosity and density, on wave propagation in fluid-filled fractures. Mechanical and ultrasonic tests were conducted on aluminum specimens, including one non-fractured and three fractured samples with one, five, and ten fractures, respectively. These fractures, filled with water, silicon oil and honey, were oriented perpendicular to wave propagation.

The first part of the experimental results focuses on determining fracture compliance, the critical property that characterizes fractures, it is derived from mechanical and ultrasonic tests on aluminum specimens. By analyzing how fracture compliance changes depending on the type of fluid and number of fractures, we gain insight into how fluid properties interact with fractures. The second part of the experiments shows how the fluids, along with the number of fractures, impact wave velocity, transmission coefficients, and attenuation.

Finally, these experimental findings were complemented by numerical simulations, which replicated the experimental conditions.

5.1 Experimental results

5.1.1 Fracture compliances of fracture specimens

Fracture compliance is a parameter that measures how easily a fracture deforms under stress, reflecting the mechanical response of fractures to applied forces. In this research, I determined both static and dynamic fracture compliance. The static compliance was obtained through mechanical test at a constant pressure and the dynamic compliance was derived from P- and S-waves seismograms recorded at a fixed pressure.

Interesting trends emerge when I examine the relationships between fracture compliances and fluid properties, specifically fluid density and viscosity. Figure 20 displays the normal and tangential components of the dynamic and static compliances as a function of the saturating fluid density for different numbers of fractures. This figure shows that for both normal and tangential components, the static are higher than the dynamic compliances. Figures 20a and 20c display the normal and tangential dynamic compliances. The normal dynamic compliances range from $\sim 9.32 \times 10^{-15}$ to 5.87×10^{-14} m/Pa, whereas the

tangential range from $\sim 1.27 \times 10^{-14}$ to 3.76×10^{-14} m/Pa. Notably, the normal dynamic compliance has a significant variation depending on whether the fracture is filled with air or liquids. In contrast, the tangential dynamic compliance appears to be less sensitive to the presence of fluid. Both the normal and tangential components of dynamic compliance exhibit a general decreasing trend as the fluid density and number of fractures increase.

Figures 20b and 20d show the static compliance's normal and tangential components against fluid density. The normal static compliance was determined by the slope of the tangent of the stress-displacement curves, as explained in section 3.3.1. Meanwhile, the static tangential compliances were approximated using equations 7 and 8. In comparison with the dynamic compliances, the static compliances exhibit a much narrower range of values regardless of the kind of fluid. Notice that the static compliances for the water case are higher than those for silicon oil, breaking the trend.

The trends in figures 20a and 20c show that the dynamic fracture compliance and fluid density are inversely proportional. Namely, higher fluid density yields lower values of fracture compliance. In contrast, a distinct trend is not apparent when fracture compliance is plotted against fluid viscosity; this relationship does not exhibit a clear and consistent pattern. However, the relation is more complicated in the static case because the pattern is disrupted by water as the infilling fluid.

Figure 19 shows the Z_n/Z_t ratios for the dynamic compliances. Note that the ratio of the fluid-filled fractures is below 0.6, whereas the dry cases have ratios above 1.0. The low Z_n/Z_t ratios in the fluid-filled fractures can be attributed to the low dynamic normal compliance, as shown in figure 20a.

The static and dynamic compliances determined in this study agree with previously reported data available in the literature for different rock types (Table 3), supporting the use of aluminum samples as a proxy for rocks in our study.

5.1.2 Observed waveforms

The observed waveforms obtained from the ultrasonic experiments for the intact and fractured specimens subjected to an uniaxial normal stress of 20 MPa are displayed in figures 21 and 22 respectively. The waveforms exhibit an initial direct P- and S- wave transmitted pulse, followed by reflections from the fractures and boundaries. Intact specimens (with no fractures) show the larger amplitude, while fluid-filled fractures cause a reduction in amplitude and an increase in waveform distortion.

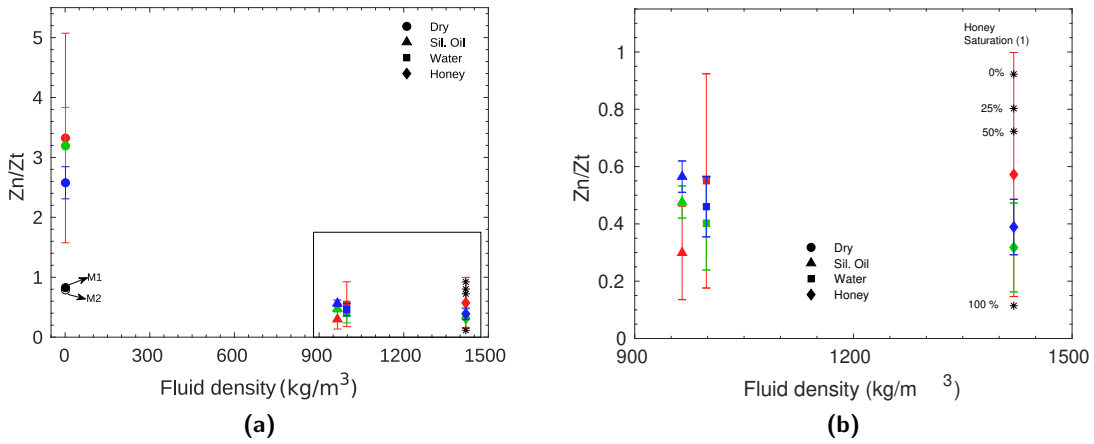

Figure 19. Measured Z_n/Z_t ratio from laboratory experiments at 20 MPa. Icons in colors red (1 fracture), green (5 fractures), and blue (10 fractures) correspond to this study, as well as the open and filled circles denoted as M1 and M2 (equations 7 and 8). The black asterisks correspond to data from Hsu & Schoenberg (1993). Error bars in the figure represent the standard deviation associated with the mean value of the Zn/Zt ratio. (a) Z_n/Z_t for all fluids, and (b) magnified view of the black rectangle from (a).

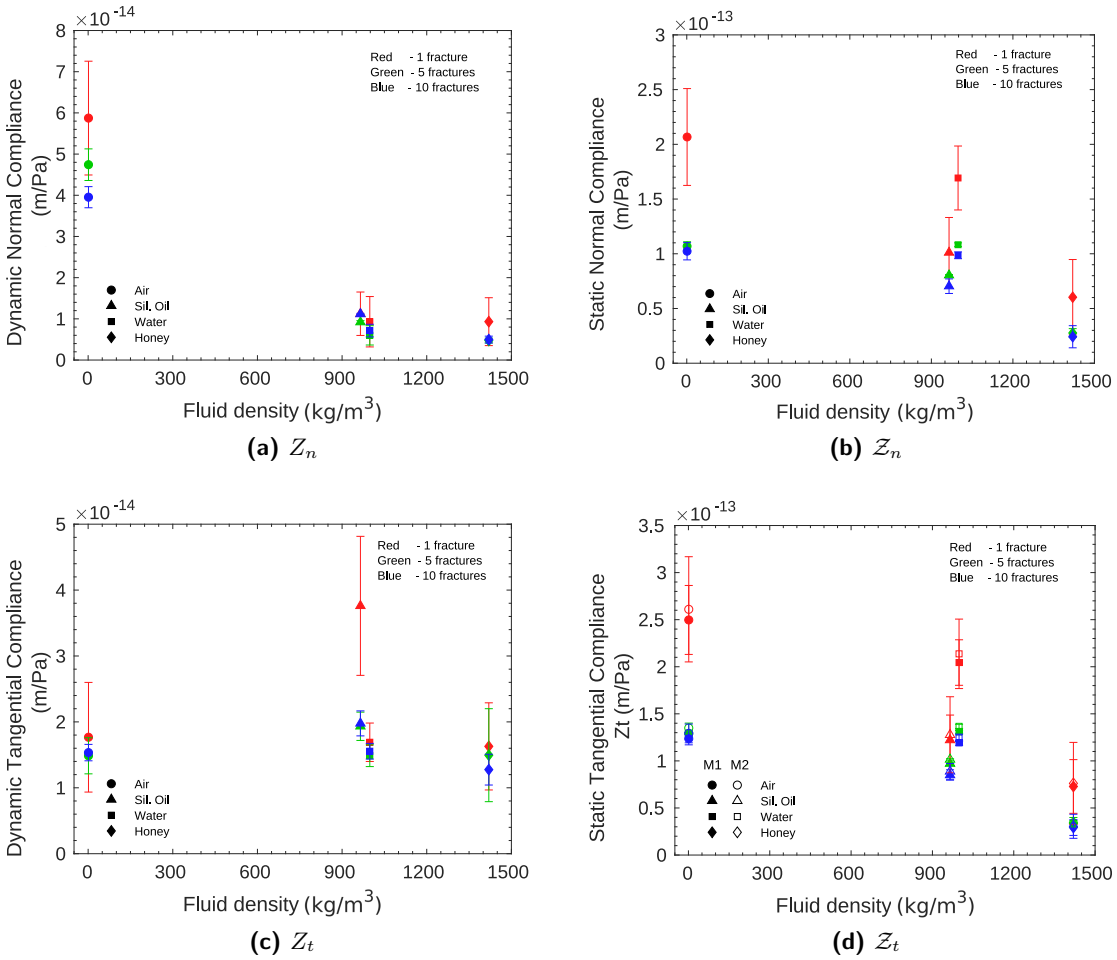

Figure 20. Fracture compliances versus density of the saturating fluid for the three fracture sets. (a) Dynamic normal compliance, (b) Static normal compliance, (c) Dynamic tangential compliance, and (d) Static tangential compliance. M1: Model where fractures are considered as planar distribution of small isolated areas of slip or cracks, and M2: Model where fractures are considered as planar distribution or imperfect facial contacts or a rough surface. Error bars in the figure represent the standard deviation associated with the mean value of the corresponding compliance value Z.

This indicates that the waves interact differently depending on the material properties of the infill. Both P- and S- waves exhibit attenuation in amplitude as the number of fractures increases. With 1 fracture, the waves are less scattered and maintain higher amplitudes, while with 5 and 10 fractures, the amplitude decreases. The increased attenuation with more fractures highlight that both types of waves are affected by the cumulative interaction with multiple fractures.

Table 3. Dynamic and Static compliances values for fracture from open literature.

Rock Type	Environment	Normal Compliance (m/Pa)	Tangential Compliance (m/Pa)	Density (kg/m^3)	Normal stress (MPa)	Reference
			Dynamic			
Shale	Dry	8.33×10^{-13}	—	2585	20	Zhou et al. (2020)
Granite	Dry	1.0×10^{-12}	—	2807	20	Zhou et al. (2020)
Limestone-1	Dry	1.14×10^{-14}	2.92×10^{-14}	—	—	Lubbe et al. (2008)
Limestone-2	Dry-ground	1.03×10^{-14}	3.74×10^{-14}	2662	—	Lubbe et al. (2008)
Limestone-2	Dry-polished	2.66×10^{-15}	6.00×10^{-15}	2662	—	Lubbe et al. (2008)
Limestone-2	wet (honey)	7.60×10^{-16}	2.82×10^{-14}	2662	—	Lubbe et al. (2008)
Granite (E35)	Dry	5.0×10^{-14}	1.61×10^{-13}	2650	20	Pyrak-Nolte et al. (1990b)
Granite (E30)	Dry	4.16×10^{-14}	8.33×10^{-14}	2650	20	Pyrak-Nolte et al. (1990b)
Granite (E35)	Wet (water)	4.0×10^{-14}	—	2650	20	Pyrak-Nolte et al. (1990b)
Granite (E30)	Wet (water)	3.86×10^{-14}	—	2650	20	Pyrak-Nolte et al. (1990b)
Aluminum	Dry	3.46×10^{-14} - 6.68×10^{-14}	3.39×10^{-14} - 5.16×10^{-14}	2702	20	This study
Aluminum	wet (water)	9.68×10^{-15} - 1.44×10^{-14}	3.42×10^{-14} - 4.12×10^{-14}	2702	20	This study
Aluminum	wet (Sil. Oil)	1.45×10^{-14} - 1.62×10^{-14}	4.41×10^{-14} - 9.95×10^{-14}	2702	20	This study
Aluminum	wet (honey)	7.00×10^{-15} - 1.46×10^{-14}	2.70×10^{-14} - 3.46×10^{-14}	2702	20	This study
			Static			
Granite (E35)	Dry	1.0×10^{-12} - 3.03×10^{-13}	—	2650	2.9-30	Pyrak-Nolte et al. (1987)
Granite	Dry	1.0×10^{-13} - 1.0×10^{-12}	—	—	2.2 -11.5	Rutqvist (1995)
Granite	Dry	5.6×10^{-13} - 2.6×10^{-12}	—	—	25 - 27	Makurat et al. (1991)
Aluminum	Dry	1.02×10^{-13} - 2.06×10^{-13}	— —	2702	20	This study
Aluminum	wet (water)	9.86×10^{-14} - 1.69×10^{-13}	—	2702	20	This study
Aluminum	wet (Sil. Oil)	7.03×10^{-14} - 1.01×10^{-13}	—	2702	20	This study
Aluminum	wet (honey)	2.41×10^{-14} - 6.03×10^{-14}	—	2702	20	This study

For P- waves, when comparing different fluid types, the air-filled fractures (green line) generally exhibit the lowest amplitude, while water, silicon oil, and honey show intermediate amplitudes, with honey (orange) producing slightly higher amplitudes than water (blue) and silicon oil (magenta) across the various number of fractures. Higher-density fluids tend to produce larger amplitudes because they reduce the impedance contrast between the aluminum solid medium and the fluid, allowing more energy to be transmitted through the fractures. Specifically, for P-wave amplitudes, in the case of a single

fracture, the percentage of amplitude reduction compared to the intact sample ranges from 62.55% for the dry case to only 8.47% for honey. For 5 and 10 fractures these values ranges from 99% for dry cases to 20% for honey respectively. Regarding the effect of the number of fractures, for 1 fracture, the waveforms are relatively smooth and similar for all fluids. However, as the number of fractures increases, scattering becomes more pronounced, especially for higher viscosity fluids like silicon oil and honey. These fluids show greater amplitude variations and waveforms distortions compared to water and air. The reduction in amplitude is also accompanied by an increase in P-wave travel times, which are delayed as fluid density decreases. For instance, in the case of a dry sample with one fracture, the travel time increases by 0.74%, whereas with honey, it only increases by 0.26%. This difference becomes more pronounced as the number of fractures increases, reaching 4.21% for dry and 0.69% for honey in the case of 10 fractures.

Regarding S-waves, the amplitude decay follows a similar trend to the P-wave in that it decreases as the number of fractures increases. However, the S-wave amplitudes are generally lower compared to P-waves, especially in the 10-fracture case, where the signal is significantly attenuated for all fluid types, with reductions ranging from 84% for the dry case to 72.66% for the honey case. In addition to amplitude reduction, S-wave travel times are delayed as the number of fractures increases and fluid density decreases. These delays are generally smaller than those observed for P-wave, ranging from 0.28% to 1.08% for the dry case and from 0.22% to 0.52% for the honey case as the number of fractures increases from 1 to 10.

Unlike the P-wave, the S-waveforms become more spread out as the number of fractures increases. In the case of air-filled fractures (green line), the amplitude behavior differs from that of P-waves; the S-waves amplitudes does not decrease as significantly in the air-filled case. Honey (orange) and silicon oil (magenta) cases exhibit more distinct amplitudes compared to water (blue) and air (green), especially in the 5 and 10 fracture cases. With 10 fractures, the fluids water and air show greater smoothing of the waveforms and reduced amplitude, while more viscous fluids like silicone oil and honey result in more distinct waveforms, though with scattering.

5.1.3 Wave velocities

Fractures typically increase the compliance of the surrounding matrix, leading to a reduction in seismic velocities which is associated with the delays in arrival times mentioned in the previous section.

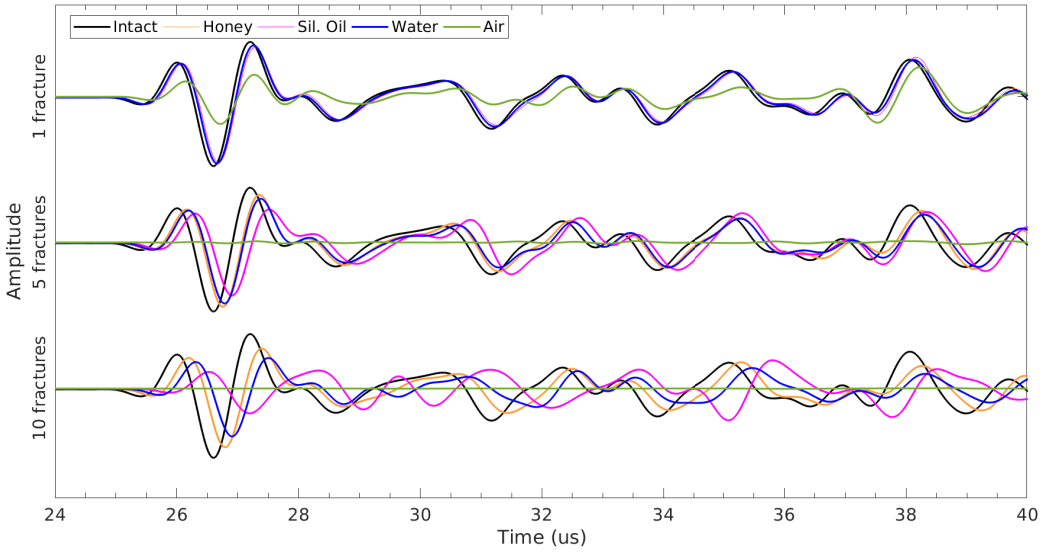

Figure 21. Observed P- waveforms through both intact and fractured specimens with single and multiple fluid-filled fractures under an uniaxial normal stress of 20MPa. All the amplitudes are normalized to the maximum amplitude of the intact specimen. The frequency of the ultrasonic transducer is 1MHz, which corresponds to P-wavelength $\lambda = 6.43$ mm.

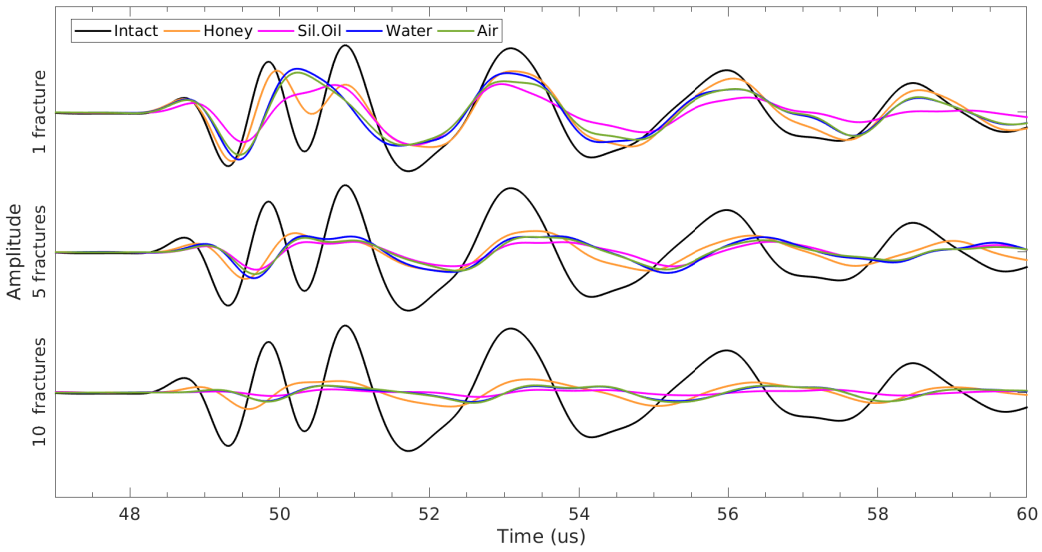

Figure 22. Observed S- waveforms through both intact and fractured specimens with single and multiple fluid-filled fractures under an uniaxial normal stress of 20MPa. All the amplitudes are normalized to the maximum amplitude of the intact specimen. The frequency of the ultrasonic transducer is 1MHz, which corresponds to S-wavelength $\lambda = 3.13$ mm.

Figures 23a and 23b shows the relationship between P- and S-wave velocities, the density of the infill material, and the number of fractures. I observe that, as the density of the fluid increases, P-wave velocities increase, demonstrating effective saturation of the fractures with the fluids, while S-wave velocities decrease initially and then increase upon the fluid density. For example, in the case with ten fractures, the P-wave velocity increases from 5926 m/s for the dry case to 6362 m/s for honey, while the S-wave velocity rises from 3084 m/s for the dry case to 3119 m/s for the honey case, with the lower value of 3067 m/s for the silicon oil case.

Conversely, as the number of fractures increases, wave velocities decrease. For instance, the average P-wave velocity for specimens with silicone oil infill ranges from 6401 m/s for one fracture to 6234 m/s for ten fractures. Additionally, the P-wave velocity approaches the value observed in the intact specimen (6432 m/s) as the fluid density increases. For P-waves, the percentage difference with respect to the intact sample is consistently larger compared to S-waves across different fluid types and fracture numbers. For example, with 10 fractures in dry conditions, the reduction in P-wave velocity is 7.86%, while the reduction in S-wave velocity is 1.77%. In the honey case with 10 fractures, the P-wave velocity reduction is 1.08%, while the S-wave velocity reduction is 0.67%.

S-waves show a relatively smaller percentage difference, particularly in the 1 and 5 fracture cases, where the reductions are minimal compared to P-waves. For example, with 1 fracture, the S-wave velocity reduction for dry conditions is 0.31%, while the P-wave reduction is 1.29%. These observations indicate that the effect of fractures and fluid properties is more pronounced on P-wave velocities, especially with an increased number of fractures. While S-wave velocities also decrease with fractures, the percentage difference remains relatively smaller across the different fluid types and fracture cases. Both wave types are affected by fractures and fluid properties, however, P-waves experience a more significant reduction in velocity, particularly in cases with more fractures and in dry conditions.

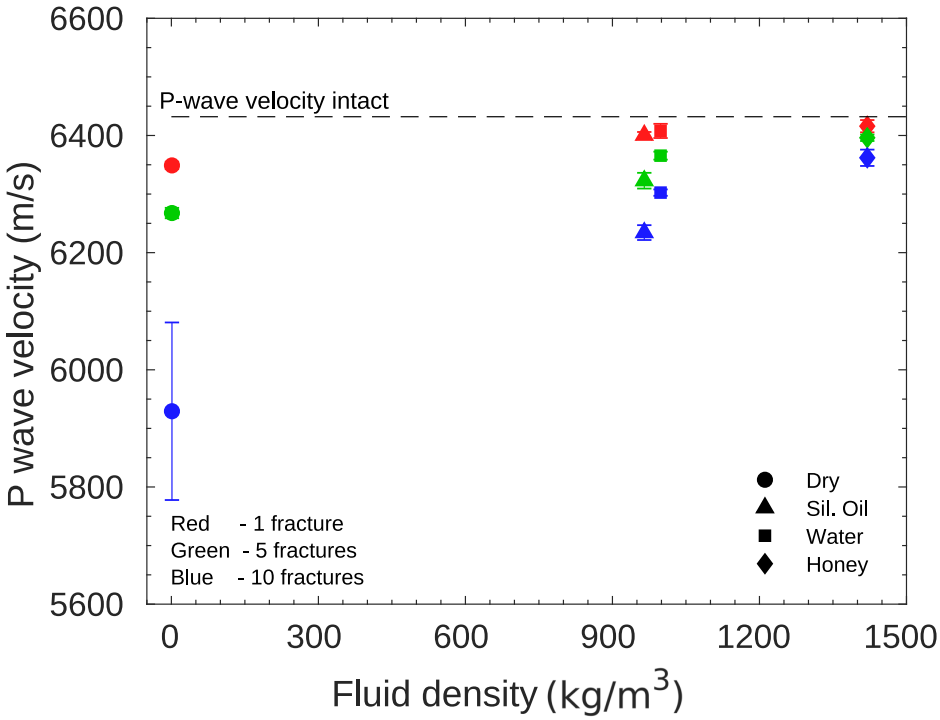

(a)

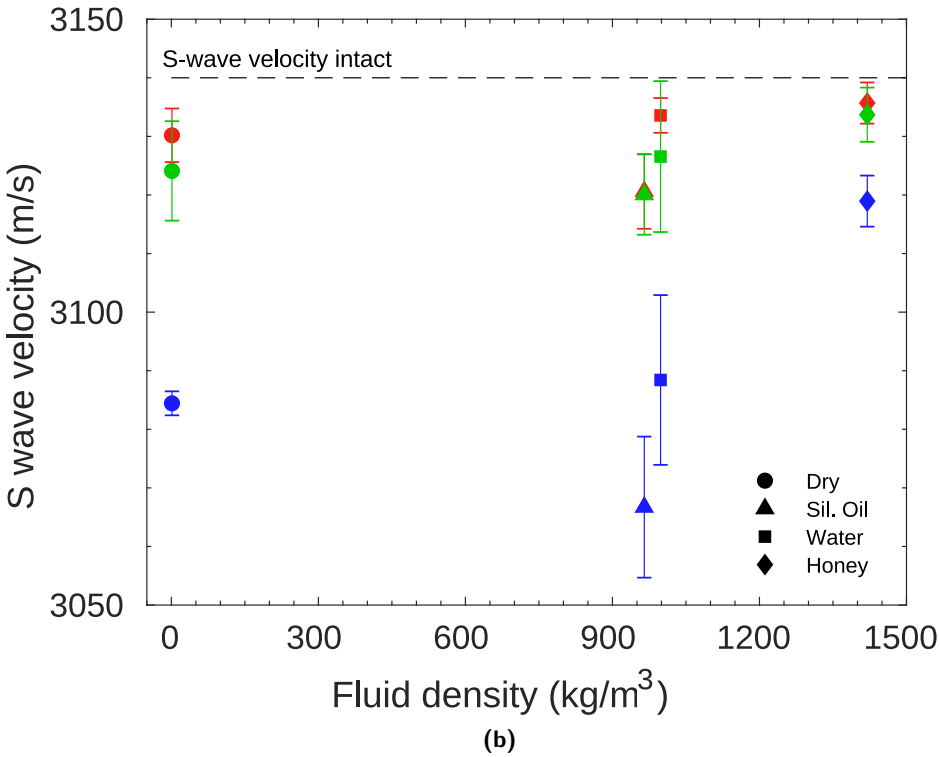

(b)

Figure 23. P- and S- wave velocity, versus fluids density for the three fractured samples. 1 fracture: red; 5 fractures: green; 10 fractures: blue. Error bars in the figure represent the standard deviation associated with the mean value of the P- and S-wave velocity.

5.1.4 Transmission Coefficient and quality factor Q

I estimated the P- and S-wave transmission coefficients across fractured specimens using equation 19. The resultant values are presented in figures 24a and 24b, which illustrates the transmission coefficient as a function of fluid density. For both waves, the transmission coefficient decreases as the number of fractures increases, for a single fracture, the transmission coefficient remains relatively high, even with lower-density fluids. However, as the number of fractures increases to 5 or 10, the impact on wave transmission becomes greater, especially for fluids with lower densities.

The transmission coefficient for P-wave increases as fluid density rises. Through all fracture cases (1, 5 and 10 fractures), denser fluids like honey and water show higher transmission coefficient, indicating more effective wave transmission. In contrast, in the dry case, the transmission is significantly lower, particularly for the case of 5 and 10 fractures, which shows a substantial wave attenuation in the absence of fluid. Even as the number of fractures increases, higher-density fluid continue to enhance the transmission coefficient. In dry conditions, the transmission coefficients range from 0.37 for a single fracture to 0.001 for ten fractures. Saturating fractures with fluids increases wave transmission, the coefficient values range from 0.892 to 0.915 for single fractures, from 0.688 to 0.899 for five fractures, and from 0.344 to 0.793 for ten fractures. The higher transmission coefficients are associated with honey as the infill material. Therefore, denser fluids facilitate better P-wave transmission across the fractured media by reducing the interaction of the wave with the fracture voids.

S-wave transmission coefficients exhibit a different trend compare to P-waves. For S-waves, the transmission coefficient in the dry case remain similar to those for fluids, showing less sensitivity to fluid density. It means, that S-wave is less affected by fluid presence in the fractures than P-wave. The values of this coefficient for the cases of air and honey (low and high density) are 0.793 to 0.899, 0.160 and 0.273 for 1 and 10 cases respectively. In addition, it is noticeable in the figures that P-wave transmission coefficient exhibit a substantial gap between the dry case and fluid-filled fractures, while S-waves maintain relatively consistent values across different fluids, including the dry case. These results show a greater sensitivity of P-waves to fluid presence and density in fractured media.

The reasons for the increase in the amplitude transmission (i.e., low attenuation) in fractures saturated with liquids in contrast to the dry cases include the following: (a) the open spaces resulting from the contact between the roughness of the surfaces of the aluminum discs in contact are filled with different types of fluid, enhancing the coupling and transmission of the wave, and (b) liquids decrease

the acoustic-impedance contrast as the density increases, reducing scattering and reflections.

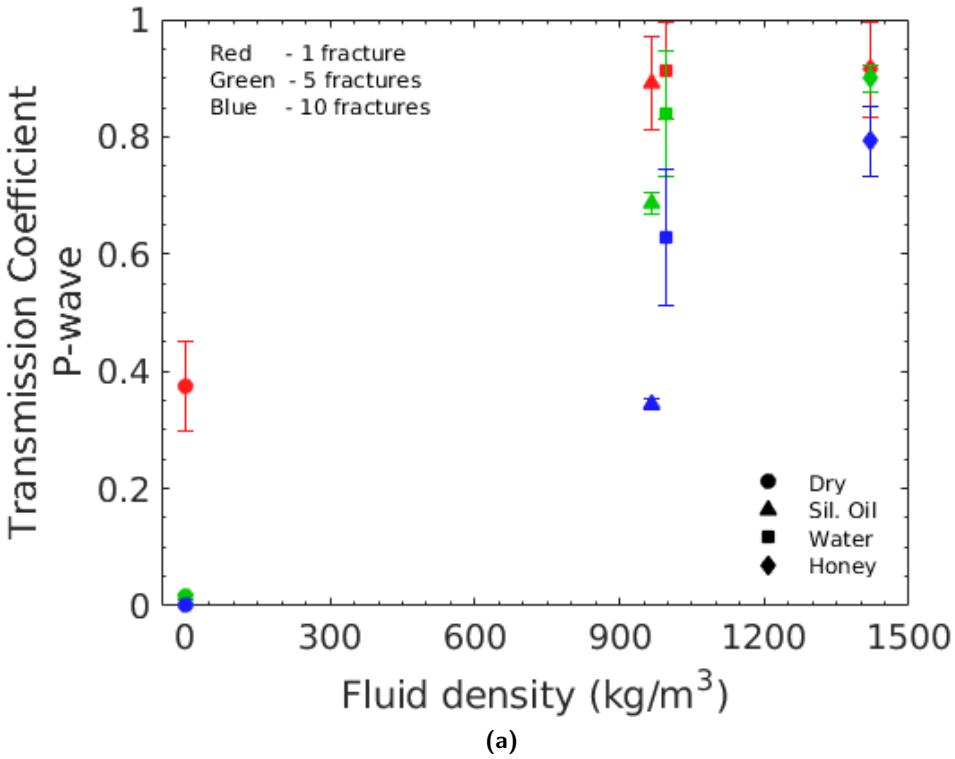

(a)

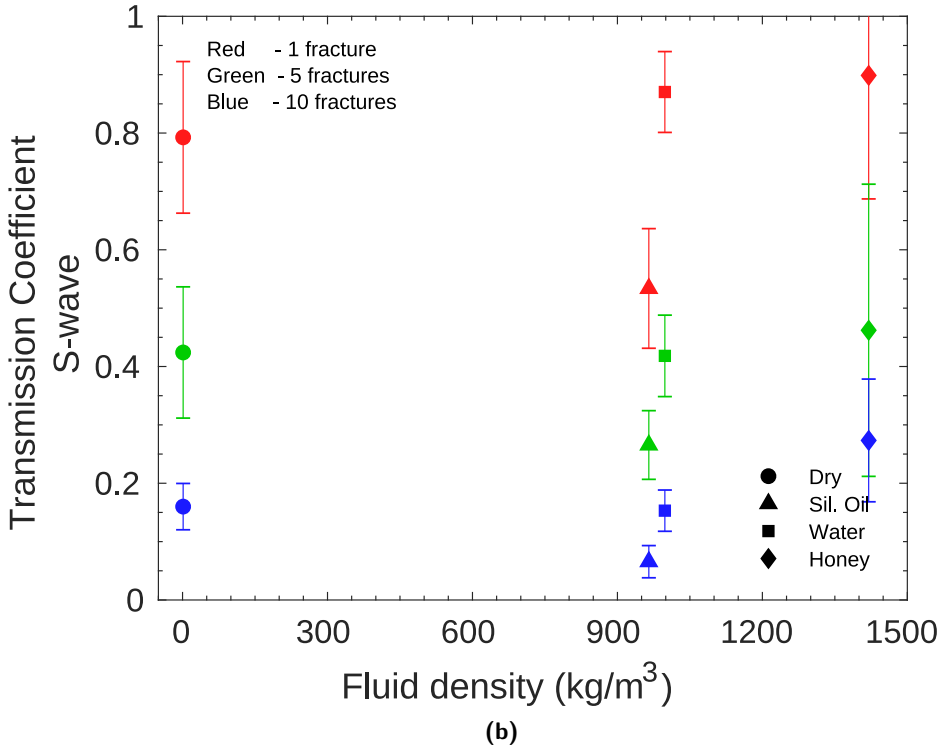

(b)

Figure 24. Transmission coefficients for P- and S-wave of fractured specimens versus density of the saturating fluids for the three fracture sets; 1 fracture: red, 5 fractures: green, 10 fractures: blue. Error bars in the figure represent the standard deviation associated with the mean value of the P- and S-wave transmission coefficient.

The quality factor Q is inversely related to the energy lost due to different mechanisms such as scattering, absorption, and transmission in the medium. A higher Q indicates less attenuation, meaning the medium is more efficient at preserving wave energy. In this study, the quality factors for P- and S- wave, Q_p, and Q_s, were calculated using the Spectral Ratio Method, equation (26). Figures 25a and 25b show the P- and S-wave quality factor as a function of fluid density.

The Q_p values increase with fluid density in all cases. In the dry conditions, they are notably lower, particularly in specimens with greater number of fractures, reflecting higher attenuation and reduced wave transmission efficiency due to scattering and energy losses caused by multiple unfilled discontinuities. The number of fractures has a pronounced effect on Q_p, for example, in the 10-fracture case (blue icons), the quality factor starts very low in the dry case but increases significantly with fluid saturation. With only 1 fracture (red icons), the Q_p is generally higher, even in dry conditions, showing that fewer fractures lead to less attenuation. As I mentioned before, denser fluids such as honey help to preserve wave energy, due to the enhanced coupling and reduced scattering effects. Q_s exhibits a distinct pattern as fluid density increases: it initially decreases before rising. Overall, Q_s values are smaller than Q_p, indicating that S-waves experience more attenuation than P-waves under similar experimental conditions. This trend is consistent across varying number of fractures, with higher-density fluids like honey, showing higher Q_s values and better energy preservation. The values of Q_s shows a much smaller difference between dry and liquid-saturated cases, indicating that S-wave is less sensitive to changes in fluid density compared to Q_p. The lower Q values for S-wave compared to the P-wave (Q_p) indicate that S-wave is more attenuated. In summary, both Q_p) and Q_s quality factors are influenced by fluid density. Q_p generally increases with fluid density, exhibiting a greater difference between dry and liquid cases due to its compressional nature. In contrast, Q_s shows a different trend, it exhibits only minor variations, reflecting its shear-dominated nature and lower sensitivity to fluid properties. Despite this, Q_s generally experiences higher attenuation in fluid-saturated media. Denser fluids mitigate attenuation effects for both wave types, leading to higher quality factors and better energy preservation overall.

For comparison, figure 26 shows the relationship between Q_p and fluid viscosity, serving as example of the irregular trend observed across wave properties such as velocity and transmission coefficient for both P- and S- waves. Unlike the clear trend observed with fluid density, the relationship between Q_p and viscosity does not follow a regular pattern. For example, water, despite being less viscous than silicon oil and honey, exhibits higher Q_p values. This irregularity suggests that viscosity alone may not directly govern Q_p; instead, it could interact with other properties, such as fluid density and fracture number, in a more complex manner.

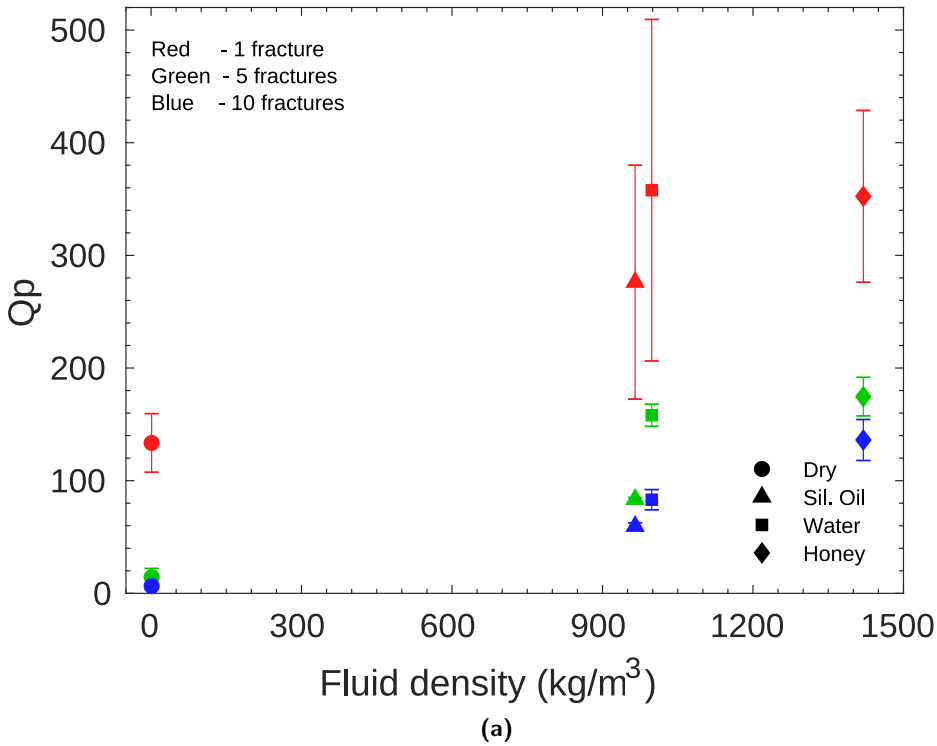

(a)

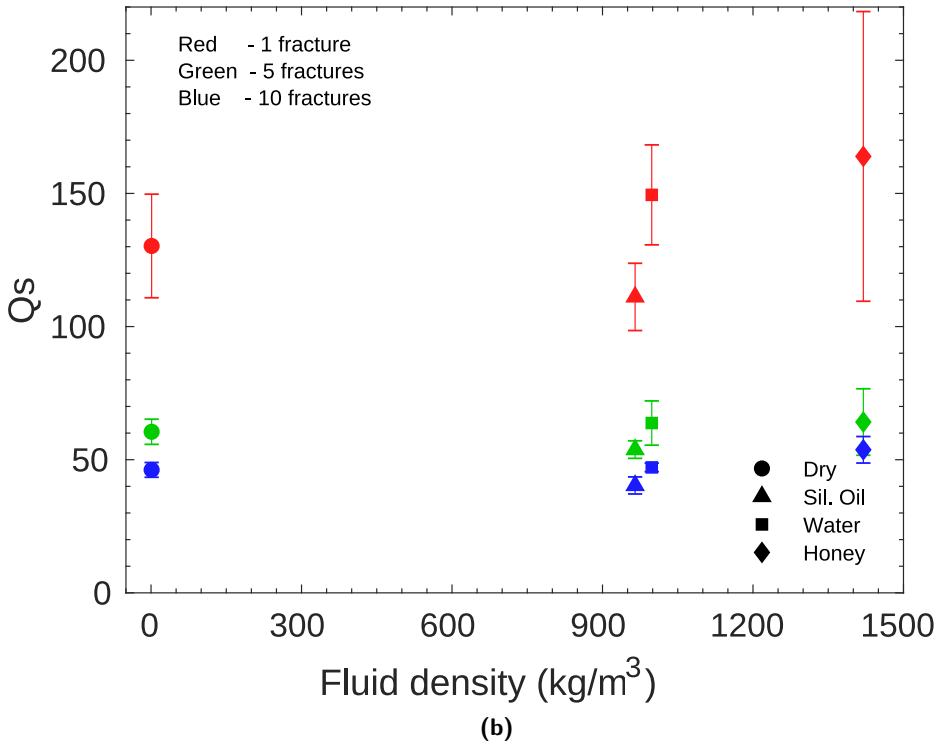

(b)

Figure 25. P- and S-wave quality factor, Q_p and Q_s, versus density of the saturating fluids for the three fracture sets; 1 fracture: red, 5 fractures: green, 10 fractures: blue. Error bars in the figure represent the standard deviation associated with the mean value of the P- and S-wave quality factor.

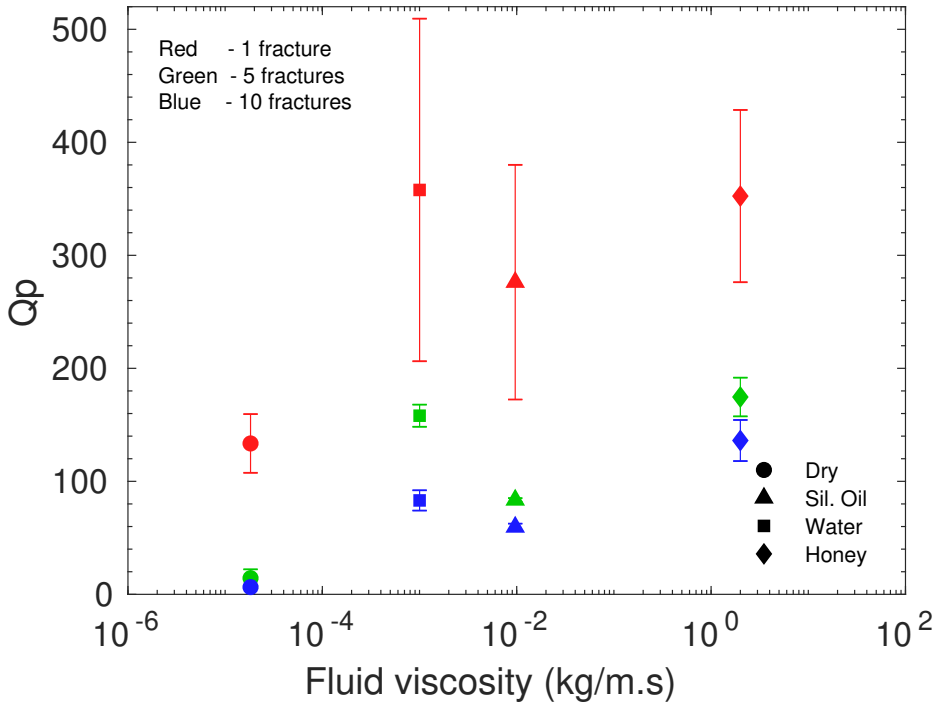

Figure 26. P-wave quality factor, Q_p, versus fluid viscosity for the three fractured samples; 1 fracture: red, 5 fractures: green, 10 fractures: blue. Error bars in the figure represent the standard deviation associated with the Q_p mean value.

5.2 Numerical results

5.2.1 Key wave parameters : Wave velocities, Transmission Coefficient and Quality Factor Q

These results were generated using the dynamic compliances estimated from laboratory ultrasonic tests under uniaxial normal stress at 20 MPa. In the numerical simulations, the same boundary conditions as in the laboratory experiments were applied, allowing for direct comparison between experimental observations and modeled wave propagation behavior.

Figures 27 and 28 show the P- and S-waveforms respectively, from the numerical simulations, including all fluids and fracture cases. Both the P- and S-wave waveforms are normalized to the maximum amplitude of the intact specimen, allowing for a direct comparison of the effects of different fluids (honey, silicon oil, water and air) and the presence of fracture. The numerical simulations successfully capture the general trends in wave behavior, such as amplitude reduction and phase shifts with increasing fracture numbers, in correspondence with the laboratory waveforms presented in figures 21 and 22.

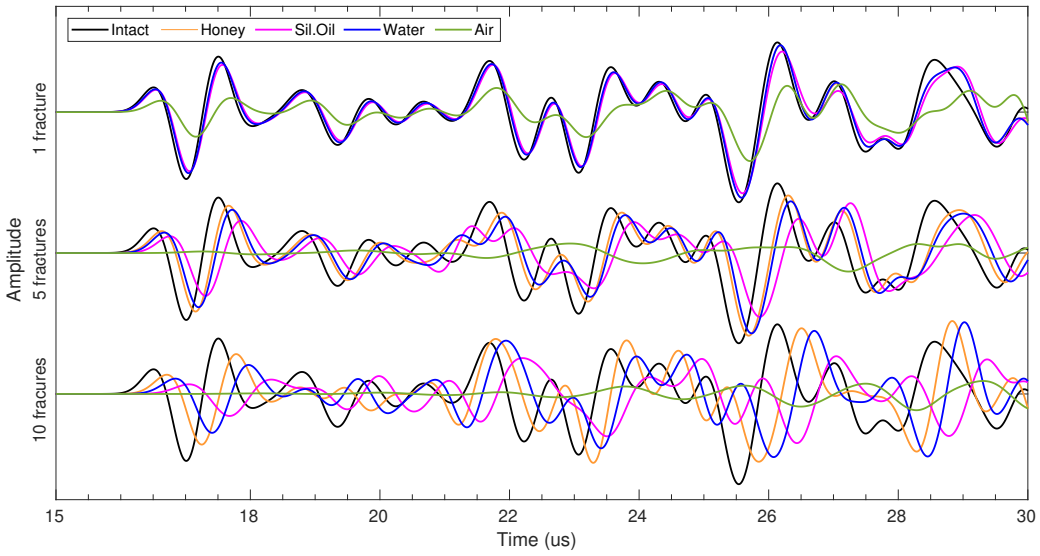

Figure 27. Simulated P-waveforms through intact and fractured specimens from numerical simulations using dynamic compliances estimated from laboratory ultrasonic tests as inputs. All the amplitudes are normalized to the maximum amplitude of the intact specimen. These results should be compared with those in figure21.

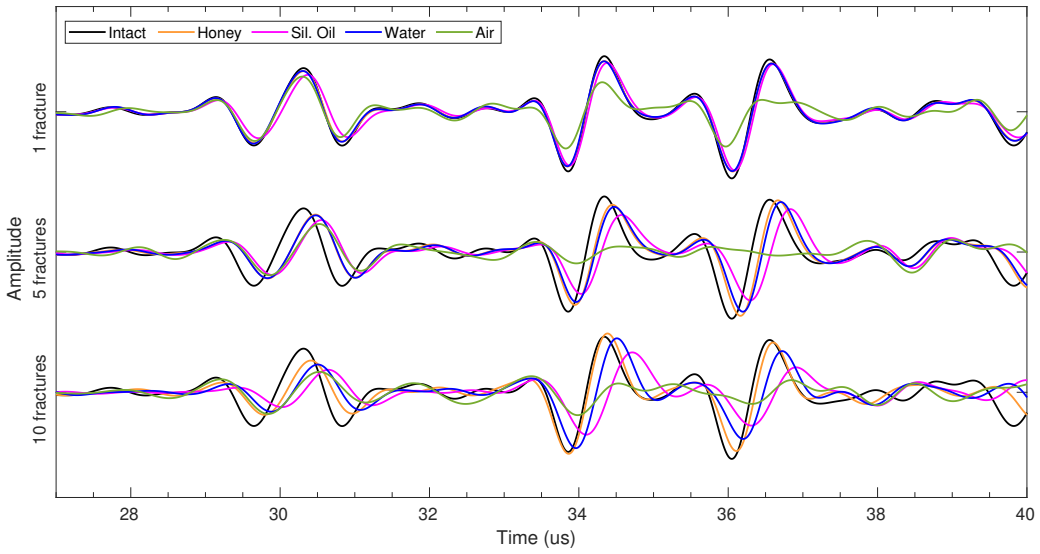

Figure 28. Simulated S-waveforms through intact and fractured specimens from numerical simulations using dynamic compliances estimated from laboratory ultrasonic tests as inputs. All the amplitudes are normalized to the maximum amplitude of the intact specimen. These results should be compared with those in figure22.

The P-wave (Figure 27) generally shows a more regular attenuation pattern, with denser fluids preserving more energy. Additionally, phase shifts and travel times are predictable as the fracture number increases. The S-wave (Figure 28), in particular, shows distinct behavior in terms of amplitude reduction and

phase delay, especially for fractures filled with fluids of different viscosities and densities. For example, in the case of more viscous fluid like honey, the energy transmission is better, therefore it shows a higher amplitude in the numerical results, while in the experimental results, the energy transmission is notably diminished. This discrepancy highlights the limited sensitivity of the S-wave to fluid and fracture properties, leading to less predictable transmission behavior compared to the P-wave.

Overall, both P- and S-wave simulations show good correspondence with the experimental data, capturing key trends in amplitude reduction and travel time delay, confirming that dynamic compliances used effectively reflect the fracture properties and fluid distinctions. However, the simulations for S-wave reveal more deviation from the experimental results, possibly due to the complex shear behavior of the fluids and fractures.

Figures 29a, 30a, 31a, display the results for wave velocity, transmission coefficient, and quality factor as functions of fluid density for P-wave, while Figures 29b, 30b, 31b show the corresponding results for S-wave. In these figures, open icons represent numerical results, while solid icons indicate laboratory results. These figures show a trend consistent with the laboratory results, indicating that dynamic compliances accurately capture the effect of fluid density on wave propagation by using LSM to model fractures filled with fluids.

The percentage differences in P-wave velocity for all fracture sets with various fluids are under 5%. However, the differences are larger for the transmission coefficient and quality factor Q_p. For the transmission coefficient, the percentage difference is below 13% for liquids and generally increases with the number of fractures. In the dry case, the percentage difference became increasingly negative as the number of fractures increased, indicating less attenuation in numerical simulations than in laboratory tests.

The quality factor, Q_p, exhibit notable variability. In dry conditions, the percentage differences range from -55.63$\%$ to 57.78$\%$, with larger discrepancies pointing to significantly less attenuation in the numerical simulations. In contrast, with liquid-saturated fractures, the difference for Q_p is narrower (21.71$\%$ to 53.13$\%$). The percentage difference in the transmission coefficient and Q_p consistently shows lower values for honey and higher values for dry cases.

In parallel, the S-wave parameters reveal a distinct response to fluid properties and the number of fractures. The S-wave velocities generally align closely between laboratory and numerical results, with percentage differences remaining minimal (under 3%) across all cases, indicating that V_s is less sensitive to fluid type and number of fractures compared to the P-wave.For the transmission coefficient, the

deviations are more substantial, particularly with an increase in the number of fractures. In dry conditions, the transmission coefficient differences become highly negative, especially with more fractures as its value is 2.5 times larger than the experimental, showing that the numerical model underestimates S-wave transmission loss, particularly in the presence of multiple fractures and viscous fluids like silicon oil.

The quality factor Q_s for S-wave show moderate variability, with differences that increase with the number of fracture and vary with fluid type. Under dry conditions, discrepancies in Q_s are generally bigger, because the numerical model underestimates attenuation. This means that amplitude reduction is less pronounced in the simulations compared to the laboratory experiments, particularly in cases with multiples fractures.

These observation about S-wave reveals that while the model performs robustly for S-wave velocities, it exhibits limitations in replicating the transmission and attenuation characteristics of S-wave in fluid-filled fracture media. The transmission coefficient and quality factor for S-wave are sensitive to the fluid viscosity and density but differ from the experimental results.

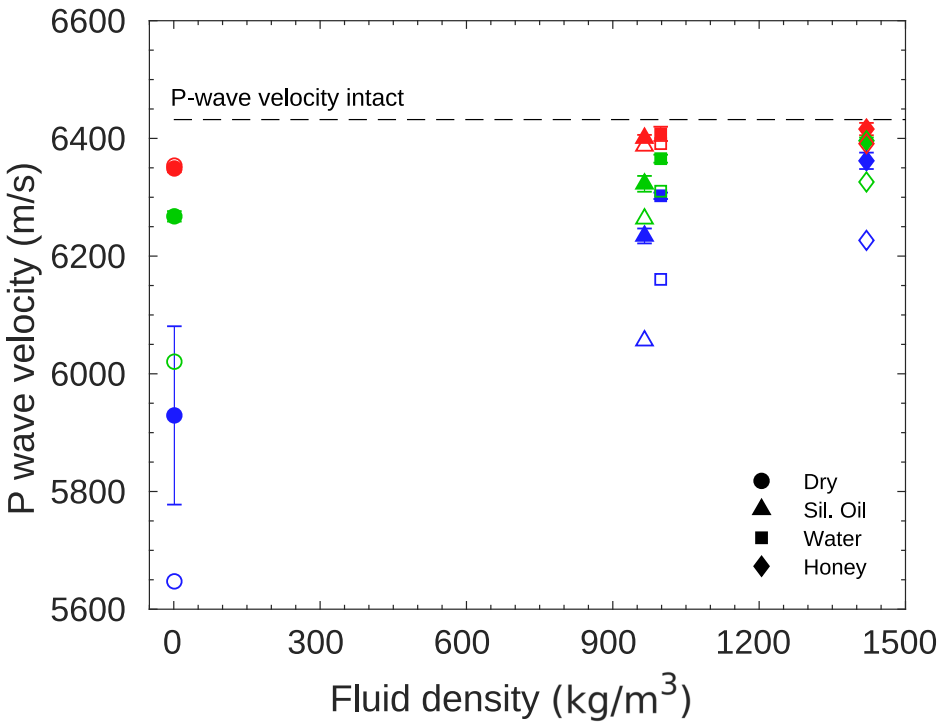

(a) V_p

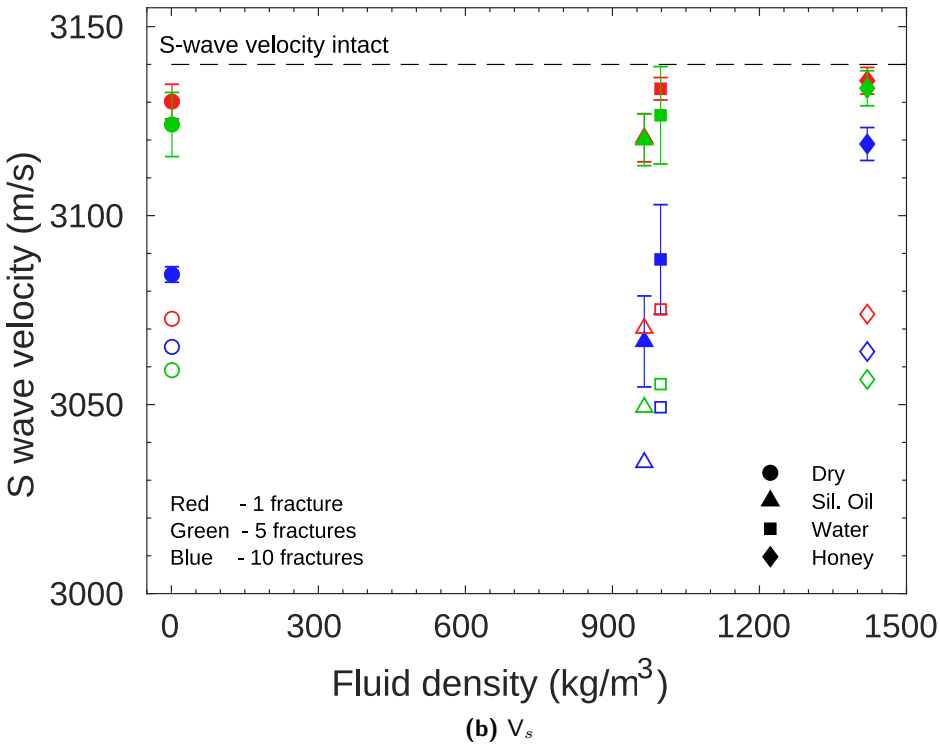

(b) V_s

Figure 29. P- and S-wave velocity as a function of fluid density, open icons correspond to the numerical results and filled icons to laboratory tests. Error bars in the figure represent the standard deviation associated with the mean value of the V_p and V_s.

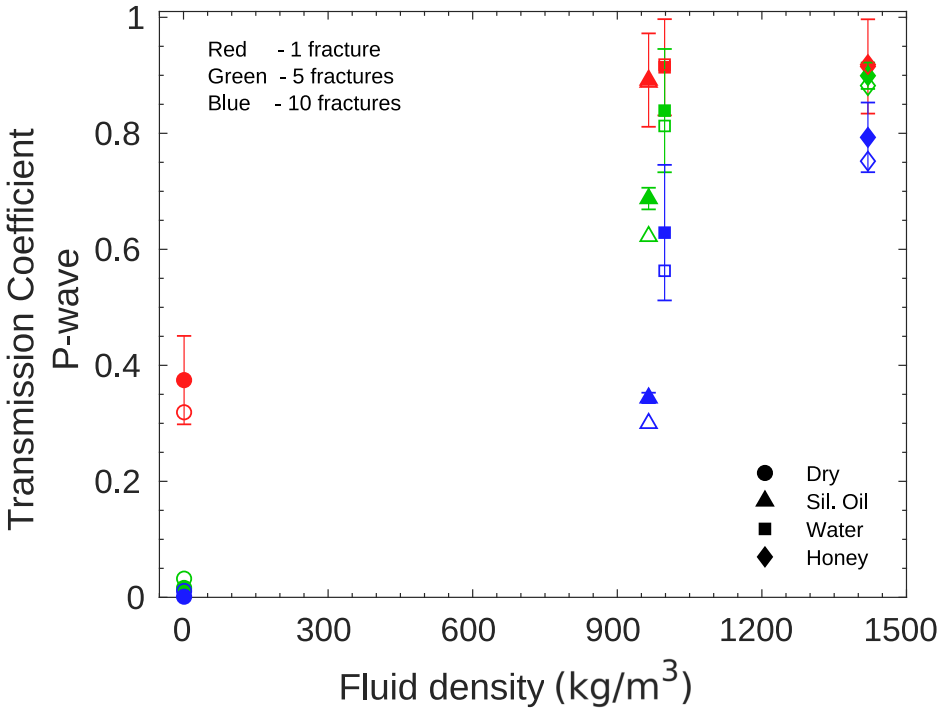

(a) TC_p

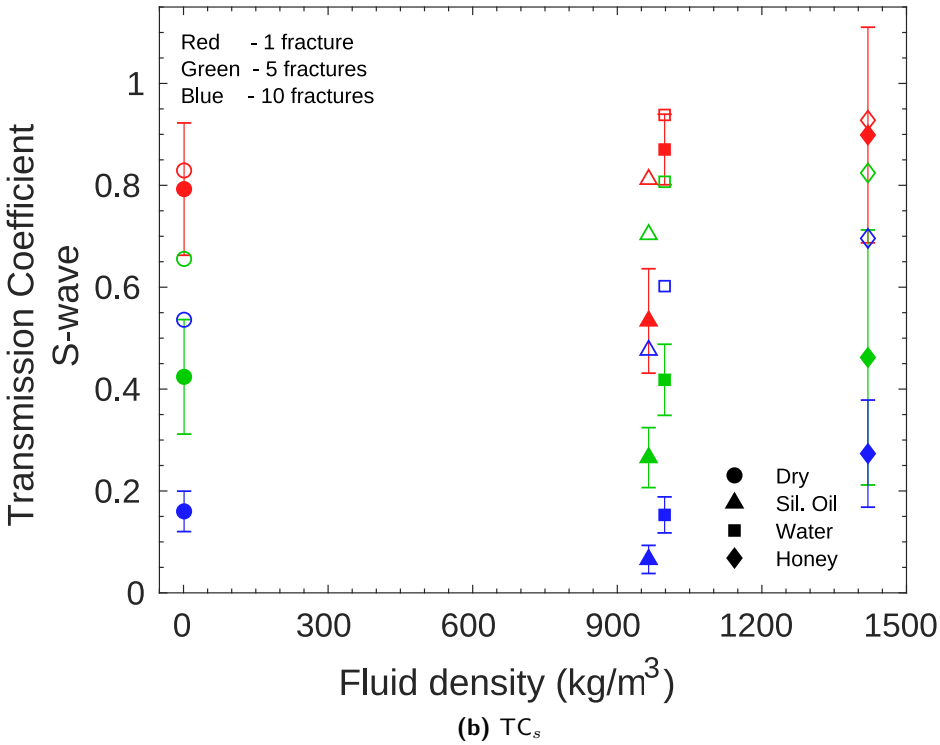

(b) TC_s

Figure 30. Transmission Coefficient for P- and S-wave as a function of fluid density, open icons correspond to the numerical results and filled icons to laboratory tests. Error bars in the figure represent the standard deviation associated with the mean value of the transmission coefficient.

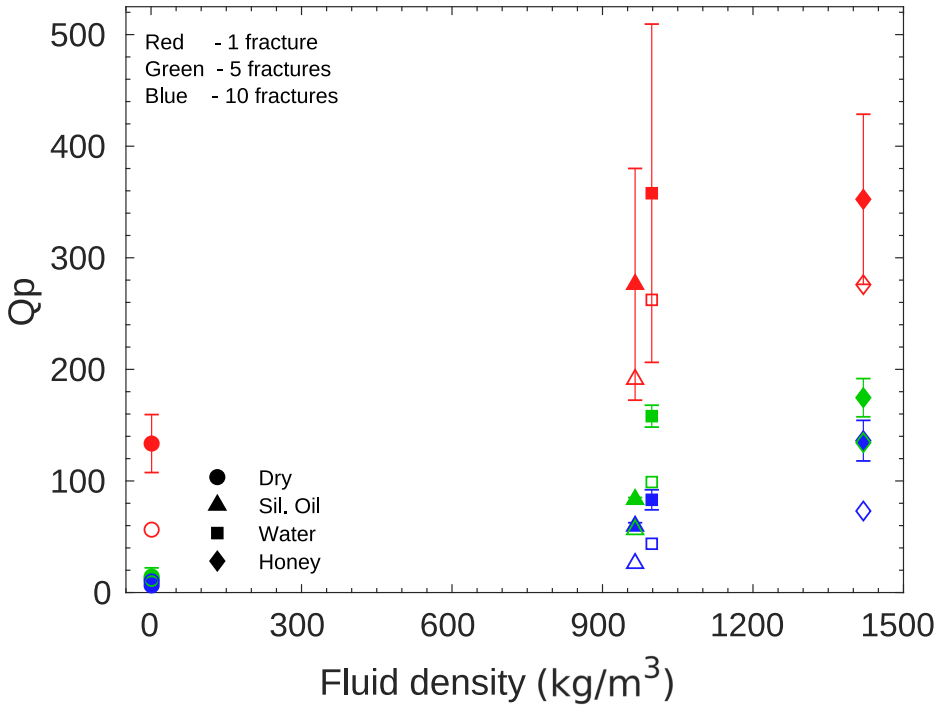

(a) Q_p

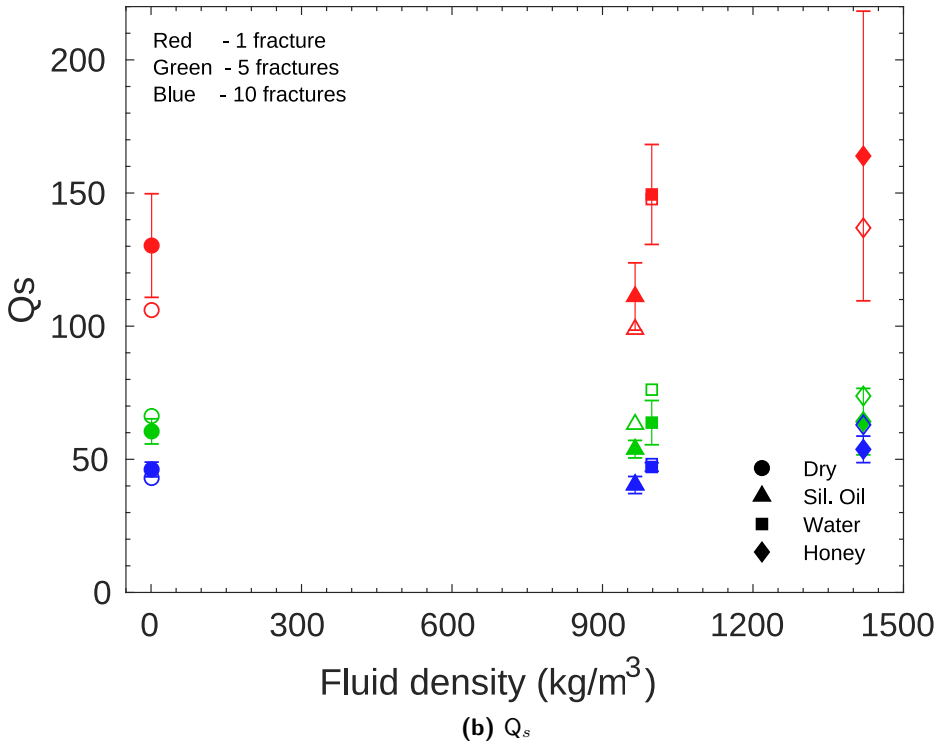

(b) Q_s

Figure 31. Quality factor Q_p and Q_s as a function of fluid density, open icons correspond to the numerical results and filled icons to laboratory tests. Error bars in the figure represent the standard deviation associated with the mean value of the Q.

5.2.2 Displacement field

In this section, to illustrate the wave field propagation behavior and its interactions with fractures, I present snapshots of the displacement field obtained from the numerical simulations, the color scale used in this section indicates displacement amplitudes (blue for negative and red for positive displacement). These figures are reproduced from Ramos-Barreto et al. (2025).

Figure 32 shows the simulated wavefield in a 3D cylindrical domain at $t = 49$ μs, capturing the magnitude of the displacement field for both the P- and S-wave components. Figure 32a illustrates the propagation of the P-wave, characterized by compressional motion, while figure 32b, which involves shear motion perpendicular to the direction of propagation. The visualizations highlight the differences in wavefront geometry and propagation between the two types of waves.

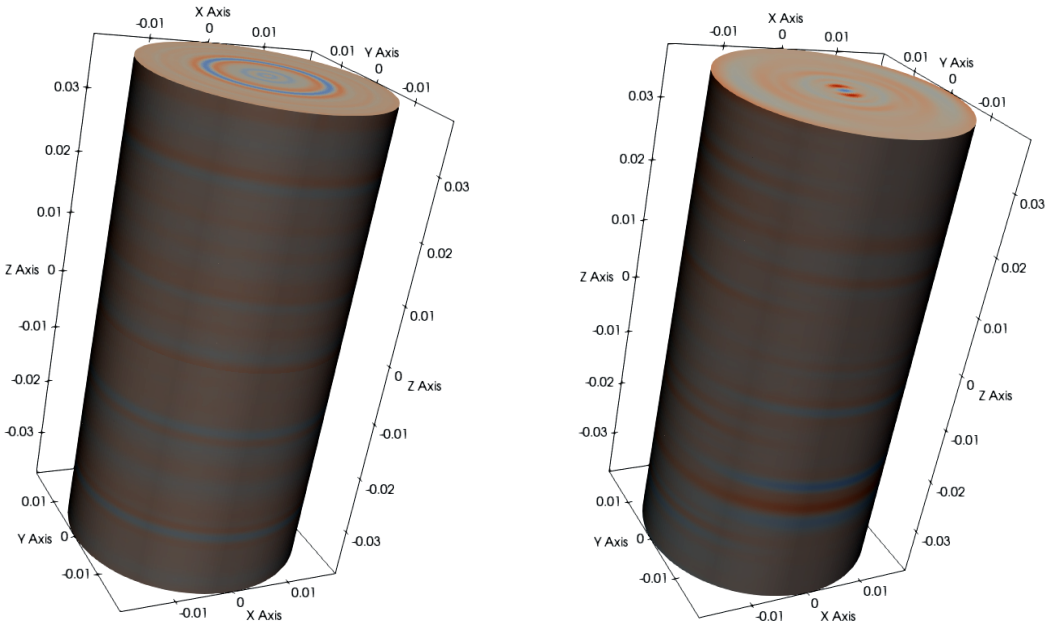

(a) Magnitude of the displacement field for P-wave.

(b) Magnitude of the displacement field for S-wave.

Figure 32. Wavefield in a 3D cylindrical domain at $t = 49$ μs.

I did a closer examination of the displacement field snapshots to observe how wave propagation behaves under different number of fractures (1, 5 and 10 fractures) and fluid types. The results are presented in two cases: (a) constant fluid with varying numbers of fractures, and (b) constant number of fractures with different fluid type. Each case is shown for both P- and S- waves.

To make a reliable comparison between wave types, different times were selected for the P- and S-waves. These times are based on the velocity ratio V_p/V_s, so the wavefields are captured at comparable propagation distances.

5.2.2.1 Varying fracture number

Figure 33 shows the vertical displacement field u_z for three different numbers of fractures and two fluid types: air (top row) and honey (bottom row). These fluids represent the extreme casesair with low density and low viscosity, and honey with high density and high viscosityhighlighting the impact of fluid properties on wave propagation.

As the number of fractures increases, wave scattering becomes more pronounced, particularly in the air-filled models. The strong impedance contrast and lower values of viscosity lead to distinct interference patterns and disruption of the coherent wavefront. In contrast, the honey-filled cases exhibit smoother wavefields. The higher density and viscosity reduces reflections and scattering, enabling more efficient energy transmission and preserving wavefront coherency even in densely fractured media.

Figure 34 shows the horizontal displacement field u_x, highlighting S-wave propagation through models with different numbers of fractures with air and honey fluids, representing contrasting cases.

Compared to the P-wave results (Figure 33), the S-wave displacement fields exhibit greater consistency across fluid types. The general wavefront shapes, reflection patterns, and spatial energy distributions remain similar between air- and honey-filled fractures. The main distinction is in amplitude: honey-filled cases show slightly stronger displacement, reflecting improved energy transmission due to the higher density and viscosity of honey. However, these effects are subtle, consistent with the expected lower sensitivity of S-waves to fluid properties.

As the number of fractures increases (left to right), the wavefields show minor variations, but overall coherence and symmetry are preserved. This further supports the observation that S-waves are less affected by fracture infill properties (Yang et al., 2024), particularly in contrast to the more fluid-sensitive P-wave fields.

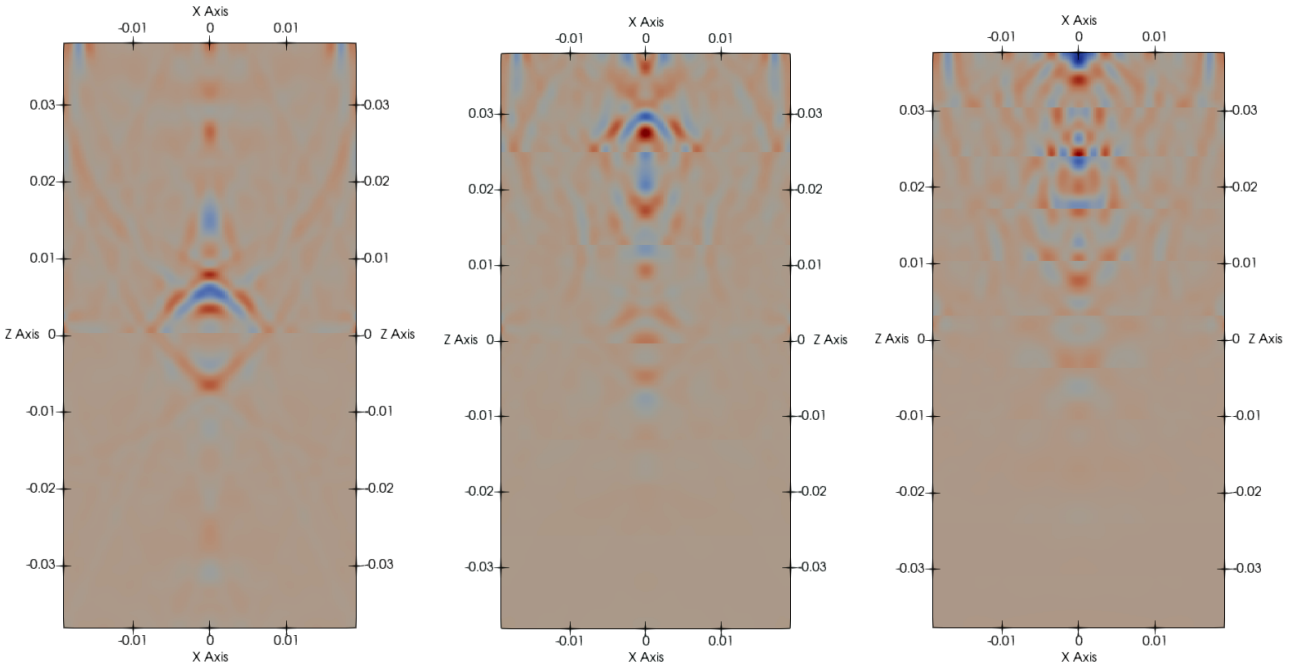

(a) u_z; $f_n = 1$; air **(b)** u_z; $f_n = 5$; air **(c)** u_z; $f_n = 10$; air

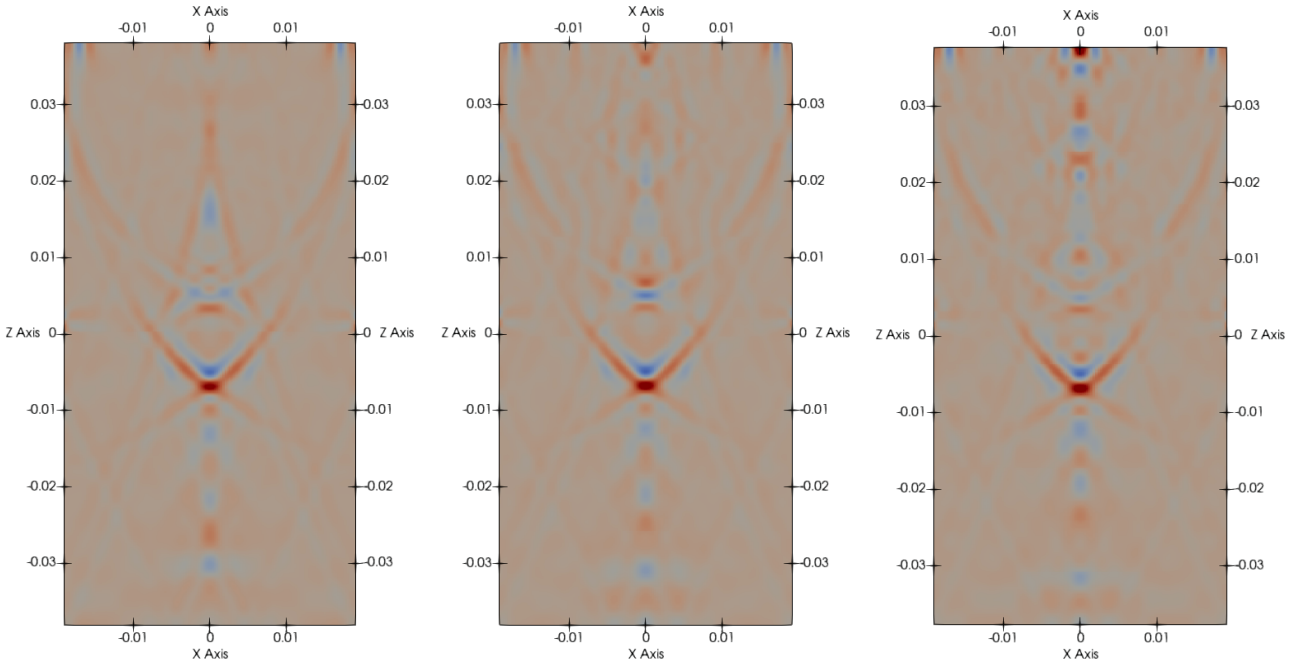

(d) u_z; $f_n = 1$; honey **(e)** u_z; $f_n = 5$; honey **(f)** u_z; $f_n = 10$; honey

Figure 33. Vertical displacement u_z snapshots at $t = 28$ μs, on the x-z plane for different number of fractures (f_n) and fluid types. The top row corresponds to air-filled fractures, while the bottom row corresponds to honey-filled fractures. From left to right, the fracture spacing decreases.

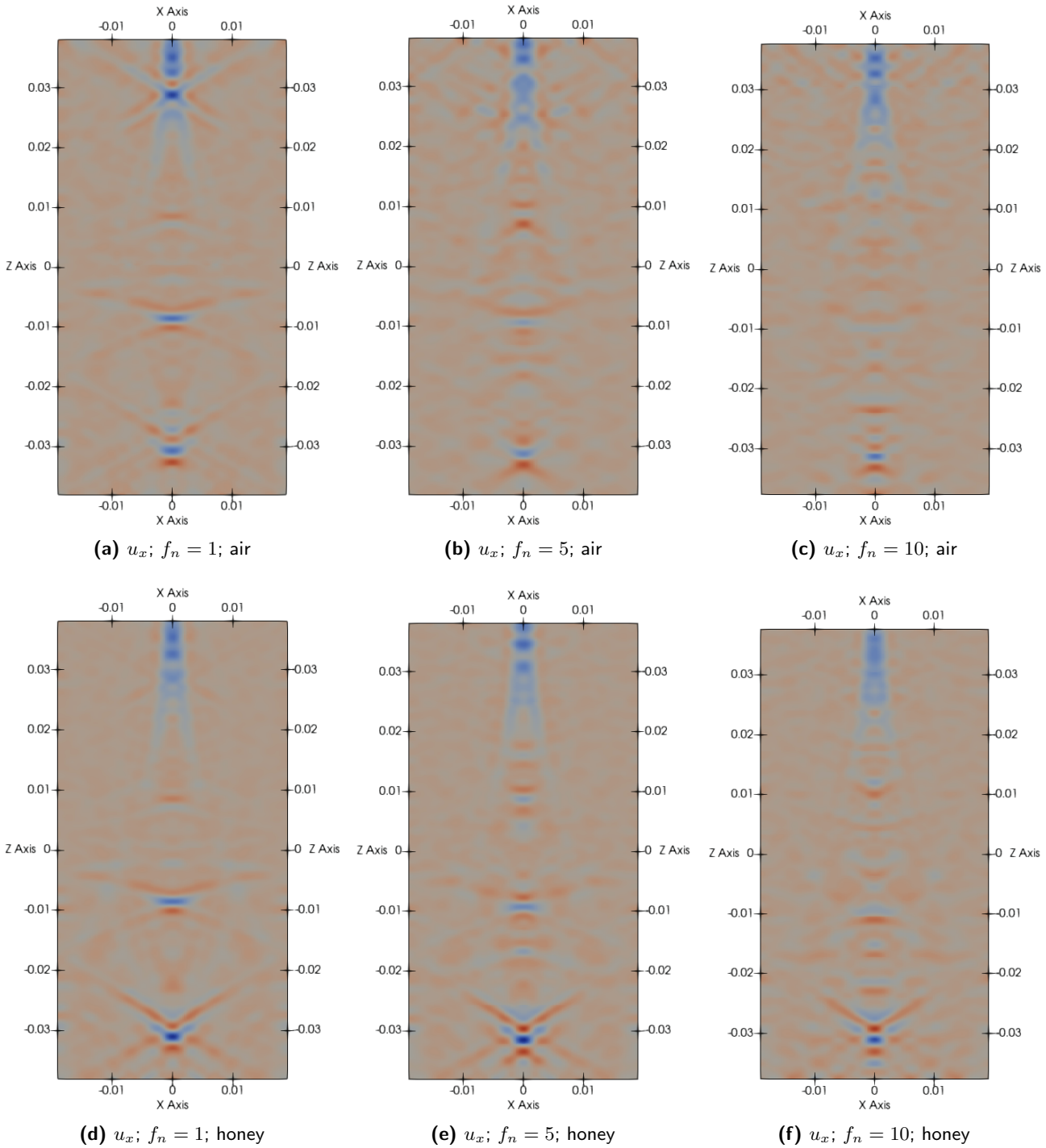

(a) u_x; $f_n = 1$; air **(b)** u_x; $f_n = 5$; air **(c)** u_x; $f_n = 10$; air

(d) u_x; $f_n = 1$; honey **(e)** u_x; $f_n = 5$; honey **(f)** u_x; $f_n = 10$; honey

Figure 34. Horizontal displacement u_x snapshots at $t = 49$ μs, on the x-z plane for different number of fractures (f_n) and fluid types. The top row corresponds to air-filled fractures, while the bottom row corresponds to honey-filled fractures. From left to right, the fracture spacing decreases.

5.2.2.2 Varying fluid type

Figures 35 and 36 present the vertical and horizontal displacement fields (u_z and u_x) for a fixed fracture number ($f_n = 1$), with varying fluid infills: air, water, silicone oil, and honey.

In the u_z snapshots (Figure 35), P-wave behavior is strongly influenced by fluid type. As fluid density and viscosity increase, the wavefronts become uniform and less distorted. Air-filled fractures exhibit stronger reflections, higher scattering, and more distinct interfaces, whereas honey-filled fractures show reduced distortion and enhanced wave transmission.

In contrast, u_x, Figure (36) are largely insensitive to fluid changes. While denser fluids slightly enhance amplitude, the overall wavefront shape and spatial energy distribution remain consistent across all cases. This reinforces the lower sensitivity of S-waves to fracture fill properties, as expected from their propagation mechanism.

5.3 Comparison between numerical and laboratory results

The numerical results (open icons) for P-wave velocity, transmission coefficient and quality factor, shown in figures 29a, 30a and 31a, align closely with the laboratory results (filled icons), especially for P-wave velocity. This agreement between numerical and laboratory results not only validates the modeling approach but also confirms that the dynamic compliance values derived from ultrasonic pulse experiments effectively capture the influence of fluid properties on wave propagation. The close match for P-wave velocity highlights the ability of the numerical simulation to accurately replicate wave arrival times and their dependency on fluid density.

However, as seen in figures 30a and 31a, the percentage difference and discrepancies are more pronounced for the transmission coefficient and quality factor. This suggests that while compliance from laboratory experiments, combined with the numerical approach, provide a reliable baseline for wave dynamics, they may not fully account for attenuation mechanism observed in laboratory experiments. This highlights the challenges in simulating energy loss and wave attenuation, especially with multiple fractures and varying fluid types.

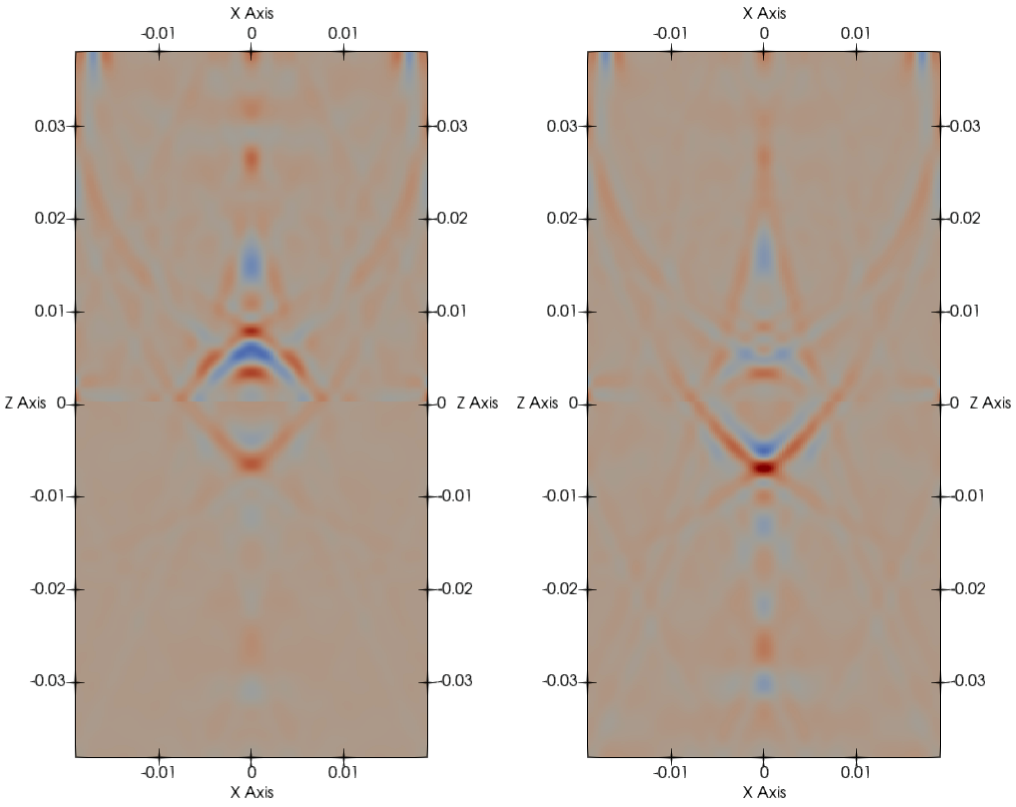

(a) u_z; $f_n = 1$; air

(b) u_z; $f_n = 1$; water

(c) u_z; $f_n = 1$; Sil. Oil

(d) u_z; $f_n = 1$; honey

Figure 35. Displacement field u_z at $t = 28$ μs, on the x-z plane fixed fracture number ($f_n = 1$) with the four different infill fluids (a) air, (b) water, (c) silicon oil, and (d) honey.

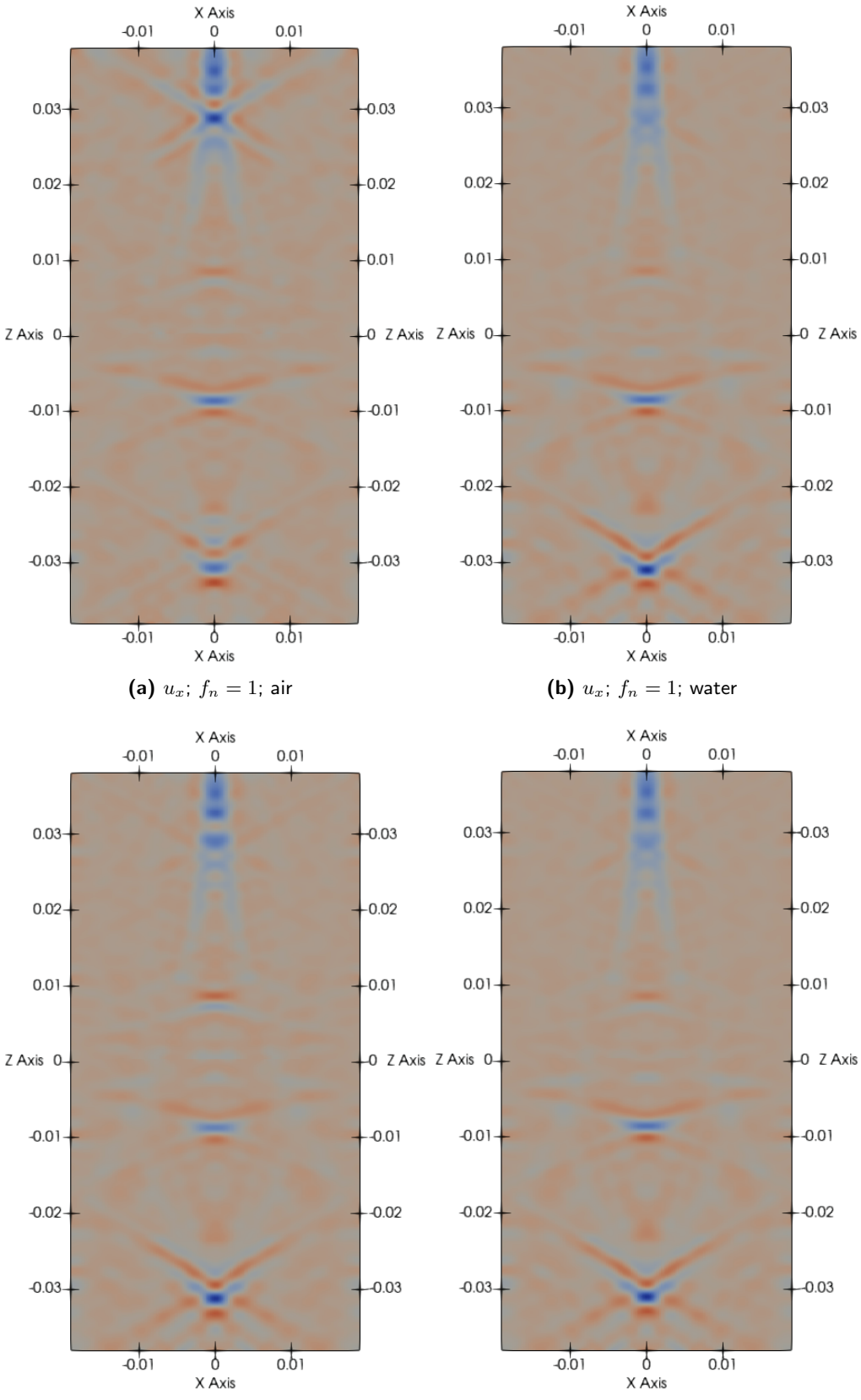

(a) u_x; $f_n = 1$; air

(b) u_x; $f_n = 1$; water

(c) u_x; $f_n = 1$; Sil. Oil

(d) u_x; $f_n = 1$; honey

Figure 36. Displacement field u_x at $t = 49$ μs, on the x-z plane for a fixed fracture number ($f_n = 1$) with the four different infill fluids (a) air, (b) water, (c) silicon oil, and (d) honey.

For S-wave, the numerical simulations show a trend consistent with laboratory results in terms of fluid density but slightly overestimate the S-wave transmission coefficient and quality factor (Q_s). As with P-wave, this indicates that the model does not adequately account well for wave attenuation mechanisms. In the fluid-filled fractures, especially with silicon oil, the gap between numerical and laboratory results become more pronounced.

The overestimated values of transmission coefficient and quality factors (Q_p and Q_s) in the numerical simulations compared to laboratory experiments, suggest reduced attenuation in the simulated medium. This is expected, as LSM assumes an idealized representation of fractures. However, this assumption does not hold for liquid-filled fractures. The overestimation of the transmission coefficient is more significant for S-waves than for P-waves, as S-wave could be more sensitive to additional factors, such as fracture surface roughness, and are not fully influenced by fluid properties. This, along with the simplified fracture representation in the numerical approach, leads to discrepancies between the numerical and laboratory results. Overall, these findings indicate that while LSM captures the general wave behavior, it does not fully account for fluid-induced attenuation, especially with fluids like silicon oil. Incorporating an additional term into the complianceone that adjusts for fluid propertiescould enhance the model's ability to represent the increased stiffness and energy loss associated with fluid-filled fractures, as proposed by Schoenberg (1980), Pyrak-Nolte et al. (1990a), and Möller & Friederich (2019).

While LSM assumes an idealized elastic representation and does not explicitly account for viscous energy dissipation, the numerical results nonetheless reflect key attenuation trends observed in the laboratory. this is particularly notable considering that this study was able to capture the general trend of attenuation reduction using the elastic formulation.

Despite these differences, the comparison between numerical and laboratory results validates the use of dynamic compliance values derived from ultrasonic pulse techniques. These values effectively distinguish between fracture infill materials, demonstrating the strength of the compliance-based approach while pointing to areas for further refinement to better represent attenuation effects observed in laboratory settings.

5.4 Effect of fluid properties and fracture number on wave propagation and compliance

Unlike previous studies that primarily focused on single fracture under different effective stresses in dry and saturated conditions, often using water as the saturating fluid (Pyrak-Nolte et al., 1990b) or varying the volumes of liquid and air (Yang et al., 2020), in our experimental setup, we increased the fluid volume by increasing the number of fractures, while maintaining a constant pressure. Additionally, we investigated the effects of different fluids in the fractures. Figures 21 and 22 show the effect of a fluid-filled fracture on elastic wave propagation. These figures exhibit that (a) the amplitude of the transmitted pulse increases with higher fluid density, compared to the dry case, but it consistently remains lower than that of the intact specimen, and (b) P- and S-wave arrival times increase when fluid density decreases. This is consistent with previous findings (Place et al., 2016; Yang et al., 2019, 2020) and confirms that the wave amplitude is highly dependent on the fluid density.

About the relationship between fluid viscosity and wave attenuation in fluid-filled fractures, it has been suggested that higher fluid viscosity leads to increased wave attenuation (Yang et al., 2019). However, this is not the case in my experiments (see figure 26). I observed that, as fluid viscosity increases, the attenuation caused by fluid-filled fractures decreases. This is because the higher-viscosity fluids can transmit the waves more effectively, resulting in reduced wave attenuation. Therefore, the increased viscosity leads to a more effective coupling of the waves with the surrounding material, allowing for better transmission and less energy loss.

The ratio of normal to tangential fracture compliance, denoted as Z_n/Z_t, serves as a fluid indicator (Liu et al., 2000) and plays an important role in characterizing fluid behavior within fracture systems. Figure 19 illustrates how this ratio varies as a function of fluid density. The data shows that the ratio decreases as the density of the fluid increases. For the dry case, the Z_n/Z_t values are greater than 1.0, between $2.57 < Z_n/Z_t < 3.32$ as shown by circular markers. In contrast, for fluid-saturated cases the ratio falls between $0.29 < Z_n/Z_t < 0.56$, marked by triangles, squares and diamonds. These results are compared with data from Hsu & Schoenberg (1993), who determined this ratio using honey as saturating fluid between lucite plates. They reported a ratio between 0.8 and 1.0 for a saturation of 0 to 25 $\%$, whereas, for a saturation of 100 $\%$, the value is approximately 0.1. Notably, for honey as the saturating fluid, my results are in accordance with those from Hsu & Schoenberg (1993) at 20 MPa. This indicates near or complete saturation within the fractures in my experiments, despite open boundary conditions that allow fluids to escape.

I compare the values from this study with the theoretical Z_n/Z_t ratios for the dry case. These theoretical ratios are determined using equations 7 and 8. These equations are based on models in which fractures are treated as a planar distribution of cracks. In figure 19, these models are labeled M1 and M2, respectively, with open and filled black circles. I found that the presence of multiple fractures, as opposed to a single fracture, particularly in LSM, improves the statistical representation. It means that the individual interaction of each fracture produces an accumulative effect. For instance, for the dry case, the ratio for ten fractures is 2.57, which is significantly higher than theoretical predictions (M1 and M2) yielding ratios of 0.83 and 0.79, respectively. It is worth noting that, due to the absence of theoretical relationships between normal and tangential compliance for fluid-filled fractures, I was only able to compute ratios for the dry case.

In summary, as is shown in figure 19, there is a clear decrease in the Z_n/Z_t ratio as fluid density increases, with additional complexity introduced by the number of fractures present in the specimen. Moreover, the roughness and irregularities of fracture surfaces in the lab samples may contribute to this trend. These surface characteristics reduce tangential compliance more than normal compliance, potentially amplifying the observed Z_n/Z_t ratios in multi-fracture systems.

There is limited available information regarding the comparisons of static and dynamic compliances. According to Pyrak-Nolte et al. (1990b) and Pyrak-Nolte (2019), single natural fractures show higher static compliance compared to dynamic compliance, typically three times greater. Also, Zhou et al. (2020) correlated normal static and dynamic fracture compliance. Using artificial rock fractures with shale and granitic rocks, they found that static compliance exceeded dynamic compliance, with the ratio approaching 2 at around 20 MPa of normal stress and gradually nearing 1 with increasing stress. Our findings agree with the observation made by Pyrak-Nolte et al. (1990b); Zhou et al. (2020), confirming that static compliance is consistently higher than dynamic compliance. This consistency applies to both normal and tangential components. However, the specific ratio varies depending on the type of fluid.

Both static and dynamic compliances are influenced by void volume content (Pyrak-Nolte, 2019), as demonstrated by the significant change when transitioning from air to fluid-filled cases. In the dynamic normal compliance (see Figure 20a), a clear trend is observed with fluid density: compliance decreases significantly as fluid density increases. This indicates that denser fluids, such as honey, make the fracture less compliant. In contrast, the static normal compliance (see Figure 20b) shows a different pattern. For static compliance, the trend breaks down with water which exhibits a larger compliance than silicon oil, despite its lower density. This deviation can be explained by fluid viscosity and its influence on void space within the fracture. Silicon oil's higher viscosity allows it to stay within the fracture, filling void

space and resulting in a lower static compliance. Water, with its lower viscosity, flows out more easily, creating a larger effective void space and therefore increasing static compliance.

Interestingly, dynamic compliance shows the opposite trend, with water being less compliant than silicon oil. This suggests that, while void volume content plays a role that is related to density, it is not the dominant factor in dynamic compliance. In the dynamic case, the higher density of water increases fracture stiffness, making it less compliant than silicon oil even though the void volume content may be higher. This underscores the role of fluid properties in determining compliance behavior, with viscosity influencing static compliance and density being more influential in dynamic compliance.

Tables 4 and 5 summarize the range of values for the static/dynamic compliance ratio for the different types of fluids, for normal and tangential components. In general, there is no clear pattern between this ratio and the fluid density. However, in dry cases for normal component, regardless of the number of fractures, the ratio falls within a relatively narrow range of variability between 2.25 and 3.52. In contrast, the range for fluid cases spans a broader range, from 4.87 to 18.20. The highest values correspond to water and the lowest are associated with honey. For the tangential component, the range of variability is broader in both, dry and fluid cases. For the dry case, the range is from 8.06 to 14.13 and for the fluid cases lies between 2.23 to 12.64.

The difference in the observed ratio of static/dynamic normal compliance primarily arises from the nature of each experiment. For example, in the case of water and silicon oil, having the lowest density between the liquids, the notably high ratio in the normal component is a consequence of a substantial displacement or fracture closure, leading to significant static normal compliance values. Interestingly, regardless of the fluid type, the case involving ten fractures yields the lowest ratio. This suggests that, as the number of fractures increases, both static and dynamic normal compliances tend to converge. As the tangential static compliances were derived from normal static values by using the relations 7 and 8, the values of the ratio static/dynamic tangential component falls within a common range without significant variations within the models.

Table 4. Ratio of normal static to dynamic compliance

Type of fluid	1 fracture	5 fractures	10 fractures
Dry	3.52	2.25	2.59
Sil. Oil	9.00	8.73	6.30
Water	18.20	18.07	13.80
Honey	6.47	5.81	4.87

Table 5. Ratio of tangential static to dynamic compliance

Type of fluid	1 fracture		5 fractures		10 fractures	
	M1	M2	M1	M2	M1	M2
Dry	14.13	14.77	8.69	9.09	8.06	8.42
Sil. Oil	3.25	3.40	5.02	5.25	4.30	4.49
Water	12.09	12.64	8.79	9.19	7.66	8.01
Honey	4.47	4.68	2.23	2.33	2.29	2.39

Key wave parameters

The key wave parametersvelocity, transmission coefficient, and quality factorare essential for characterizing wave behavior in fractured systems filled with fluids. These parameters provide insights into the stiffness of the medium, the influence of fluid properties on wave propagation, the energy transmitted across fractures, and the mechanisms of wave energy dissipation.

Ultrasonic data from this study reveal that P-wave velocity, transmission coefficient, and quality factor (Q_p) correlate positively with the density of the saturating fluids (Figures 23a, 24a, 25a). For dry fractures, these parameters show lower values due to the absence of fluid, resulting in greater effective compliance. In contrast, fractures filled with fluids exhibit an increase in these parameters. The observed trends in P-wave velocity align with previous findings by Yang et al. (2020), confirming that key wave parameters are strongly dependent on fluid properties.

However, discrepancies arise when considering the transmission coefficient and quality factor for P-waves in fluid-filled fractures. These variations can be attributed to the interplay between fluid density, viscosity, fracture thickness and fracture spacing (average distance between parallel fracture). For instance, Yang et al. (2020) observed a positive correlation between transmission coefficient and fluid density, which is consistent with my results. However, they also reported an inverse relationship between viscosity and both transmission coefficient and quality factor. In contrast, my experiments show an opposite trend specifically with the liquids: lower viscosity fluids resulted in lower transmission and lower Q_p, similar to observations by Clarke et al. (2020).

The quality factor is inversely related to the amount of energy lost due to scattering, absorption, and transmission in the medium. A higher Q means less attenuation, indicating that the medium is more efficient at preserving wave energy during propagation. The general trend for the three fluids observed in Q_p of this study (figure 26) show a more complex relationship between viscosity and Q_p than a simple positive or negative correlation suggesting a non-uniform relationship between viscosity and quality factor.

However, the differences between my results and those of other studies can be explained by the distinct experimental setups used, particularly fracture characteristics such as their number, distribution and size. Yang et al. (2020) employed cylindrical specimen with a single fracture of finite thickness (6 mm), while Clarke et al. (2020) investigated cylindrical specimens with distributed cracks. In contrast, this study examines cylindrical specimens with one and multiple fractures, with thicknesses on the order of micrometers.

Although wave attenuation is expected in viscous media, the experimental conditions in this study suggest that the wavelength and fracture thickness may prevent the wave from fully interacting with the fluid due to the high frequency of the seismic wave. This likely minimizes the effect of viscosity, allowing density and bulk modulus to dominate. As a result, the fractures behave as if they are stiffer, reducing the impedance contrast and explaining the observed discrepancies. Regarding the number of fractures, it is difficult to make direct comparisons, as most studies focus on a single fracture. However, in this study, the observed trend remains consistent: while the key wave parameters follow the same general pattern, their values decrease as the number of fractures increases. This can be attributed to the complex interaction of the wave with multiple fractures along the specimen, which results in a more significant scattering and energy dissipation. For all samples used in these experiments, the fracture spacing ranges between 1 and 13 times the seismic wavelength (λ), placing them in a regime where scattering effects are strongly influenced by interference between waves interacting with adjacent fractures. This relationship further explains the observed increase in attenuation with increasing number of fractures (decreasing fracture spacing).

For S-wave in fluid-filled fractures, it might initially be anticipated that fluid saturation would have little effect on their transmission. However, this expectation is not entirely supported by our observations as well as by Pyrak-Nolte et al. (1990b). Significant variations and distinct behavior are evident. Unlike P-waves, where the key wave parameters exhibit a wide range of values that effectively distinguish between dry and fluid cases, S-waves show a narrower variation range. This suggests that S-waves are less sensitive to the presence of fluids, with their values in dry cases being relatively similar to those in fluid-saturated cases.

The transmission of S-waves is also facilitated by the connected asperities of the fracture surfaces, which maintain mechanical contact even in the presence of fluids. These asperities contribute to the overall compliance of the fractures, enabling the propagation of shear waves regardless of fluid saturation.

The general trend for the key S-wave parameters exhibits a concave upward dependency on fluid density

irrespective of the number of fractures (see figures 23b, 24b, 25b). This trend suggest that silicon oil for S-wave, as the infilling material, makes the fracture more compliant compared to the other liquids and even to the dry case. The possible explanation to this behavior could be a combination of the viscoelastic nature of the silicon oil, increased tangential dynamic compliance, and weaker interaction with the fracture surface.

Unlike denser fluids (water and honey), the viscoelastic behavior of the silicon oil might reduce the shear-wave coupling between the fracture walls, resulting in higher tangential compliance, leading to reduced S-wave amplitudes, transmission coefficient and quality factor (Q_s) compared to the other fluids.

Despite the relatively limited information available on S-wave behavior in fluid-filled fractures, a recent study by Yang et al. (2024) presents intriguing observations of S-waves in fluid-saturated media. They investigate how varying water saturation levels influence S-wave propagation and attenuation across clay-rich rock fractures filled with kaolinite-dominant gouges (2-mm thickness). Ultrasonic experiments revealed that S-wave velocity fluctuates slightly with water saturation, and that spectral amplitudes and seismic quality factors are affected differently. Notably, S-waves exhibit less sensitivity to water saturation compared to P-waves, with trends in velocity, frequency, and attenuation attributed to the skeletal frame properties of the medium, as opposed to the fluid-particle interactions that dominate P-wave behavior.

In many ways, our results align with and expand upon the findings of Yang et al. (2024). While their study highlights the dependence of S-wave behavior on the skeletal frame in clay-rich fractures, our results demonstrate the significant role of infilling fluid properties, particularly for viscoelastic fluids like silicon oil. This additional information enhances the understanding of how fluid type and density influence the mechanical response of fractures to S-wave propagation.

Chapter 6. Conclusions

This study tested the hypothesis that variations in fluid density and viscosity produce measurable changes in fracture compliance, thus controlling the propagation of P- and S-waves in fractured media. Therefore, laboratory experiments and numerical simulations were integrated to evaluate the influence of fluid-filled fractures on seismic wave behavior.

Laboratory ultrasonic experiments demonstrated that normal fracture compliance decreases with increasing fluid density, while tangential compliance shows limited sensitivity. This confirm a strong inverse relationship between fluid density and normal compliance, supporting the hypothesis that fracture compliance is sensitive to fluid properties.

The normal to tangential compliance ratio effectively distinguishes between dry and fluid-filled fractures, confirming its potential as a fluid indicator, although differences among fluids of similar density remain small. Additionally, the presence of multiple fractures resulted in a cumulative effect that amplifies the influence of fluid properties.

Laboratory experiments showed that the relationship between wave attenuation and fluid viscosity is complex and cannot be described by a monotonic trend. This finding highlight the role of viscosity in controlling energy dissipation.

Incorporating the laboratory compliance values into the Interior Penalty Discontinous Galerkin Method (IP-DGM) simulations successfully reproduced key features observed in the laboratory seismograms. P-waves were particularly sensitive to fluid density due to acoustic impedance contrasts, whereas S-waves remained unaffected.

The accurate quantification of compliance enabled the simulations to capture amplitude decay and arrival time delays, demonstrating that the laboratory derived values are both robust and practically useful for predictive modeling of wave propagation in fractured media.

This work present the first laboratory-derived compliance values within IP-DGM simulations, establishing a predictive framework that integrates controlled experimental measurements with advanced numerical modeling. The results confirm that fracture compliance is a key parameter linking fluid properties to seismic wave behavior and that combining experiments with numerical modeling improves the ability to model wave propagation in fluid-saturated fractured media.

While attenuation is not explicitly modeled in the elastic formulation of the LSM, the incorporation of

laboratory derived dynamic compliances allow its influence to be indirectly quantified, enabling good comparison with experimental results. However, discrepancies in amplitude attenuation suggest that LSM could be improved by incorporating additional compliance corrections to better represent fluid effects.

This discrepancies highlight directions for future research, including testing fluids relevant to the oil industry, improving the LSM to better capture attenuation and transmission coefficients, and extending the approach to more realistic subsurface fracture networks.

Overall, this study demonstrates that accurately measured fracture compliance serves as a robust bridge between fluid properties and seismic response, providing a validated methodology to integrate experimental observations into predictive numerical simulations. By linking laboratory measurements to numerical modeling, this framework enhances our understanding of seismic wave propagation in fractured media and provides a foundation for future studies in more complex subsurface environments.

Bibliography

Aguilera, R. (1998). Geologic aspects of naturally fractured reservoirs. *The Leading Edge*, *17*(12), 1667–1670. https://doi.org/10.1190/1.1437912.

Arnold, D. N. (1982). An interior penalty finite element method with discontinuous elements. *SIAM journal on numerical analysis*, *19*(4), 742–760. https://doi.org/10.1137/0719052.

Arnold, D. N., Brezzi, F., Cockburn, B., & Marini, D. (2000). Discontinuous galerkin methods for elliptic problems. In *Discontinuous Galerkin Methods: Theory, Computation and Applications*, (pp. 89–101). Springer.

Arora, K., Cazenave, A., Engdahl, E. R., Kind, R., Manglik, A., Roy, S., Sain, K., & Uyeda, S. (2011). *Encyclopedia of solid earth geophysics*. Springer Science & Business Media.

Ba, J., Pan, X., Carcione, J. M., & Ma, R. (2023). Effects of pressure and fluid properties on p-wave velocity and attenuation of tight sandstones. *Frontiers in Earth Science*, *10*, 1065630. https://doi.org/10.3389/feart.2022.1065630.

Baird, A. F., Kendall, J.-M., Verdon, J. P., Wuestefeld, A., Noble, T. E., Li, Y., Dutko, M., & Fisher, Q. J. (2013). Monitoring increases in fracture connectivity during hydraulic stimulations from temporal variations in shear wave splitting polarization. *Geophysical Journal International*, *195*(2), 1120–1131. https://doi.org/10.1093/gji/ggt274.

Bakulin, A., Grechka, V., & Tsvankin, I. (2000). Estimation of fracture parameters from reflection seismic datapart i: Hti model due to a single fracture set. *Geophysics*, *65*(6), 1788–1802. https://doi.org/10.1190/1.1444863.

Barton, N. (2006). *Rock quality, seismic velocity, attenuation and anisotropy*. CRC press.

Berryman, J. G. (2007). Seismic waves in rocks with fluids and fractures. *Geophysical Journal International*, *171*(2), 954–974. https://doi.org/10.1111/j.1365-246X.2007.03563.x.

Best, A. I. (1992). Seismic attenuation and pore-fluid viscosity in clay-rich sandstones. In *SEG Technical Program Expanded Abstracts 1992*, (pp. 674–676). Society of Exploration Geophysicists.

Brown, S. R. & Scholz, C. H. (1985). Closure of random elastic surfaces in contact. *Journal of Geophysical Research: Solid Earth*, *90*(B7), 5531–5545. https://doi.org/10.1029/JB090iB07p05531.

Brown, S. R. & Scholz, C. H. (1986). Closure of rock joints. *Journal of Geophysical Research: Solid Earth*, *91*(B5), 4939–4948. https://doi.org/10.1029/JB091iB05p04939.

Cai, J. & Zhao, J. (2000). Effects of multiple parallel fractures on apparent attenuation of stress waves in rock masses. *International Journal of Rock Mechanics and Mining Sciences*, *37*(4), 661–682. https://doi.org/10.1016/S1365-1609(00)00013-7.

Choi, M.-K., Bobet, A., & Pyrak-Nolte, L. J. (2014). The effect of surface roughness and mixed-mode loading on the stiffness ratio $\kappa x/\kappa z$ for fracturesstiffness ratio $\kappa x/\kappa z$ for fractures. *Geophysics*, *79*(5), D319–D331. https://doi.org/10.1190/geo2013-0438.1.

Clarke, J., Adam, L., van Wijk, K., & Sarout, J. (2020). The influence of fluid type on elastic wave velocity and attenuation in volcanic rocks. *Journal of Volcanology and Geothermal Research*, *403*, 107004. https://doi.org/10.1016/j.jvolgeores.2020.107004.

Coates, R. T. & Schoenberg, M. (1995). Finite-difference modeling of faults and fractures. *Geophysics*, *60*(5), 1514–1526. https://doi.org/10.1190/1.1443884.

Cockburn, B., Karniadakis, G. E., & Shu, C.-W. (2000). *Discontinuous Galerkin methods: theory, computation and applications*, volume 11. Springer Science & Business Media.

Cockburn, B. & Shu, C. (1989). TVB Runge-Kutta Local Projection Discontinuous Galerkin Finite Element Method for Conservation Laws II: General Framework. *Mathematics of Computation*, *52*(186), 411–435. https://doi.org/10.2307/2008474.

Crampin, S. (1984). Effective anisotropic elastic constants for wave propagation through cracked solids. *Geophysical Journal International*, *76*(1), 135–145. https://doi.org/10.1111/j.1365-246X.1984.tb05029.x.

Dawson, C., Sun, S., & Wheeler, M. F. (2004). Compatible algorithms for coupled flow and transport. *Computer Methods in Applied Mechanics and Engineering*, *193*(23-26), 2565–2580. https://doi.org/10.1016/j.cma.2003.12.059.

De Basabe, J. D. (2009). High-order finite element methods for seismic wave propagation. [Thesis Doctor of Philosophy, The University of Texas at Austin]. Disponible en: https://repositories.lib.utexas.edu/items/c9ab8ccc-412d-49bb-956b-5ecd6a9075e2.

De Basabe, J. D. (2011). Elementos finitos de orden superior para propagación de ondas sísmicas. *GEOS*, *31*(2), 228-245.

De Basabe, J. D., Sen, M. K., & Wheeler, M. F. (2008). The interior penalty discontinuous galerkin method for elastic wave propagation: grid dispersion. *Geophysical Journal International*, *175*(1), 83–93. https://doi.org/10.1111/j.1365-246X.2008.03915.x.

De Basabe, J. D., Sen, M. K., & Wheeler, M. F. (2016). Elastic wave propagation in fractured media using the discontinuous galerkin method. *Geophysics*, *81*(4), T163–T174. https://doi.org/10.1190/geo2015-0602.1.

Duru, K., Rannabauer, L., Gabriel, A.-A., Ling, O. K. A., Igel, H., & Bader, M. (2019). A stable discontinuous galerkin method for linear elastodynamics in 3d geometrically complex media using physics based numerical fluxes. *arXiv preprint arXiv:1907.02658*. https://doi.org/10.48550/arXiv.1907.02658.

Evans, K. & Wyatt, F. (1984). Water table effects on the measurement of earth strain. *Tectonophysics*, *108*(3-4), 323–337. https://doi.org/10.1016/0040-1951(84)90242-7.

Ferroni, A. (2017). Discontinuous galerkin spectral element methods for the elastodynamics equation on hybrid hexahedral-tetrahedral grids. [Thesis Doctor of Philosophy, Politecnico Di Milano]. Disponible en: https://tesidottorato.depositolegale.it/handle/20.500.14242/207068.

Fidkowski, K. J. & Chen, G. (2020). Output-based mesh optimization for hybridized and embedded discontinuous galerkin methods. *International Journal for Numerical Methods in Engineering*, *121*(5), 867–887. https://doi.org/10.1002/nme.6248.

Giwelli, A., Sakaguchi, K., & Matsuki, K. (2009). Experimental study of the effect of fracture size on closure behavior of a tensile fracture under normal stress. *International Journal of Rock Mechanics and Mining Sciences*, *46*(3), 462–470. https://doi.org/10.1016/j.ijrmms.2008.11.008.

Goodman, R. E. (1976). *Methods of geological engineering in discontinuous rocks*. West Group.

Goodman, R. E., Taylor, R. L., & Brekke, T. L. (1968). A model for the mechanics of jointed rock. *Journal of the soil mechanics and foundations division*, *94*(3), 637–659. https://doi.org/10.1061/JSFEAQ.0001133.

Guo, J., Shuai, D., Wei, J., Ding, P., & Gurevich, B. (2018). P-wave dispersion and attenuation due to scattering by aligned fluid saturated fractures with finite thickness: Theory and experiment. *Geophysical Journal International*, *215*(3), 2114–2133. https://doi.org/10.1093/gji/ggy406.

Gurevich, B., Makarynska, D., de Paula, O. B., & Pervukhina, M. (2010). A simple model for squirt-flow dispersion and attenuation in fluid-saturated granular rocks. *Geophysics*, *75*(6), N109–N120. https://doi.org/10.1190/1.3509782.

Hall, F. & Wang, Y. (2012). Seismic response of fractures by numerical simulation. *Geophysical Journal International*, *189*(1), 591–601. https://doi.org/10.1111/j.1365-246X.2012.05360.x.

Hardin, E., Cheng, C., Paillet, F., & Mendelson, J. (1987). Fracture characterization by means of attenuation and generation of tube waves in fractured crystalline rock at mirror lake, new hampshire. *Journal of Geophysical Research: Solid Earth*, *92*(B8), 7989–8006. https://doi.org/10.1029/JB092iB08p07989.

Hobday, C. & Worthington, M. (2012). Field measurements of normal and shear fracture compliance. *Geophysical Prospecting*, *60*(3), 488–499. https://doi.org/10.1111/j.1365-2478.2011.01000.x.

Hornby, B. E. (1998). Experimental laboratory determination of the dynamic elastic properties of wet, drained shales. *Journal of Geophysical Research: Solid Earth*, *103*(B12), 29945–29964. https://doi.org/10.1029/97JB02380.

Hsu, C.-J. & Schoenberg, M. (1993). Elastic waves through a simulated fractured medium. *Geophysics*, *58*(7), 964–977. https://doi.org/10.1190/1.1443487.

Hudson, J., Liu, E., & Crampin, S. (1997). The mean transmission properties of a fault with imperfect facial contact. *Geophysical Journal International*, *129*(3), 720–726. https://doi.org/10.1111/j.1365-246X.1997.tb04507.x.

Hudson, J., Pointer, T., & Liu, E. (2001). Effective-medium theories for fluid-saturated materials with aligned cracks. *Geophysical Prospecting*, *49*(5), 509–522. https://doi.org/10.1046/j.1365-2478.2001.00272.x.

Hudson, J. A. (1981). Wave speeds and attenuation of elastic waves in material containing cracks. *Geophysical Journal International*, *64*(1), 133–150. https://doi.org/10.1111/j.1365-246X.1981.tb02662.x.

Hughes, T. (1987). *The finite element method. Linear static and dynamic finite element analysis*. Englewood Cliffs, New Jersey: Prentice-Hall International.

Iding, M. & Ringrose, P. (2009). Evaluating the impact of fractures on the long-term performance of the in salah co2 storage site. *Energy Procedia*, *1*(1), 2021–2028. https://doi.org/10.1016/j.egypro.2009.01.263.

Jung, R. (1989). Hydraulic in situ investigations of an artificial fracture in the falkenberg granite. In *International Journal of Rock Mechanics and Mining Sciences & Geomechanics Abstracts*, volume 26, 301–308. Elsevier. https://doi.org/10.1016/0148-9062(89)91978-5.

Käser, M. & Dumbser, M. (2006). An arbitrary high-order discontinuous galerkin method for elastic waves on unstructured meshesi. the two-dimensional isotropic case with external source terms. *Geophysical Journal International*, *166*(2), 855–877. https://doi.org/10.1111/j.1365-246X.2006.03051.x.

Komatitsch, D. & Tromp, J. (1999). Introduction to the spectral element method for three-dimensional seismic wave propagation. *Geophysical journal international*, *139*(3), 806–822. https://doi.org/10.1046/j.1365-246x.1999.00967.x.

Komatitsch, D. & Vilotte, J.-P. (1998). The spectral element method: an efficient tool to simulate the seismic response of 2d and 3d geological structures. *Bulletin of the seismological society of America*, *88*(2), 368–392. https://doi.org/10.1785/BSSA0880020368.

Lähivaara, T. (2010). Discontinuous galerkin method for time-domain wave problems. [Thesis Doctor of Philosophy, University of Eastern Finland]. Disponible en: https://erepo.uef.fi/server/api/core/bitstreams/60fd9dac-7ab3-4a5a-8741-abc6e12dec74/content.

Leviant, V., Kvasov, I., & Petrov, I. (2019). *Numerical modeling of seismic responses from fractured reservoirs by the grid-characteristic method*. Society of Exploration Geophysicists.

Liu, E. (2005). Effects of fracture aperture and roughness on hydraulic and mechanical properties of rocks: implication of seismic characterization of fractured reservoirs. *Journal of Geophysics and Engineering*, *2*(1), 38. https://doi.org/10.1088/1742-2132/2/1/006.

Liu, E., Hudson, J. A., & Pointer, T. (2000). Equivalent medium representation of fractured rock. *Journal of Geophysical Research: Solid Earth*, *105*(B2), 2981–3000. https://doi.org/10.1029/1999JB900306.

Liu, E. & Martinez, A. (2012). *Seismic Fracture Characterization: Concepts and Practical Applications (EET 8)*. Earthdoc.

Lubbe, R., Sothcott, J., Worthington, M., & McCann, C. (2008). Laboratory estimates of normal and shear fracture compliance. *Geophysical Prospecting*, *56*(2), 239–247. https://doi.org/10.1111/j.1365-2478.2007.00688.x.

Lubbe, R. & Worthington, M. (2006). A field investigation of fracture compliance. *Geophysical Prospecting*, *54*(3), 319–331. https://doi.org/10.1111/j.1365-2478.2006.00530.x.

Makurat, A., Barton, N., Tunbridge, L., & Vik, G. (1991). The measurement of the mechanical and hydraulic properties of rock joints at different scales in the stripa project. *Publikasjon-Norges Geotekniske Institutt*, *182*, 541-548.

Martin, R., Komatitsch, D., Blitz, C., & Le Goff, N. (2008). Simulation of seismic wave propagation in an asteroid based upon an unstructured mpi spectral-element method: Blocking and non-blocking communication strategies. In Palma, J. M. L. M., Amestoy, P. R., Daydé, M., Mattoso, M., & Lopes, J. C., editors, *High Performance Computing for Computational Science - VECPAR 2008*, 350–363. Springer Berlin Heidelberg.

Mavko, G., Mukerji, T., & Dvorkin, J. (2020). *The rock physics handbook*. Cambridge university press.

Mindlin, R. (1960). Waves and vibrations in isotropic, elastic plates. *Structure Mechanics*, , 199–232. https://doi.org/157423187448208473 6s.

Möller, T. & Friederich, W. (2019). Simulation of elastic wave propagation across fractures using a nodal discontinuous galerkin methodtheory, implementation and validation. *Geophysical Journal International*, *219*(3), 1900–1914. https://doi.org/10.1093/gji/ggz410.

Möllhoff, M., Bean, C., & Meredith, P. (2010). Rock fracture compliance derived from time delays of elastic waves. *Geophysical Prospecting*, *58*(6), 1111–1122. https://doi.org/10.1111/j.1365-2478.2010.00887.x.

Myer, L., Pyrak-Nolte, L., & Cook, N. (1990). Effects of single fractures on seismic wave propagation. *Rock joints*, *15*, 467–473. https://doi.org/escholarship.org/uc/item/5nz6p4cd.

O'Connell, R. J. & Budiansky, B. (1977). Viscoelastic properties of fluid-saturated cracked solids. *Journal of Geophysical Research*, *82*(36), 5719–5735. https://doi.org/10.1029/JB082i036p05719.

Pimienta, L., Fortin, J., & Guéguen, Y. (2016). Effect of fluids and frequencies on poissons ratio of sandstone samples. *Geophysics*, *81*(2), D183–D195. https://doi.org/10.1190/geo2015-0310.1.

Place, J., Ghafar, A. N., Malehmir, A., Draganovic, A., & Larsson, S. (2016). On using the thin fluid-layer approach at ultrasonic frequencies for characterising grout propagation in an artificial fracture. *International Journal of Rock Mechanics and Mining Sciences*, *89*, 68–74. https://doi.org/10.1016/j.ijrmms.2016.07.010.

Pratt, H., Swolfs, H., Brace, W., Black, A., & Handin, J. (1977). Elastic and transport properties of an in situ jointed granite. In *International Journal of Rock Mechanics and Mining Sciences & Geomechanics Abstracts*, volume 14, 35–45. Elsevier. https://doi.org/10.1016/0148-9062(77)90560-5.

Prioul, R., Donald, A., Koepsell, R., Marzouki, Z. E., & Bratton, T. (2007). Forward modeling of fracture-induced sonic anisotropy using a combination of borehole image and sonic logs. *Geophysics*, *72*(4), E135–E147. https://doi.org/10.1190/1.2734546.

Prioul, R., Jocker, J., Montaggioni, P., & Escaré, L. (2008). Fracture compliance estimation using a combination of image and sonic logs. In *SEG Technical Program Expanded Abstracts 2008*, (pp. 314–318). Society of Exploration Geophysicists.

Pyrak, L. J. (1988). Seismic visibility of fractures. [Thesis Doctor of Philosophy, University of California, Berkeley]. Disponible en: https://www.osti.gov/biblio/6720988.

Pyrak-Nolte, L. (1996). The seismic response of fractures and the interrelations among fracture properties. *International journal of rock mechanics and mining sciences & geomechanics abstracts*, *33*(8), 787–802. https://doi.org/10.1016/S0148-9062(96)00022-8.

Pyrak-Nolte, L., Cook, N., & Myer, L. (1987). Seismic visibility of fractures. In *ARMA US Rock Mechanics/Geomechanics Symposium*, ARMA–87. ARMA.

Pyrak-Nolte, L. J. (2019). Chapter 14 - fracture specific stiffness: The critical link between the scaling behavior of hydro-mechanical coupling in fractures and seismic monitoring. In *Science of Carbon Storage in Deep Saline Formations*, Process Coupling Across Time and Spatial Scales, (pp. 311–335). Elsevier.

Pyrak-Nolte, L. J., Myer, L. R., & Cook, N. G. (1990a). Anisotropy in seismic velocities and amplitudes from multiple parallel fractures. *Journal of Geophysical Research: Solid Earth*, *95*(B7), 11345–11358. https://doi.org/10.1029/jb095ib07p11345.

Pyrak-Nolte, L. J., Myer, L. R., & Cook, N. G. (1990b). Transmission of seismic waves across single natural fractures. *Journal of Geophysical Research: Solid Earth*, *95*(B6), 8617–8638. https://doi.org/10.1029/JB095iB06p08617.

Ramos-Barreto, A. L., De Basabe, J. D., & Silva-Avalos, R. U. (2025). Elastic wave propagation through cylinders with fluid-filled fractures using the discontinuous galerkin method. *Mathematics*, *13*(10), 1572. https://doi.org/10.3390/math13101572.

Rao, Y. & Wang, Y. (2015). Seismic attenuation in fractured media. *Journal of Geophysics and engineering*, *12*(1), 26–32. https://doi.org/10.1088/1742-2132/12/1/26.

Reed, W. H. & Hill, T. R. (1973). Triangular mesh methods for the neutron transport equation. Los Alamos Scientific Lab., N. Mex.(USA).

Rivière, B. (2008). *Discontinuous Galerkin methods for solving elliptic and parabolic equations: theory and implementation*. SIAM.

Rioyos-Romero, R., De Basabe, J. D., Solorza-Calderón, S., González-Escobar, M., & Gross, M. (2022). Comparison of wave-propagation simulations in fractured domains using discrete fractures and equivalent media. *Geophysical Journal International*, *230*(1), 427–447. https://doi.org/10.1093/gji/ggac014.

Riviere, B. & Wheeler, M. F. (2003). Discontinuous finite element methods for acoustic and elastic wave problems. *Contemporary Mathematics*, *329*(271-282), 4–6. https://doi.org/10.1090/conm/329.

Rivière, B., Wheeler, M. F., & Girault, V. (1999). Improved energy estimates for interior penalty, constrained and discontinuous galerkin methods for elliptic problems. part i. *Computational Geosciences*, *3*, 337–360. https://doi.org/10.1023/A:1011591328604.

Rutqvist, J. (1995). Determination of hydraulic normal stiffness of fractures in hard rock from well testing. *International journal of rock mechanics and mining sciences & geomechanics abstracts*, *32*(5), 513–523. https://doi.org/10.1016/0148-9062(95)00039-J.

Sayers, C. & Kachanov, M. (1991). A simple technique for finding effective elastic constants of cracked solids for arbitrary crack orientation statistics. *International Journal of Solids and Structures*, *27*(6), 671–680. https://doi.org/10.1016/0020-7683(91)90027-D.

Sayers, C. M. (2007). Introduction to this special section: Fractures. *The Leading Edge*, *26*(9), 1102–1105. https://doi.org/10.1190/1.2780777.

Schoenberg, M. (1980). Elastic wave behavior across linear slip interfaces. *The Journal of the Acoustical Society of America*, *68*(5), 1516–1521. https://doi.org/10.1121/1.385077.

Schoenberg, M. & Douma, J. (1988). Elastic wave propagation in media with parallel fractures and aligned cracks1. *Geophysical prospecting*, *36*(6), 571–590. https://doi.org/10.1111/j.1365-2478.1988.tb02181.x.

Shearer, P. M. (2019). *Introduction to seismology*. Cambridge university press.

Smith, S. A. (2021). Seismic wave propagation across single fractures: An experimental and numerical study. [Master Thesis, University of Oslo]. Disponible en: https://www.duo.uio.no/bitstream/handle/10852/87761/5/SA-Smith-Thesis-Final.pdf.

Stein, S. & Wysession, M. (2003). *An introduction to seismology, earthquakes, and earth structure*. Blackwell Publishing.

Suarez-Rivera, R. (1992). The influence of thin clay layers containing liquids on the propagation of shear waves. [Thesis Doctor of Philosophy, University of California, Berkeley]. Disponible en: https://www.proquest.com/openview/50d52808f0d68989629b96d8d1c66345/1?cbl=18750diss=ypq-origsite=gscholar.

Toksöz, M., Johnston, D. H., & Timur, A. (1979). Attenuation of seismic waves in dry and saturated rocks: I. laboratory measurements. *Geophysics*, *44*(4), 681–690. https://doi.org/10.1190/1.1440969.

Tsang, C.-F., Bernier, F., & Davies, C. (2005). Geohydromechanical processes in the excavation damaged zone in crystalline rock, rock salt, and indurated and plastic claysin the context of radioactive waste disposal. *International Journal of Rock Mechanics and Mining Sciences*, *42*(1), 109–125. https://doi.org/10.1016/j.ijrmms.2004.08.003.

Tsang, C.-F., Neretnieks, I., & Tsang, Y. (2015). Hydrologic issues associated with nuclear waste repositories. *Water Resources Research*, *51*(9), 6923–6972. https://doi.org/10.1002/2015WR017641.

Tsvankin, I. & Grechka, V. (2011). *Seismology of azimuthally anisotropic media and seismic fracture characterization*. Society of Exploration Geophysicists.

Vamaraju, J., Sen, M. K., De Basabe, J., & Wheeler, M. (2020). A hybrid galerkin finite element method for seismic wave propagation in fractured media. *Geophysical Journal International*, *221*(2), 857–878. https://doi.org/10.1093/gji/ggaa037.

Vasilyeva, M., De Basabe, J., Efendiev, Y., & Gibson Jr, R. (2019). Multiscale model reduction of the wave propagation problem in viscoelastic fractured media. *Geophysical Journal International*, *217*(1), 558–571. https://doi.org/doi.org/10.1093/gji/ggz043.

Vlastos, S., Liu, E., Main, I. G., & Li, X.-Y. (2003). Numerical simulation of wave propagation in media with discrete distributions of fractures: effects of fracture sizes and spatial distributions. *Geophysical Journal International*, *152*(3), 649–668. https://doi.org/10.1046/j.1365-246X.2003.01876.x.

Wei, Q., Han, D.-H., Li, H., Wang, J., Wang, Y., & Chen, J. (2024). Effects of fluid saturation and viscosity on seismic dispersion characteristics in berea sandstone. *Geophysics*, *89*(5), MR251–MR263. https://doi.org/10.1190/geo2023-0350.1.

Wheeler, M. F. (1978). An elliptic collocation-finite element method with interior penalties. *SIAM Journal on Numerical Analysis*, *15*(1), 152–161. https://doi.org/10.1137/0715010.

Wu, C., Harris, J. M., Nihei, K. T., & Nakagawa, S. (2005). Two-dimensional finite-difference seismic modeling of an open fluid-filled fracture: Comparison of thin-layer and linear-slip models. *Geophysics*, *70*(4), T57–T62. https://doi.org/10.1190/1.1988187.

Yang, H., Duan, H., & Zhu, J. (2019). Ultrasonic p-wave propagation through water-filled rock joint: an experimental investigation. *Journal of Applied Geophysics*, *169*, 1–14. https://doi.org/10.1016/j.jappgeo.2019.06.014.

Yang, H., Duan, H.-f., & Zhu, J. (2020). Effects of filling fluid type and composition and joint orientation on acoustic wave propagation across individual fluid-filled rock joints. *International Journal of Rock Mechanics and Mining Sciences*, *128*, 104248. https://doi.org/10.1016/j.ijrmms.2020.104248.

Yang, H., Duan, H.-F., Zhu, J., & Zhao, Q. (2024). Water effects on elastic s-wave propagation and attenuation across single clay-rich rock fractures: Insights from ultrasonic measurements. *Rock Mechanics and Rock Engineering*, *57*(4), 2645–2659. https://doi.org/10.1007/s00603-023-03712-6.

Yousef, B. & Angus, D. (2016). When do fractured media become seismically anisotropic? some implications on quantifying fracture properties. *Earth and Planetary Science Letters*, *444*, 150–159. https://doi.org/10.1016/j.epsl.2016.03.040.

Zangerl, C., Evans, K., Eberhardt, E., & Loew, S. (2008). Normal stiffness of fractures in granitic rock: A compilation of laboratory and in-situ experiments. *International journal of rock mechanics and mining sciences*, *45*(8), 1500–1507. https://doi.org/10.1016/j.ijrmms.2008.02.001.

Zhang, Z., Zhu, J., & Deng, J. (2023). A comparative study for determining rock joint normal stiffness with destructive uniaxial compression and nondestructive ultrasonic wave testing. *Journal of Rock Mechanics and Geotechnical Engineering*, *15*(7), 1700–1712. https://doi.org/10.1016/j.jrmge.2022.10.010.

Zhao, J., Cai, J., Zhao, X., & Li, H. (2006). Experimental study of ultrasonic wave attenuation across parallel fractures. *Geomechanics and Geoengineering: An International Journal*, *1*(2), 87–103. https://doi.org/10.1080/17486020600834613.

Zhou, J., Zhang, L., Qi, S., & Yang, D. (2020). Empirical ratio of dynamic to static stiffness for propped artificial fractures under variable normal stress. *Engineering geology*, *273*, 105683. https://doi.org/10.1016/j.enggeo.2020.105683.

Zhu, J., Zhao, X., Li, J., Zhao, G., & Zhao, J. (2011). Normally incident wave propagation across a joint set with the virtual wave source method. *Journal of Applied Geophysics*, *73*(3), 283–288. https://doi.org/10.1016/j.jappgeo.2011.01.012.

Zhu, J., Zhao, X., Wu, W., & Zhao, J. (2012). Wave propagation across rock joints filled with viscoelastic medium using modified recursive method. *Journal of Applied Geophysics*, *86*, 82–87. https://doi.org/10.1016/j.jappgeo.2012.07.012.

Zimmerman, R. W. & King, M. S. (1985). Propagation of acoustic waves through cracked rock. In *Research & engineering applications in rock masses: proceedings of the 26th US Symposium on Rock Mechanics, South Dakota School of Mines & Technology, Rapid City*, 26–28.